REALIZATION OF A CANINE POSITIONING DEVICE FOR IN SITU PROSTATE PHASE CONTRAST – COMPUTED TOMOGRAPHY IMAGING

A Thesis Submitted to the College of
Graduate and Postdoctoral Studies
In Partial Fulfillment of the Requirements
For the Degree of Master of Science
In the Division of Biomedical Engineering
University of Saskatchewan
Saskatoon

By
Jay D. Keith

Permission to Use

In presenting this thesis/dissertation in partial fulfillment of the requirements for a Postgraduate degree from the University of Saskatchewan, I agree that the Libraries of this University may make it freely available for inspection. I further agree that permission for copying of this thesis/dissertation in any manner, in whole or in part, for scholarly purposes may be granted by the professor or professors who supervised my thesis/dissertation work or, in their absence, by the Head of the Department or the Dean of the College in which my thesis work was done. It is understood that any copying or publication or use of this thesis/dissertation or parts thereof for financial gain shall not be allowed without my written permission. It is also understood that due recognition shall be given to me and to the University of Saskatchewan in any scholarly use which may be made of any material in my thesis/dissertation.

DISCLAIMER

Reference in this thesis/dissertation to any specific commercial products, process, or service by trade name, trademark, manufacturer, or otherwise, does not constitute or imply its endorsement, recommendation, or favoring by the University of Saskatchewan. The views and opinions of the author expressed herein do not state or reflect those of the University of Saskatchewan, and shall not be used for advertising or product endorsement purposes.

Requests for permission to copy or to make other uses of materials in this thesis/dissertation in whole or part should be addressed to:

Head of the Division of Biomedical Engineering
Room 2B60
57 Campus Drive
University of Saskatchewan
Saskatoon, SK S7N 5A9 Canada

OR

Dean
College of Graduate and Postdoctoral Studies
University of Saskatchewan
107 Administration Place
Saskatoon, Saskatchewan S7N 5A2 Canada

Abstract

Background: Worldwide, prostate cancer (PCa) is the most commonly diagnosed non-skin cancer in men. The current diagnostic standard of PCa requires invasive procedures such as needle biopsies. Non-invasive medical imaging techniques, such as Computed Tomography (CT), are only used as an adjunct for staging PCa. The development of a novel non-invasive imaging technique for PCa could revolutionize diagnostic standards and improve patient prognosis. The similarity between canine and human prostates, as well as similar PCa pathophysiology, makes the dog an ideal model for human PCa research. Initial investigations with Phase Contrast – CT (PC-CT) has shown potential for detecting morphological abnormalities in *ex vivo* canine prostates and therefore warrants further testing as a potential PCa diagnostic imaging technique.

This research addresses the design, development and implementation of a canine positioning device used for *in situ* prostate PC-CT imaging on the Biomedical Imaging and Therapy –Insertion Device Beamline at the Canadian Light Source. This device is currently being used to collect micron-level resolution PC-CT reconstructions of canine cadaver prostates. This thesis lays the ground work for canine imaging on the BMIT – ID beamline at the CLS. The design and implementation of the device are described, along with the issues discovered and addressed.

Acknowledgements

I would like to thank the many people who contributed to the success of this thesis, and who helped me through to the very end. I need to firstly commend my two supervisors, Dr. Elizabeth Snead and Dr. Murray Pettitt, for encouraging me to develop both professionally and personally, and for their tireless support. Without them and the rest of my graduate committee, Dr. Jaswant Singh and Dr. Dean Chapman, my thesis would not have been possible. So, thank you all.

I need to also make mention of the support from the University of Saskatchewan Prostate Research Group, in no particular order: Dr. Ali El-Gayed, Dr. Kishore Visvanathan, Dr. James Montgomery, Dr. Rajni Chibbar, Dr. Pritpal Malhi, Dr. Natalia Cardoso, and Dr. Michal Wesolowski. The first Tuesday of the month would not have been the same without you all. I would like to also give my thanks to the engineers and designers at RMD for their advice and expertise during my project.

A huge thank you to the BMIT beam-team for taking me under their wing and teaching me way, way, way more than anyone should ever know about synchrotron imaging. To Dr. George Belev, Dr. Ning Zhu, Dr. Adam Webb, Dr. Denise Miller, and Dr. Tomasz Wysokinski I give my undying gratitude for your support and effort.

To my family, without your support I would have washed out after the first week. Mom, thank you for always being there for me and encouraging me to be the best I can be. Kelsey, Wes, and Zach, I’m glad you’ve got my back. To my friends, thanks for keeping me sane (mostly). It was rough but we got there.

Lastly, I need to acknowledge Marly, Bolt, Shy, Waldo, Patty, and Choco. I hope it’s true that all dogs go to heaven. Thank you for your sacrifice.

To Kevin
Who Will Be Missed Forever

Table of Contents

List of Tables

List of Figures

List of Abbreviations

°	---	Degrees
2D	---	Two-Dimensional
3D	---	Three-Dimensional
BM	---	Bending Magnet
BMIT	---	Biomedical Imaging and Therapy
CLS	---	Canadian Light Source, Inc.
CPSE	---	Canine Prostate Specific Esterase
CT	---	Computed Tomography
DRE	---	Digital Rectal Examination
FNAB	---	Fine Needle Aspiration Biopsy
FOV	---	Field of View
FPS	---	Frames per Second
GY	---	Gray
HGPIN	---	High-grade Prostatic Intraepithelial Neoplasia
ID	---	Insertion Device
ICU	---	Intra-urethral Catheter
IV	---	Intravenous
LGPIN	---	Low-grade Prostatic Intraepithelial Neoplasia
MRI	---	Nuclear Magnetic Resonance Imaging
PBI	---	Propagation Based Imaging
PCa	---	Prostate Cancer
PC-CT	---	Phase Contrast – Computed Tomography
PCI	---	Phase Contrast Imaging
PIA	---	Proliferative Inflammatory Atrophy
PIN	---	Prostatic Intraepithelial Neoplasia
POE	---	Primary Optic Enclosure
PSA	---	Prostate Specific Antigen
TAUS	---	Transabdominal Ultrasound
TRUS	---	Transrectal Ultrasound
TURP	---	Transurethral Resection of the Prostate
US	---	Ultrasound
USPT	---	University of Saskatchewan Prostate Research Team

Chapter 1: Introduction

1.1 *Overview*

In Canada and worldwide, prostate cancer (PCa) is the most commonly diagnosed non-skin cancer in men (3). It is estimated that in 2015 approximately 24% of all new cancer cases in men will be PCa. In Canada, PCa is the third leading cause of cancer deaths in men. When PCa is detected in the early stage of the disease the five-year relative survival rate is 96%, meaning that most men will die with PCa, but not due to PCa. Unfortunately, if PCa is detected in the later stages of the disease, the five-year relative survival rate drops to around 31% (3). Therefore, the early detection of PCa is key to a favorable prognosis.

The current diagnostic strategy of PCa involves multiple invasive tests, usually needle biopsies, which are not 100% accurate (4). The false negative rate for prostate biopsy is between 20-24% (5), (6). The probability of detecting PCa using needle biopsies is subject to random sampling error, and introduces doubts about diagnostic accuracy (7). Needle biopsies also come with a variety of risks including hematuria, infection, hospital admission and even death (4). Unfortunately, the diagnostic gold standard of PCa is histological evaluation, which requires an invasive biopsy to obtain prostate tissue (4), (8).

Currently non-invasive medical imaging techniques, such as Magnetic Resonance Imaging (MRI), Computed Tomography (CT) and Ultrasound (US) are only used as an adjunct for staging PCa (7)**.** Low image resolution with conventional medical imaging modalities prevents clear distinction between intra-organ tissue types and cellular morphologies, preventing pathologists from visually diagnosing PCa (9). In the past twenty years, synchrotron X-ray imaging has emerged as a novel way for high resolution imaging of biological tissues and samples (10), (11), (12). As a uniquely precise source of X-rays, synchrotrons allow for imaging with resolution orders of magnitude greater than that of conventional imaging modalities, potentially allowing for the visualization of cellular morphologies (13).

Previous research on PCa has been conducted at the Canadian Light Source Inc. (CLS), Canada’s first and only synchrotron. Excised prostates have been imaged on the Biomedical Imaging and Therapy (BMIT) – Bend Magnet (BM) beamline, with a resolution of 17 micrometers (14). The positive results of this initial research lead to the goal of imaging *in situ* prostates on the BMIT-Insertion Device (BMIT-ID) beamline. Due to the nature of the research, dogs were selected as models for human PCa. Human and canine prostates have similar morphologies, biological behavior, and both species spontaneously develop prostate cancer contributing to the advantage of the dog model (15).

1.2 *Specific Objective*

The specific objective of this research was to design, develop and implement a canine positioning system for the BMIT-ID beamline, capable of imaging *in situ* dog prostates in both cadaver and live dogs. This design was developed based on specific performance specifications, some of which included vertical positioning of the dog for imaging, proper restraint of the dog and anesthetic equipment capabilities. Through this thesis the design and implementation of the canine positioning system is evaluated. The University of Saskatchewan Animal Research Ethics Board, operating in accordance with the guidelines set out by the Canadian Council on Animal Care, has reviewed and approved the use of live animal subjects and animal tissues for the purposes of this thesis. Chapter 2 examines the current understanding of human and canine prostate anatomy and pathology, as well provided justification for the use of dogs as a model for human PCa. In chapter 3 the general concepts of radiology and synchrotron imaging is discussed, and background is provided on the use of PC-CT for *in situ* imaging.

Chapter 4 presents the design process for the canine positioning device, along with the background information of the detectors used for PC-CT. In chapter 5 the implementation of the device is discussed, including cadaver and live dog imaging. Chapter 6 covers the conclusion of this thesis.

Chapter 2: Literature Review

This chapter overviews both human and canine prostatic anatomy and pathology, with the goal of identifying and discussing similarities and differences between the two species. The general morphology and histology of the human prostate is examined first, then an examination of several common human prostatic pathologies, including PCa, followed by a review of the diagnosis of human PCa. The second half of this chapter focuses on canine prostate anatomy and pathology, canine PCa and diagnosis, and directly compares and contrasts human PCa against canine PCa. The canine model for human prostatic disease concludes this chapter and justifies why dogs were chosen to study human PCa,

2.1 *Human Prostate Anatomy*

The prostate is an accessory sex gland of the male genitourinary system that produces and secretes components of the seminal plasma. It is believed that prostatic secretions are important for spermatozoa survival in the female reproductive tract, though the exact role and function of prostatic fluid are poorly understood (3).

The prostate gland is enclosed by a capsule, approximately 0.5mm in thickness. The capsule is composed primarily of collagen, elastin and smooth muscle. The bulk of the glandular prostatic tissue is situated posteriorly and bilaterally in the prostate. A fibromuscular stroma composes the anterior third of the prostate. The urethra runs the length of the prostate; approximately 3cm in length. The urethra is lined by transitional epithelium, and is situated closer to the anterior surface of the prostate. The urethra is divided into proximal (preprostatic) and distal (prostatic) segments. At the neck of the bladder, circular detrusor muscle fibers project distally around the preprostatic urethra, forming the internal urethra sphincter. The seminal vesicles and vasa deferentia enter through the prostate parallel and posterior to the postprostatic urethra to form the ejaculatory ducts (16), (17).

There are four distinct regions and a fibromuscular compartment recognized within the human prostate (Figure 2.1). These areas differ in their respected patterning of acini, as well as their susceptibility to disease. The four regions of the human prostate are the peripheral, the central, the transitional, and the periurethral zones. The peripheral zone of the prostate contains approximately 75% of the prostates glandular elements, and occupies most of the posterior and lateral aspect of the gland. In the normal prostate, the central zone contains approximately 25% of the glandular elements and is located circumferentially around the openings of the ejaculatory ducts. Approximately 5-10% of glandular elements are found in the transitional zone of the prostate. A thin fibromuscular band separates the transitional zone from other prostatic zones. Finally, approximately 1% of glandular elements compose the periurethral glands. Scattered along the proximal length of the urethra, the small periurethral glands are enclosed between fibers of longitudinal smooth muscle, and are contained within the preprostatic sphincter (17).

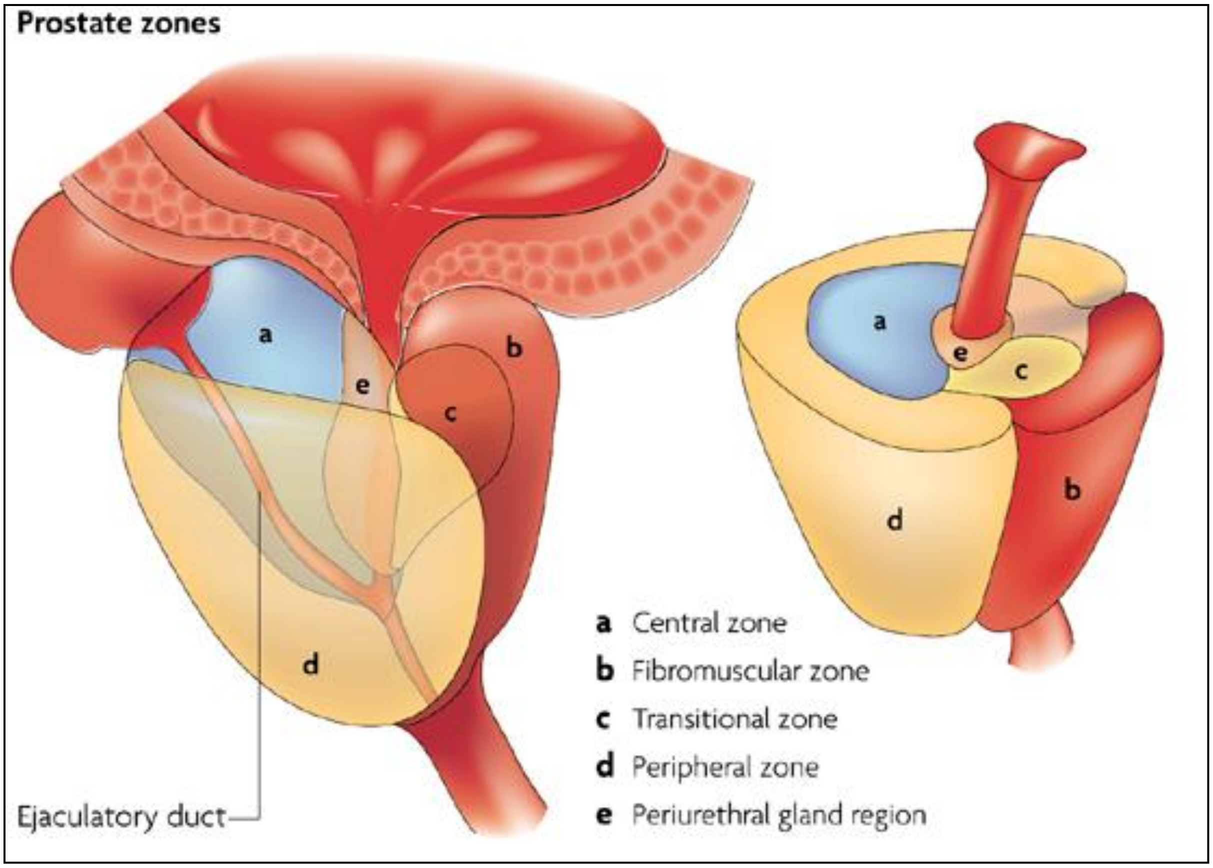

Figure 2.1: The four glandular zones of the prostate, and the anterior fibromuscular zone. The ejaculatory ducts are shown here as well (18). Reprinted with permission.

Approximately 70% of the volume of the prostate is composed of secretory glands, with the fibromuscular stroma composing the remaining 30% (16). These secretory glands are tubuloalveolar, extending from the capsule of the prostate and emptying into the urethra. The secretory glands have simple branching patterns with the main ducts surrounded by acini. The acini and ducts are lined by simple cuboidal or columnar epithelium containing abundant secretory granules. Between the secretory epithelium and basement membrane are small flattened basal cells, forming a nearly continuous layer. Neuroendocrine cells are also scattered throughout the epithelium of the ducts and acini, though their exact function and origin remain obscure. The stroma of the prostate is primarily composed of fibrillar collagen, elastin, and smooth muscle. The secretory cells of the ducts and acini have large, irregular nuclei. The luminal surface of the ducts and acini is also irregular, with frequent secretory cells projecting into the lumen (19).

2.2 *Human Prostate Disease*

Adenocarcinoma accounts for 95% of all diagnosed PCa cases (3). Adenocarcinoma of the prostate arises from gland cells and is usually multifocal, i.e. there are multiple sites of tumor growth located throughout the prostate (3). Benign prostatic hyperplasia (BPH) is a common non-cancerous enlargement of the prostate caused by an increase in the number (hyperplasia) and size of cells (hypertrophy) (20). Almost 90% of men will have experienced some BPH occurrence by the time they reach their 80’s (20). There are also two precancerous conditions that can develop within the prostate: prostatic intraepithelial neoplasia (PIN), and proliferative inflammatory atrophy (PIA) (3), (21).

2.2.1 *Adenocarcinoma*

Most adenocarcinomas are located in the peripheral zone of the prostate, the largest of the three zones of the prostate (17). Adenocarcinomas are cancers of glandular epithelial cells. There are other rarer types of prostate cancers including, transitional cell carcinoma, sarcoma of the prostate, small cell carcinoma, ductal carcinoma, mucinous carcinoma, large duct carcinoma, basal cell, and primary lymphoma of the prostate (3). A sarcoma is a cancer originating in connective tissue, while a lymphoma is a cancer of lymphatic tissue. Cancers originating elsewhere in the body, such as stomach cancer can also metastasize to the prostate (22). Adenocarcinoma is diagnosed via histology, and the Gleason classification system is used to grade the progression of disease (3). It is used to describe the aggressiveness of PCa, as well as the likelihood of metastasis of the cancer. The Gleason system is based on five histological and architectural patterns of tumor growth, most notably centered on the changes of the gland cells. The Gleason system is used to reflect the differences between normal prostate tissue and cancerous tissue. To determine the Gleason score, a biopsy of the prostate must be performed (3).

2.2.2 *Benign Prostatic Hyperplasia*

Growth in the prostate due to BPH occurs in the transition zone of the prostate, unlike adenocarcinoma (8). As men age the prostate naturally develops hyperplasia due to both an increase in stromal tissue and epithelial cell number and size, with almost all men in their 70’s experiencing some degree of prostatic enlargement (3), (8). BPH presents no early signs and symptoms; clinical manifestations only appear when the enlarged prostate begins to press on the urethra. The latter leads to changes in bladder habits (8). Pressure on the urethra from prostatic growth manifests as changes in bladder habits, notably frequent urination, which can progress to difficulty urinating and painful urination as BPH progresses (23). Symptoms of BPH can be treated non-surgically with Alpha-Blockers, which induce smooth muscle relaxation of the prostate, bladder neck and urethra, increasing urine flow through the urethra (24). When symptoms become severe enough, and medication is no longer a viable treatment option, a transurethral resection of the prostate (TURP) is usually performed. TURP is the invasive surgical removal of tissue from the area surrounding the prostatic urethra to reduce prostate size and decrease prostatic invasion of the urethra. A specialized tube is inserted through the urethra to the prostate, and excess prostatic tissue, including the epithelial cells surrounding the urethra are ablated, increasing the size of the constricted urethra. This procedure may have to be repeated again several years after the initial surgery if symptoms return due to subsequent prostatic hyperplasia (8).

2.2.3 *Prostatic Intraepithelial Neoplasia*

Prostatic intraepithelial neoplasia (PIN) is a multifocal, multi–grade condition that arises from the epithelial cells that line the ducts and the acini inside the prostate. There are two grades of PIN, low-grade PIN (LGPIN) and high-grade PIN (HGPIN). HGPIN occurs when the nucleus of epithelial cells become enlarged, and increased cellular proliferation causes the ducts to fill with excess epithelial cells. LGPIN shows similar cytological changes to HGPIN, and is regarded as a part of the spectrum of changes seen in benign prostatic tissue, though not as clearly pronounced. LGPIN show tufted crowding, stratification and irregular spacing of luminal cells, but without a large increase in nucleoli seen in HGPIN (25), (26). HGPIN is easily identified with a biopsy and histological evaluation due to the increased nucleoli located within duct structures throughout the prostate. HGPIN shares many similar characteristics to PCa, including cytological changes, increased incidence with age, and increased occurrence in the peripheral zone. Unlike PCa however, HGPIN does not increase serum Prostate-Specific Antigen (PSA) levels (21), (27). Recent studies have shown that men with HGPIN had an increased risk of PCa diagnosis during a secondary follow-up biopsy, as compared with men whose initial tests revealed only LGPIN (3), (8), (21), (25). Due to poor interobservation between pathologists and a clear link to PCa, LGPIN is not seen as a diagnostically useful pathological observation (28).

2.2.4 *Proliferative Inflammatory Atrophy*

In humans as well as dogs, Proliferative Inflammatory Atrophy (PIA) is suspected of being a precursor to PCa (27). Inflammation of the prostate caused by pathogens or pro-inflammatory cytotoxic agents cause proliferation of prostatic glandular cells. The damage, inflammation, and subsequent regeneration of glandular cells is thought to induce PCa generation (29). This proliferation of glandular cells leads to the appearance of nuclear disorder, large nuclei and nucleoli within glandular cells. These areas of dysplasia are associated with both chronic inflammation and epithelial cell proliferation, and are usually found adjacent to HGPIN and PCa (30). Genetic material in the epithelial cell may become damaged due to the release of reactive oxygen species during chronic inflammation, which might lead to PIN, and eventually adenocarcinoma (18), (30).

2.3 *Diagnosis of Prostate Cancer in Humans*

2.3.1 *Digital Rectal Examination*

A digital rectal examination (DRE) may be used by a physician to palpate the prostate to determine if there are any structural abnormalities. A gloved finger is inserted into the rectum of the patient and the peripheral zone of the prostate is palpated. The examiner assesses the size, symmetry, shape and consistency of the posterior surface of the prostate. Abnormalities of the prostate felt during DRE include nodularity, induration and asymmetry. Small tumors or those near the anterior surface of the prostate may go unnoticed during DRE. The tenderness and presence and consistency of any nodules is also assessed. The normal prostate is free of nodules with a palpable median sulcus separating the lateral lobes. A DRE test is often performed as part of a general annual checkup for men over the age of 50, or earlier for men who have a family history of prostate cancer (1). If abnormalities are felt, more tests are recommended for the patient, usually a prostate specific antigen (PSA) test (1). The prostatic volume can also be estimated during DRE, though it is usually underestimated (30).

2.3.2 *Prostate Specific Antigen*

Prostate specific antigen is a protein synthesized by the epithelial cells of the prostate gland and is found in the serum of healthy men (3). The PSA test is a measurement of the blood PSA level, and was first used as a monitor for PCa treatment response and recurrence in the early 1980's. During PCa treatment, the level of PSA in the blood plasma can be used to gauge how effective the treatment was; a decreasing PSA level indicated a positive treatment response. If, post-treatment, the PSA levels began to rise, physicians interpreted this as a sign that there was a recurrence of PCa (31). In the 1990's the test was approved by the United States Food and Drug Administration as a screening aid for PCa diagnosis (32). The PSA molecule is normally found in the blood at very low levels, <4ng/mL, with serum PSA levels between 4-10ng/ml potentially indicating PCa (3), although approximately 66% of men with elevated PSA levels do not have PCa (25). Other prostatic diseases, such as prostatitis and BPH, may cause elevations of PSA levels, and could potentially cause false-positive test results (32). Although most incidences of PCa increase serum PSA levels, approximately 20% of men with clinically significant PCa will have normal PSA serum levels (33). Therefore, the use of PSA tests for PCa screening has been controversial for many years. In Canada, there were two peak yearly incidence rates of PCa following intensified screening activity using the PSA test in 1993 and 2001 (3). The Canadian Task Force on Preventative Health Care recommended that PSA not be used to screen men for PCa, as they found that the certainty of harm outweighed the potential benefits (33). One of the major factors in the taskforce's decision was both the inability of the PSA test to distinguish between benign and malignant cancer, as well as the between low-grade and high-grade cancers. Due to the PSA test's inability to accurately predict which patients with elevated PSA levels should undergo further testing, millions of Canadian men needlessly underwent prostate biopsies

(34). The results of the European "Randomized Study of Screening for Prostate Cancer" trial estimated that the PSA testing as a screening test for PCa led to an overdiagnosis of PCa in 40-56% of men (33). The task force also found that when using a threshold of 4.0ng/mL, the false positive rate was 19.8% in men screened for PCa using PSA levels. Men with false-positive test results were usually invited to undergo further invasive testing, potentially having multiple needle biopsies. Biopsy of the prostate carries with it multiple risk factors, including hematuria, infection, hospital admission and death (7), (33).

2.3.3 *Transrectal Ultrasound*

A transrectal ultrasound (TRUS) test may be performed on males who are experiencing symptoms associated with prostate disease, have elevated PSA levels, or if abnormalities are felt during a DRE. An ultrasound transducer is inserted into the rectum of the patient, and the prostate and surrounding tissue are displayed on the ultrasound monitor. A TRUS test is used to visualize the size of the prostate, as well as to see if there are any structural abnormalities. TRUS may also be used to guide a biopsy needle to collect samples from abnormal areas of the prostate (3), (35).

2.3.4 *Needle Biopsy*

A biopsy of the prostate is required to accurately diagnose PCa. A prostate biopsy may be performed if abnormalities were felt during a DRE or seen with TRUS (3), (7). A biopsy may also be performed if high levels of PSA are detected; but there have been recent recommendations to move away from this practice, see section 2.3.2 (33). During a prostate biopsy, tissue samples are taken from multiple sites; usually 6-12 locations (27). Approximately 20-24% of needle biopsies result in false negatives, as abnormal areas may be overlooked, missed or under sampled (3), (21), (27). A false negative result is a term used to describe a situation in which a diagnostic test, such as needle biopsies, showed a negative or normal result, when in fact the patient had a positive test result. During a transrectal biopsy a specialized biopsy needle is inserted into the rectum and passes through the wall of the rectum into the prostate where tissue samples are collected. Transrectal ultrasound is usually used to visualize the location of the prostate and guide the needle during sample collection. Potential side effects of the biopsy include pain, infection, and bleeding (7). The results of a prostate biopsy are used to determine whether PCa is present or not, and if cancer is present, to describe the type and aggressiveness of the cancer using the Gleason classification system (3).

2.3.5 *Histopathology of Prostate Cancer*

Several microscopic features form the basis for the histopathological diagnosis of PCa. There are both primary and secondary criteria for diagnosis, with no specific feature being indicative of PCa, except for perineural invasion (36). Perineural invasion is the presence of malignant adenocarcinoma glands in the perineural space, i.e. the periphery of cells surrounding the nerves passing through and innervating the prostate. The primary criteria refer to the pattern or architecture of the glands. Normal prostatic glands are arranged in lobules, and are medium in size. Malignant glands are found to be typically small, forming microacini, arranged haphazardly, overcrowded, have lost their lobule formation, are fused together, and have invaded between benign glands (36). The secondary features of PCa are cytological, and include the presence of hyperchromatic nuclei, the absence of the basal cell layer, and glands crowded with cells. The grading of PCa is based on the deviation of malignant glands from normal histological morphology, with the Gleason grading system being the internationally accepted standard. In 2005, the Gleason classification system was updated to better accommodate current diagnostic practices through the International Society of Urological Pathology (ISUP) Consensus Conference (37). In 2013 a new system of PCa grading was proposed, consisting of five grade groups, with group five indicating the least favorable prognosis and group one the most. This proposed five group grading system is in contrast to the Gleason system, where there are 25 potential grading combinations. The new PCa grading system was validated with a retrospective study of 25000 men between 2005 and 2014 who received PCa treatment either with radical prostatectomy or radiotherapy. The study concluded that the contemporary PCa grading system has several benefits over the Gleason system including: simplified grading, improved stratification between grades, and potential reduction in PCa overdiagnosis (38).

2.4 *Canine Prostate Anatomy*

The prostate gland of dogs sits at the caudal neck of the bladder with the urethra traversing through it (39), (40). The gland is bound ventrally by the symphysis pubis and ventral abdominal wall, and dorsally by the rectum. The dorsal and ventral portions of the prostate are separated by the two folded layers of the peritoneum bounding the rectogential space. The urethra passes through the dorsal center of the prostate gland. Contrary to the human prostate, the canine prostate is not divided into zones (41). A median septum divides the canine prostate gland into left and right lobes. The left and right lobes are further divided into lobules by capsular trabeculae. Each lobule consists of many compound tubuloalveolar glands. The tubuloalveolar glands are lined by columnar epithelium, similar to in the human prostatic gland. The ducts from the tubuloalveolar glands empty into the urethra (39). The size of the prostate gland varies with the age and weight of the dog (42), (43).

The prostate gland is located in the caudal abdomen or pelvic cavity depending on the size and age of the dog. In dogs less than two months of age the prostate gland is typically found in the abdominal cavity, before the urachal vestige breaks down allowing the prostate to move caudally into the pelvic cavity. During puberty, around 5-8 months of age, the prostate gland begins to enlarge and the gland starts to move cranially back toward the pelvic brim. By four years of age hyperplastic enlargement of the prostate results in a further shift of the gland cranially into the abdominal cavity; at this age the prostate typically is located equally within the abdominal and pelvic cavities. Usually by ten years of age in an intact dog the entire prostate gland has shifted into the abdominal cavity (41).

As in humans, the exact function of the canine prostate gland is not entirely understood. The canine prostate gland secretes citrate, lactate, cholesterol, and enzymes. It is commonly believed that the glandular secretions help to create an optimum environment for sperm survival within the female reproductive tract (39)

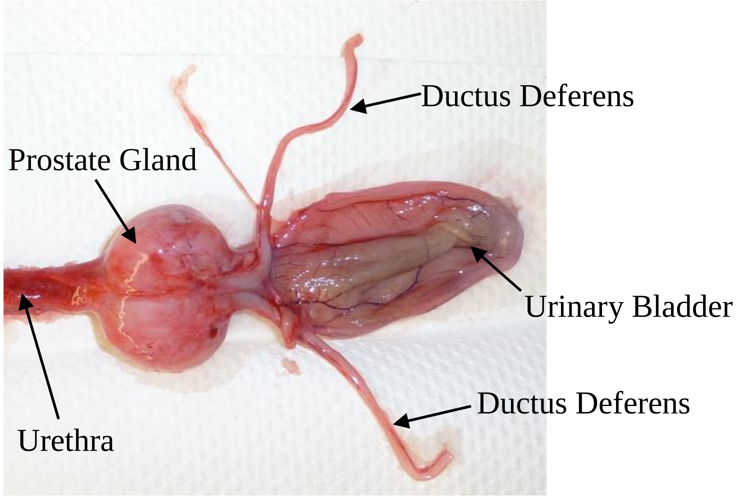

Figure 2.2: The gross anatomy of the canine prostate.

2.5 ***Canine Prostate Disease***

2.5.1 *Prostatic Neoplasia*

There are two major types of prostatic neoplasia diagnosed in dogs, adenocarcinoma and transitional cell carcinoma, with adenocarcinoma more commonly diagnosed than transitional cell carcinoma (42). Transitional cell carcinoma originates from urethral cells, while adenocarcinoma originates from glandular cells within the prostate (44). Immunohistochemistry of specific prostate cellular markers are needed to distinguish adenocarcinoma from transitional cell carcinoma (42). There are a large range of cellular markers used to differentiate the two types of neoplasia, with PSA being a primary marker between high-grade transitional cell carcinoma and adenocarcinoma (45). Prostatic neoplasia is usually not diagnosed until clinical signs of the disease are present, frequently with local or regional metastasis occurrence. Adenocarcinoma of the prostate is usually diagnosed in 8-10-year-old dogs, with a much lower incidence rate in younger dogs (46). Castration does not appear to affect the prevalence of prostate neoplasia, as castrated and intact dogs have the similar occurrence rates of the disease (39), (47). Clinical signs of prostatic neoplasia include anorexia, weight loss, stranguria, hematuria, tenesmus, and weakness of the rear limbs (47). As in humans, metastases occur to regional lymph nodes and the pelvic bone (39). Through transrectal examinations, the prostate of affected dogs is typically revealed to be irregular, enlarged and asymmetrical (42), (47). Canine adenocarcinoma mimics human PCa in heterogeneity, increased prevalence in older patients, histopathology of disease and association with skeletal metastasis (48). The incidence of adenocarcinoma in humans and canines similarly increases with age (48), (49). The median age of adenocarcinoma in dogs is 10 years, which is approximately equivalent to the average age of diagnosis in human men, 70 years, when converted to human years (49). Human and canine PCa may metastasis to bones, causing osteoblastic lesions in both species (50), (51), (52).

2.5.2 *Prostatic Hyperplasia (Benign Prostatic Hyperplasia)*

As in humans, the canine prostate gland increases in size with age, with 95% of all intact dogs affected by the age of 9 (47). One study found that 50% of beagle dogs in their cohort developed BPH by the age of 5, suggesting a difference of incidence between species (53). The canine model of BPH is currently the only model for human BPH, with sufficient similarities between the pathology and anatomy of both species to consider it a reliable comparison (54), (55), (56). The incidence of BPH is also age related in both species, similar to PCa (53). One of the only differences in pathophysiology of BPH between the species is that the human disease is characterized by hyperplasia of the stromal cells within the periurethral space, whereas in canine BPH there is diffuse epithelial or glandular proliferation throughout the entire prostate (49), (54). Most cases of canine BPH do not show clinical signs, but occasionally the enlargement can cause hematuria or tenesmus, as well as urethral discharge, hemospermia, or a silted gait (42), (47). Definitive diagnosis of BPH in dogs can only be made with a needle biopsy, though a presumptive diagnosis is often made based on history, DRE, and/or ultrasonographic appearance of the prostate gland. Castration is the most effective treatment, causing a 70% reduction in prostate size following surgery, with completed involution taking up to four months (42).

2.5.3 *Prostatic Intraepithelial Neoplasia*

Similar to humans, canine prostatic intraepithelial neoplasia (PIN) is an atypical epithelial lesion of the prostate considered to be a precursor of prostate cancer (52), (30). PIN is a multifocal, multi–grade condition that arises from the epithelial cells that line the ducts and the acini inside the prostate. High grade PIN (HGPIN) is considered to precede PCa in both dogs and humans (57), (58). Histologically, canine HGPIN is similar to human HGPIN, with proliferation of the luminal secretory cells lining pre-existing ducts, and characteristic cytological changes and abnormalities including nuclear crowding, variation in nuclear size and enlargement of nucleoli (59), (60). The disruption of the basal cell layer, increase in proliferative index and increase in micro-vessel density characterize both human and canine HGPIN (60). The prevalence of HGPIN in dogs seems to be influenced by sexual status with one study reporting HGPIN in 55% of intact dogs compared to only 9% in castrated dogs (57), (58).

2.5.4 *Proliferative Inflammatory Atrophy*

Canine and human proliferative inflammatory atrophy (PIA) share many characteristic histological features, including: discrete foci of hyperchromic glands, acini glands having two layers of epithelial cells with the luminal layer of cells appearing as attenuated cuboidal cells, and atrophic acini glands appearing to have only one layer of attenuated epithelial cells (61), (60). PIA is seen as a preneoplasitc lesion in both humans and dogs (60). The proposed method of carcinogenesis involves a chronic cycle of tissue damage and regeneration, with prolonged reactive oxygen species exposure causing oncogenic changes to the cellular DNA (27), (61). Several studies have found evidence of PIA in canine prostates, suggesting it is not an uncommon disorder, and may be reasonably well detected with routine biopsy (61).

2.6 *Diagnosis of Prostate Cancer in Canines*

2.6.1 *Prostate Specific Antigen & Canine Prostate Specific Esterase*

In humans, serum prostate specific antigen (PSA) levels can be a useful screening tool for facilitating PCa diagnosis (33). PSA is a proteolytic glycoprotein found in normal, hyperplastic and malignant human prostatic tissue, and can be found in similar canine prostatic tissue using immunohistochemical techniques (62). Though detectable in human serum, PSA is not detectable in canine serum, and therefore its use as a screening tool for canine PCa is not recommended (62), (63). Canine prostatic tissue secretes an enzyme called canine prostate specific esterase (CPSE), a proteolytic glycoprotein similar to PSA, though different in their respective enzymatic activity and substrate binding (62). Both PSA and CPSE are under hormonal regulation, with decreases in serum testosterone levels resulting in decreases in serum SPA and CPSE levels, while increasing levels of testosterone increases the levels (63). CPSE has been identified in normal, hyperplastic, and malignant canine prostatic tissue, similar to PSA in humans (62). Bell et al. (1995) found the mean serum CPSE concentrations were higher for dogs with BPH, but found no statistically significant difference between healthy dogs and those with PCa (62). Neither PSA or CPSE are considered useful screening tool for PCa diagnosis in dogs.

2.6.2 *Digital Rectal Examination*

A physical examination, called a digital rectal examination (DRE), of the canine prostate is a basic non-invasive screening test for prostate abnormalities such as BPH and PCA (64). The veterinarian inserts a gloved finger into the rectum of the dog while applying pressure to the abdomen and palpates the prostate. The normal canine prostate should have a smooth surface, solid consistency free of nodules, be isothermic and not cause pain to the dog during palpation (63). The symmetry of the prostate gland is evaluated during a DRE, using the central sulcus on the dorsal surface of the gland to determine the bilateral symmetry of the prostate. The left and right lobules of the prostate in a normal canine prostate are similar in size. If abnormalities are felt during a DRE, the veterinarian should investigate further (63).

2.6.3 *Transabdominal Ultrasound*

Transabdominal ultrasound (TAUS) is used for visualizing the internal architecture, external texture and structural features within the prostate. Similar to humans, ultrasonography is used for performing percutaneous or aspiration biopsy of the canine prostate. The length, width and depth of the prostate gland can be determined using TAUS, allowing for a volume estimate to be made (65). If abnormalities are suspected, such as BPH or PCa, the volume of the prostate can be monitored overtime for any change. The prostate is normally displayed with a homogenous pattern during TAUS, but an inflamed, hyperplastic or neoplastic prostate loses this homogenous pattern (66). TAUS has been successfully used to establish a preliminary diagnosis, and is routinely used as a screening tool for prostatic disease (67).

2.6.4 *Fine Needle Aspiration & Prostatic Biopsy*

Fine needle aspiration (FNA) is a minimally invasive procedure to collect prostatic tissue for bacterial cultivation and/or cytology. TAUS may be used to enhance the effects of FNA by allowing for better targeting of questionable tissue (68). The prostate gland can be approached and sampled through the perineum, caudal abdomen, perirectum and rectum (63), (42). As in humans a specialized needle is inserted into the prostate and tissue samples are collected. The reliability of FNA in PCa diagnosis is approximately 80%, but can reach up to 89% (69).

The gold standard for determining prostatic disease in dogs is a histological evaluation of a prostate biopsy (67). A prostate biopsy is a more invasive diagnostic test compared to FNA (63).A prostate biopsy is performed in cases where less invasive diagnostic tests do not render a diagnosis, such as TAUS, DRE and/or FNA, or in cases were an immediate diagnosis is needed (42). There are two main methods of prostatic biopsy: percutaneous and excisional (i.e. during surgery). As in FNA, percutaneous biopsies can be collected through the perineum or transabdominally, though the patient is sedated or anesthetized (39). The procedure is most often guided by ultrasound, but can be performed blindly if performed tranrectally (67). The samples collected can be cultured and evaluated both cytologically and histopathologically for prostatic diseases and abnormalities.

2.6.5 *Histopathology of Canine Prostate Cancer*

The canine prostate gland is composed of tubuloalveolar structures of glandular components surrounded by a smooth muscle and connective tissue stroma (70). The normal epithelial cells of the prostate are well defined cuboidal or columnar cells, containing small nucleoli and an oval nucleus (71). In intact male dogs the acini are composed of luminal tall columnar and cuboidal secretory epithelial cells with a basal cell layer (70). In contrast to humans, the basal cell layer in dogs is discontinuous (71), (30). This lack of the continuous basal cell layer in humans is a strong indicator of PCa, yet in dogs is entirely normal, which is a specific histological difference between the two species (30), (37). As described previously, the human prostate gland contains four regions: the central zone, the peripheral zone, the transitional zone, and small periurethral glands (17). Conversely, the canine prostate does not exhibit zonal anatomy, though it contains a median septum which separates the prostate into the left and right lobes (72). In humans PCa arises primarily in the transitional zone of the prostate, while in dogs there is growing evidence to suggest that PCa originates from the ductular epithelium in the periurethral space (72), (73). HGPIN and PIA are believed to be precancerous histological changes in both human and canine prostates (52).

2.7 *Canine Model for Human Prostatic Disease*

Animal models have been used in the past to gain a deeper pathogenic understanding of multiple types of cancers, such as lymphoma, soft-tissue sarcoma, osteosarcoma, mammary gland carcinoma, and melanoma (15). Dogs represent a unique model to better understand PCa in humans, as both share many characteristics and morphologies. For example, dogs are the only other mammal besides humans that commonly develops spontaneous PCa and BPH (74), (75), (76). As discussed previously, human and canine BPH and HGPIN develop and progress similarly, and PIA is believed to be a histological precancerous lesion in both humans and dogs as well. There are also parallels between the diagnosis of PCa in each species. Both male humans and dogs produce a specific prostate protein detectable in serum, and although PSA and CPSE are distinct, they share a remarkable amount of similarities. The gold standard of PCa diagnosis, histology of prostate biopsy cores, is also the same between humans and dogs. There is also a similar tendency for PCa to metastasize to the bone in both humans and dogs (74), (75). In contrast, a major difference between the two species is the continuity of the basal cell layer around the epithelial glandular lining of the prostate.

Considering these resemblances, dogs can allow us to test and perfect the positioning device on the BMIT-ID beamline before modifying it for human imaging in the future. The canine positioning device will be used to generate a considerable amount of data on both living and cadaver canine prostates. Synchrotron imaging may provide a unique insight into the pathophysiology of prostatic diseases in dogs, and can be used to study BPH, HGPIN and PCa development. The device will allow for future canine studies to be conducted on the BMIT-ID beamline, not just for prostate imaging research.

Chapter 3: Medical Imaging & Synchrotron X-ray Source

3.1 *Overview of Conventional Medical Imaging*

A general concept and understanding of X-ray medical imaging is needed to appreciate the data collected for this thesis. This chapter overviews X-ray medical imaging, including the generation of X-rays using a synchrotron. An introduction on how X-rays are used to generate contrast within an object begins Chapter 3, followed by a section on computed tomography and phase contrast - computed tomography, as this was the method used to collected *in situ* canine prostate reconstructions.

3.1.1 *Introduction to Radiography*

X-ray images are formed via the differential attenuation of the X-rays as they pass through a sample. Variation in thickness and density within the sample cause fluctuations in the transmitted X-ray intensity. Simply put, the amount of photons entering a sample is greater than the amount of photons leaving the sample due to the properties of the sample. According to the Beer-Lambert law, the ratio of photons passing through a sample to incident sample photons is related to the integral of the sample absorption coefficient and the distance the X-ray photons pass through the sample, given in the following equation (77).

$$\frac{I}{I_0} = e^{-\mu x} \qquad [3.1]$$

Where I_0 and I are the incident and transmitted beam intensity, respectively, μ is the linear attenuation coefficient, and x is the thickness of the sample. In uniform materials, the attenuation of the X-ray beam will be constant throughout the sample.

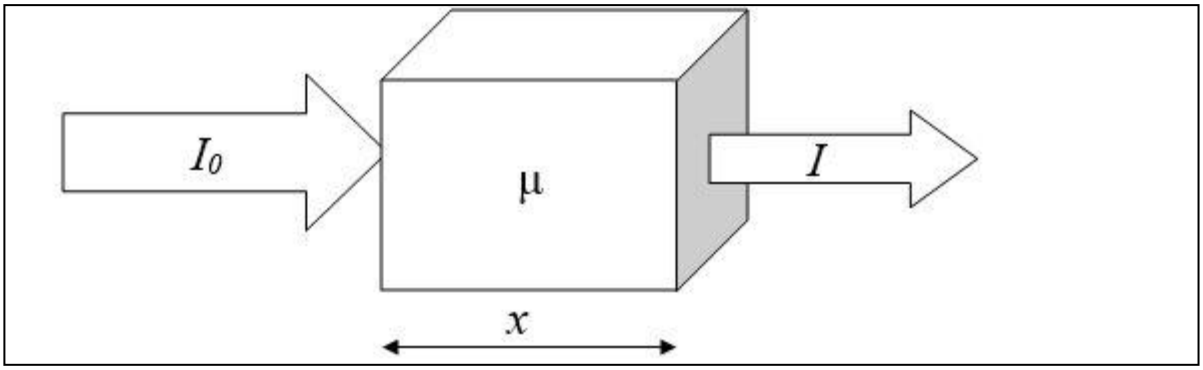

Figure 3.1: The linear attenuation of an X-ray beam I_0 by a homogenous object with μ linear attenuation coefficient and x thickness.

For heterogeneous samples, such as human tissue, the equation is modified to (77):

$$\frac{I}{I_0} = e^{-(\mu_1 x_1 + \mu_2 x_2 \ldots)} \qquad [3.2]$$

Where the product of the linear attenuation coefficient and thickness of each separate object are added together.

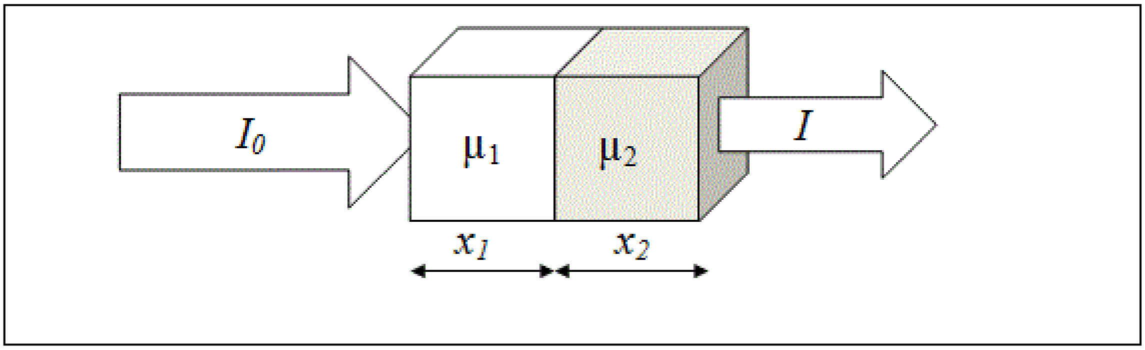

Figure 3.2: The linear attenuation of an X-ray beam $I_0$by a heterogeneous object with different linear attenuation coefficients μ_1 and $\mu_2$and thicknesses x_1 and x_2.

The linear attenuation coefficient of objects is energy dependent. This means each specific wavelength of photons passing through the sample will be attenuated by a different amount. As a general rule, the higher the X-ray photon energy, the lower the linear attenuation coefficient, meaning higher energy photons pass through materials preferentially, compared to lower energy photons. Due to the smaller absorption of high energy X-rays, the dose received during imaging is smaller compared to low energy X-ray photons. The linear attenuation coefficient can be described by two material properties: the linear attenuation coefficient (μ), and the density of the material (ρ_o). The mass attenuation coefficient (μ/ρ_o) of the material is more commonly found than the linear attenuation coefficient in the literature due to the mass attenuation coefficients ability to normalize same materials of different density, e.g. liquid versus ice water (78).

$$\mu = \frac{\mu}{\rho_o}\rho_o \qquad [3.3]$$

Contrast of objects embedded in a background material is defined as how much the object signal is detectable from the background signal. Contrast can also be described as the difference of pixel value in the image between an area of interest and the surrounding background. The contrast of an image depends on the characteristics of the material being imaged, as well as the general setup of any imaging process. Contrast can be further broken down and described as radiographic versus detector contrast for X-ray imaging. Detector contrast refers to the ability of the detector system to measure and convert photon count differences across the X-ray beam into an electronic signals representing the image. Radiographic contrast refers to the intensity *I* of the X-ray beam passing through different regions of the object being scanned. Radiographic contrast depends on a number of different physical properties of the material including atomic number, physical density, electron density, thickness, as well as the energy of the incident photon beam. For the purpose of this thesis, contrast will refer to radiographic contrast, as the parameters of detector contrast are outside the scope of this thesis. For X-ray radiography, the absorption contrast can be examined and explained using an object with μ_{object} linear attenuation coefficient, and x_{object} thickness embedded in matrix with μ_{Matrix} linear attenuation coefficient and x_{matrix} thickness, shown in Figure 3.3 (79).

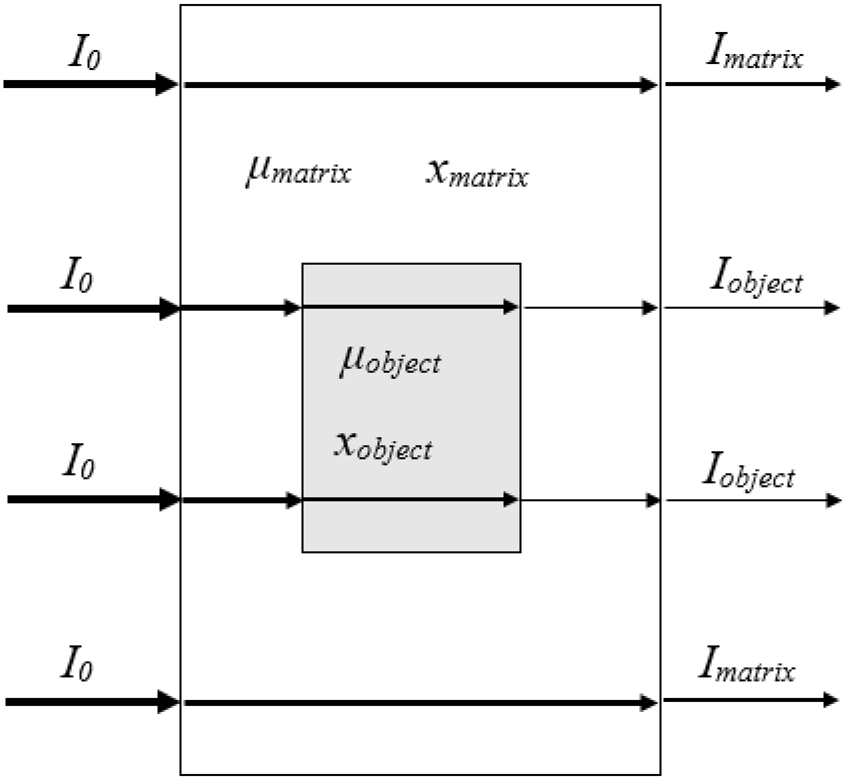

Figure 3.3: The linear attenuation of an X-ray beam I_0 through a matrix with an object embedded inside.

The contrast of this embedded object can be determined using the following formula, [4]. Inserting equation [1] and [2], the contrast formula becomes [5], which can be simplified to [6].

$$C = \frac{I_{matrix} - I_{object}}{I_{matrix}} \qquad [3.4]$$

$$C = \frac{I_0 e^{-\mu_{matrix} x_{matrix}} - I_0 e^{-\mu_{matrix} x_{matrix}} e^{-(\mu_{object} - \mu_{matrix}) x_{object}}}{I_0 e^{-\mu_{matrix} x_{matrix}}} \qquad [3.5]$$

$$C = 1 - e^{-(\mu_{object} - \mu_{matrix}) x_{object}} \qquad [3.6]$$

The contrast of an object is given by the absorption differences between the matrix and the embedded object, and the object thickness. As previously stated, the absorption of X-rays in material is dependent on the mass attenuation coefficient, density, and incident X-ray photon energy. Therefore, in samples of near homogeneous mass attenuation coefficient, such as cancerous and non-cancerous tissue, contrast relies heavily on density differences (79).

3.1.2 *Computed Tomography*

The word tomography comes from the Greek word “tomo”, meaning *to cut.* Computed tomography allows for the viewing of internal structures of an object without cutting the sample open. A viable clinical Computed Tomography (CT) scanner was first separately introduced by both Sir Godfrey Newbold Hounsfield and Allen McLeod Cormack in 1967. Computed Tomographic imaging technology builds on conventional radiology, though CT is not subject to the same limitations. In conventional radiography, three-dimensional (3D) objects within a sample are superimposed onto a two-dimensional (2D) image, causing confusion and interpretation issues for the viewer due to the silhouette effect. Computed tomography images on the other hand, provide cross-sectional images of the interior of the sample, enabling 3D information to be viewed through multiple 2D images. Digital processing of the consecutive 2D images can be performed to allow a 3D image to be constructed. Since its inception, CT has also provided high soft tissue contrast, enabling the visualization of different tissues and organs, compared to simple radiographs (80).

Tomography is based on the approach that detecting information from multiple angles around an object can be reconstructed into a section of the object. CT uses many radiographs taken at equidistant intervals 180° around an object to produce a section image of the object. The cross-section geometry of an object can then be visualized from hundreds of radiographs taken at slightly different angles, called tomographic projections, by processing using computer algorithms (77). This process is discussed in depth later in this section.

Conventional CT has evolved greatly since its inception in the 1970's (80). The clinical CT setup can be described as consisting of three principle components: The X-ray source, the object being imaged, and the X-ray detectors, Figure 3.4. The source and detector in conventional CT machines rotate on a gantry around the object being imaged, e.g. a human. The rotation of the X-ray source and detector allow for a 180° scan that collects contiguous tomographs of the subject being imaged. Conventional CT machines employ a cone beam projection X-ray source, which is contrary to a synchrotron X-ray source, which employs parallel beam projections, discussed further in the thesis.

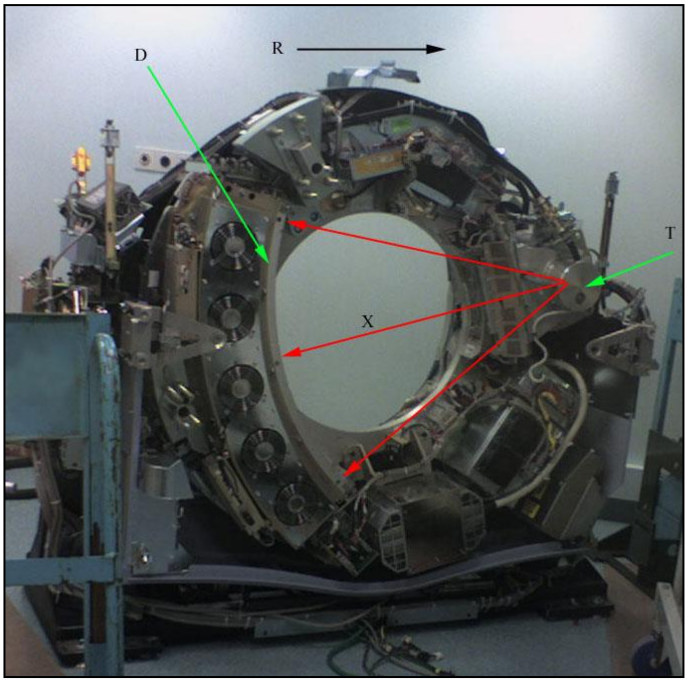

Figure 3.4: Internal components of a clinical CT machine, where T is the X-ray source, D is the X-ray detector, X is the cone path of the X-ray beam, and R is the rotation (clockwise) direction of the gantry (81). Reprinted with permission.

To discuss the tomographic reconstruction process, parallel beam geometry will be used. Each tomographic projection is the line integral representation of the total attenuation of the object at that particular angle. A line integral is the integral taken along the line of a function with a continuously varying value, such as the linear attenuation coefficient at each point in a sample being imaged with X-rays. Each row of pixels of a tomographic projection can be expressed as a function with respect to each of the pixel value and location (82).

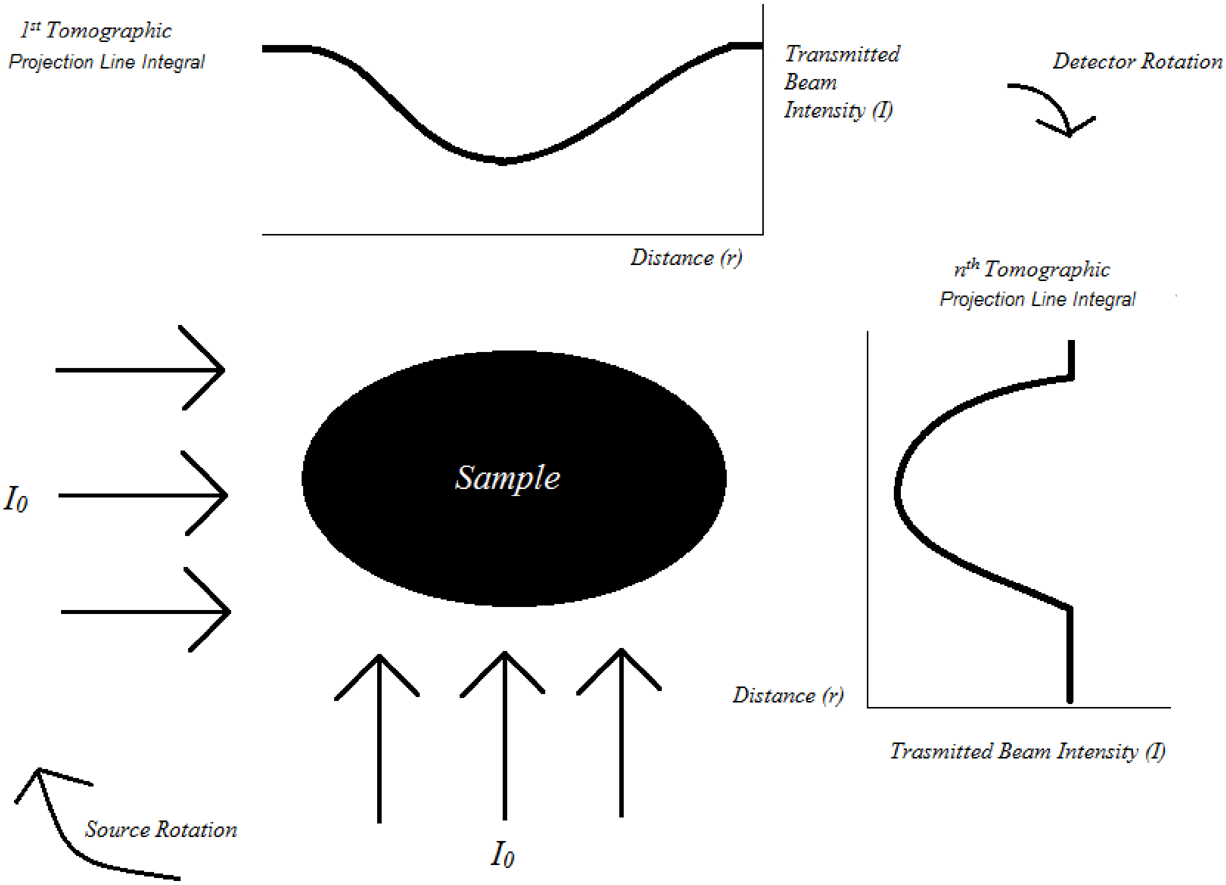

Figure 3.5: A visual aid to describe the collection of parallel beam tomographic projections where the source and detector rotate around the homogeneous sample. The transmitted beam intensity versus distance graphs in the figure show continuous lines of each pixel's line integral, i.e. the absorption of the X-ray beam path. Each function shows the total attenuation of the sample at two specific angles 90° to each other.

The final pixel value of the line integral is the summation of all the absorption occurring on the line through which the photons passed. In digital medical imaging, this value is expressed as a grey pixel value. The 2D representation of this can be seen as a typical radiograph, or in this case, a tomographic projection as seen in Figure 3.5. Following collection of the projection tomographs, computer algorithms are then used to reconstruct a sample slice from each of the line integrals (83).

There are several different computational methods to reconstruct the 2D sample slice from the series of tomographic projections. The following will briefly describe the Filtered Backprojection method, as this was the method used to reconstruct the data collected for this thesis. The method of Backprojection involves setting the projected tomograph pixel values equal to the ray lines along the path the tomograph was taken on. A backprojected image is formed by "smearing" the projections, also called views, back along the direction they were originally acquired on. The final reconstructed image is the sum of all the backprojected views. Unfortunately, this leads to blurring of objects and sample, as seen in Figure 3.6 (83).

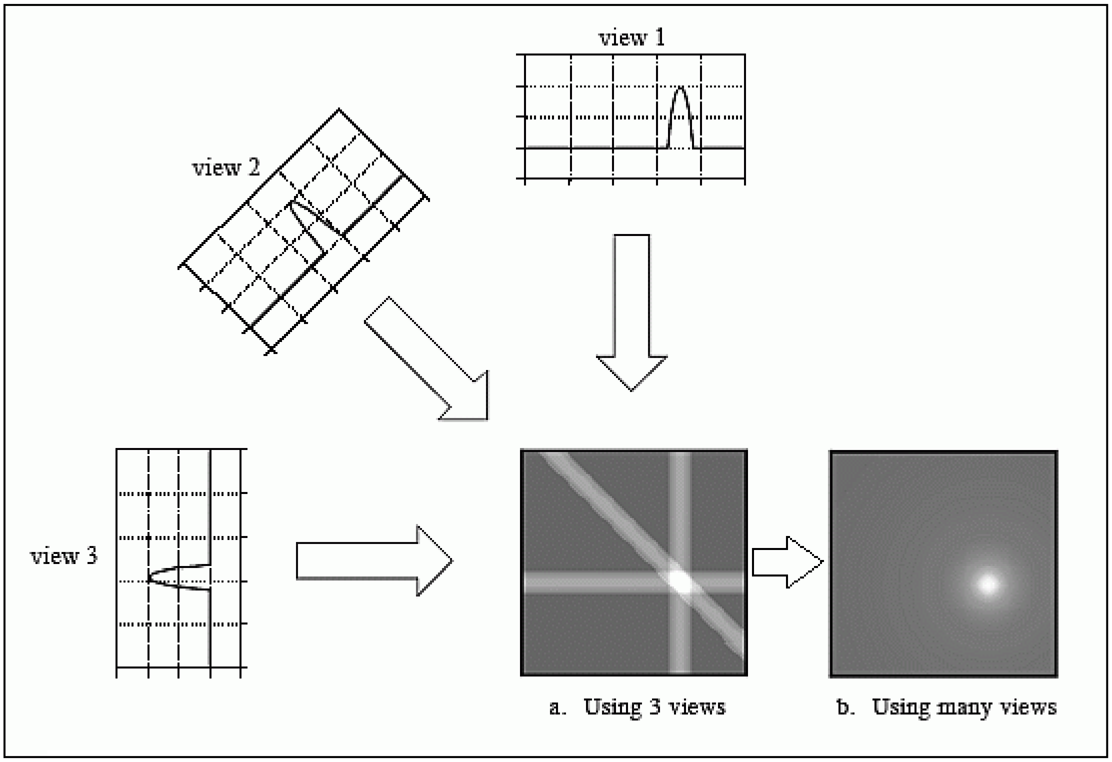

Figure 3.6: Backprojection method of CT reconstruction. The image (a) is generated by taking each tomographic projection (view) and “smearing” it along the path it was acquired on. (a) The reconstructed image is generated from three views;(b) The reconstructed image is generated using many views, blurring of the object is apparent (83). Reprinted with permission.

A single point within the real object being imaged is reconstructed as a circular ring of decreasing radial intensity, seen as a circularly symmetrical spread function decreasing with the reciprocal of the radius. Fortunately, this blurring effect can be overcome with filtering. This is called Filtered Backprojection, and is one of the most common tomographic reconstruction methods. In filtered Backprojection, each tomographic projection is convolved with a 1D filter kernel, creating a set of “filtered” projections. This means the function of transmitted beam intensity is multiplied by another function called the filter function. This convolving of the two functions creates new projection tomographs, called filtered projections or views. The filtered projections are then backprojected, i.e. smeared, as described above, creating a filtered reconstructed image. These filtered projections supply a closer reconstruction approximation to the real object being imaged compared to the unfiltered projections (83).

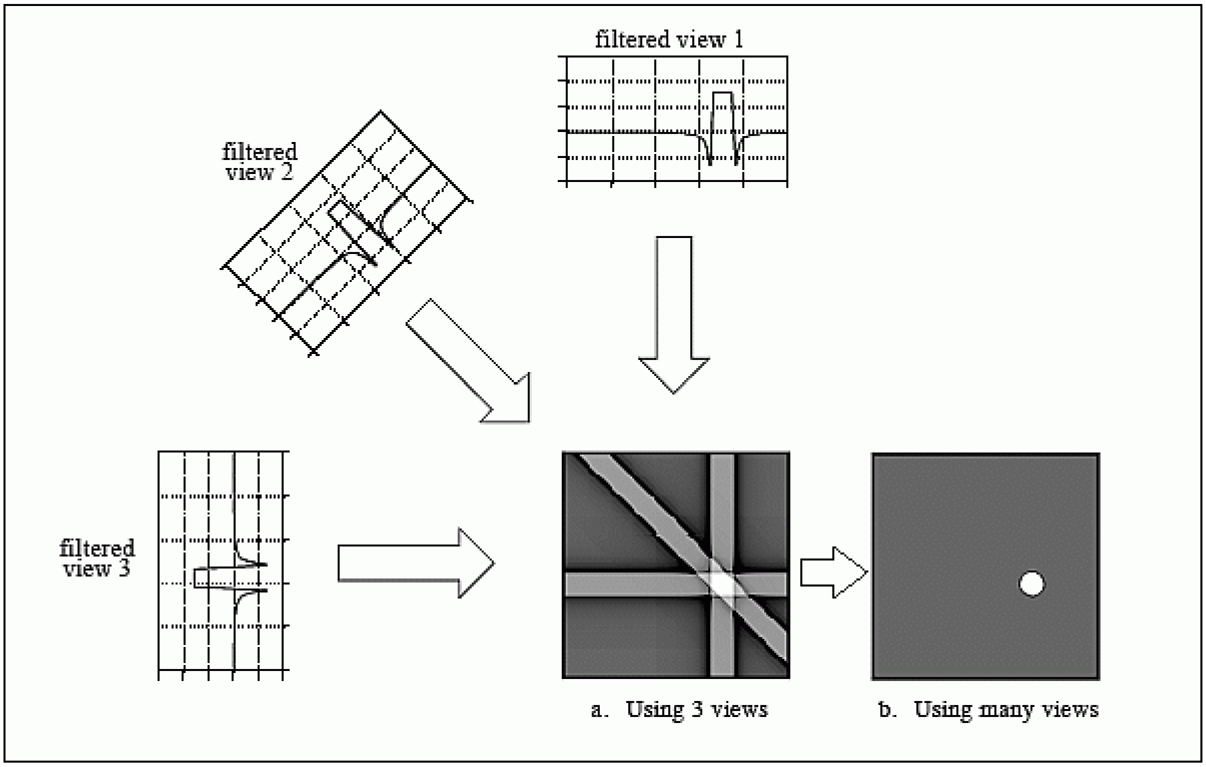

Figure 3.7: Filtered Backprojection method of CT reconstruction. The image is generated by taking each filtered tomographic projection (view) and “smearing” it along the path it was acquired on. a) The filtered reconstructed image is generated from three filtered views; b) The filtered reconstructed image is generated using many filtered views. Object blurring was removed with filtering (83). Reprinted with permission.

In fact, with an infinite number of projections taken of an object, the filtered Backprojection method can reconstruct the image perfectly. However, in a practical sense this is impossible, and therefore the reconstruction is just a very close approximation of the actual object. Each reconstructed slice is one row of the detector’s pixels, e.g. if the detector has a pixel array of 1000 x 200, up to 200 slices of the object could be reconstructed from a single scan.

3.2 *Synchrotron X-ray Source*

The Canadian Light Source Inc, located in Saskatoon, Saskatchewan was utilized as the X-ray source for the data collected in this thesis with the Biomedical Imaging and Therapy – Insertion Device Beamline (BMIT-ID) used to collect the data.

Synchrotron radiation is produced by accelerating relativistic electrons through bending magnets, superconducting wigglers or undulators (84). Wigglers and undulators are devices primarily composed of a series of alternating magnetic poles, which force an electron beam passing through them to conform to a characteristic sinusoidal trajectory. Electrons are produced by a linear accelerator and injected into a booster ring, which accelerates the electrons to near the speed of light, referred to as relativistic speeds. After the electrons gain relativistic speed, they are injected into a storage ring. The electrons travel in a near circular path inside the storage ring, which consists of straight sections and bends. The bending of the electron path is done using high-powered bending magnets. There are 24 bending magnets at the CLS, each altering the trajectory of the electrons by 15° in the transverse plane of the electron movement (85). As the relativistic electrons pass through the bending magnets, the magnetic field accelerates the electrons, forcing them to change direction, and causing them to emit electromagnetic radiation. The relativistic speed of the electrons causes this emitted radiation to be seen as hard polychromatic X-rays from a laboratory reference frame (12).

There are several insertion devices found within the straight sections of the storage ring at the CLS. These insertion devices incorporate a series of oppositely oriented magnetic poles. The electron beam passing though the insertion device is accelerated by the magnetic fields, causing the electrons to undulate in a sinusoidal fashion. The sinusoidal path of the electrons passing through the insertion devices produces polychromatic electromagnetic radiation. The polychromatic electromagnetic radiation, including hard X-rays, generated from either an insertion device or bending magnet are highly collimated in the transverse direction of the electron beam, and travel in tangent lines away from the storage ring. Specialized beamlines, tangent to the storage ring, house the radiation as it leaves the storage ring and travel to the imaging hutches at the end of the beamlines (1).

BMIT has two beamlines for x-ray imaging, the insertion device (ID) beamline, and the bending magnet (BM) beamline. They are named after the device used in the storage ring to produce X-rays. A 4.3 max Tesla (T) superconducting wiggler is the source of X-rays on the ID beamline. BMIT-ID's superconducting wiggler has 25 full-field magnetic poles, as well as 2 half-field magnetic poles, causing the electron beam to "wiggle" inside the device in a sinusoidal shape as the electrons pass through it. The periodicity of the electron beam is 4.8 cm, with a magnetic deflection parameter K of 19.3. The BMIT-ID superconducting wiggler supplies a critical photon energy of 24 keV, at a maximum magnetic field of 4.3 T (86). The polychromatic X-rays generated by the superconducting wiggler travel down the beamline and into a specialized primary optics enclosure (POE-3) hutch, where the incident polychromatic X-ray photons are refined (1). Specific X-ray beam energies are selected from the polychromatic source using a monochromator, which is a series of two perfect silicon crystals refracting the incident X-ray beam at specific angles. The monochromator utilizes Bragg's law of crystal refraction to select a specific wavelength (in reality a bandwidth $\frac{\Delta\lambda}{\lambda}$) of photons passing through it (87). In this way a monochromator can be tuned to allow only a specific wavelength through. After the monochromator has selected a specific bandwidth, the monochromatic X-rays can be filtered using different thickness of specific metals, e.g. copper. The refined X-rays then enter the imaging hutch, pass through the sample, and are collected with an X-ray detector. The size of the beam at the sample location in the imaging hutch is approximately 200 mm x 11 mm. The imaging stage rotates in a single plane parallel to the ceiling and floor of the imaging hutch. The imaging axis is therefore perpendicular to this plane, and parallel to the walls of the hutch as shown in Figure 3.8.

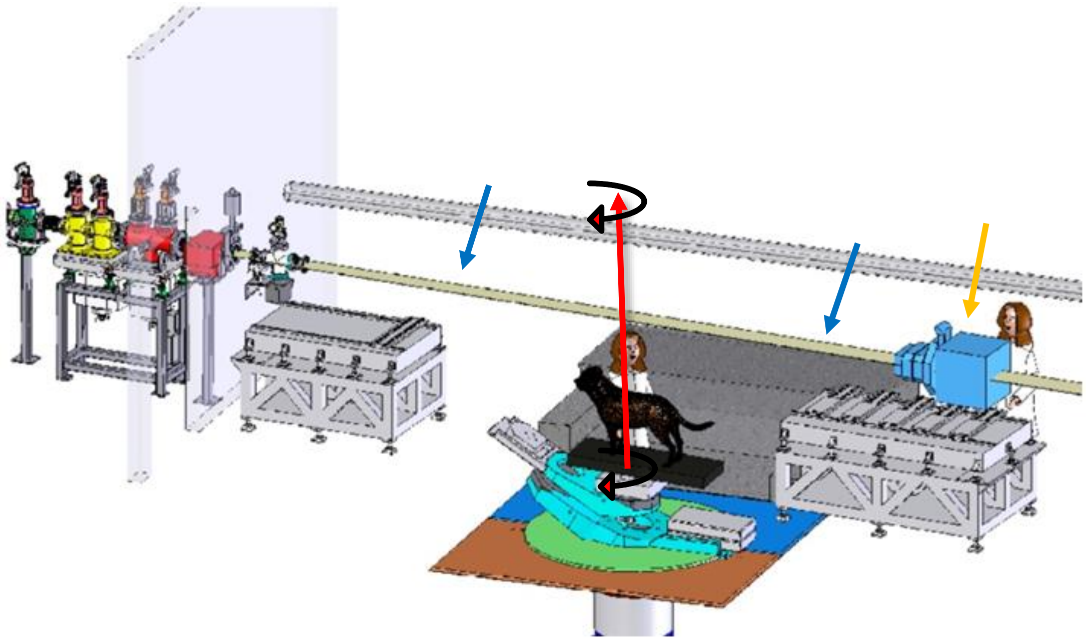

Figure 3.8: The experimental setup of the BMIT imaging hutch. The X-ray beam is indicated with a blue arrow. The imaging axis is indicated with a red arrow, notice how it is perpendicular to the imaging beam path. The detector is indicated with a green arrow. Modified from (1). Reprinted with permission.

3.3 *Phase Contrast – Computed Tomography*

Phase contrast imaging (PCI) is an imaging technique that allows for the phase information of X-rays passing through a sample to be collected. Especially useful for soft tissue imaging, PCI is more sensitive to density variations compared to absorption X-ray imaging (88). PCI's improved soft tissue contrast results from the phase cross section of low Z materials being 1000x that of the absorption cross section, indicating PCI is more sensitive than absorption X-ray imaging (11). The cross section refers to the probability of an absorption or scattering process occurring in an area due to elastic scattering, inelastic scattering, and photoelectric absorption (89). Elastic scattering refers to the conservation of kinetic energy of the photon after a modification to the direction of propagation, in contrast to inelastic scattering where kinetic energy of the photon is not-conserved. Photoelectric absorption refers to the attenuation or absorption of X-rays as the pass through an object. Phase contrast CT (PC-CT) has been developed for improved tomographic reconstructions from samples with low atomic Z, (e.g.), soft tissue. PC-CT uses the phase shift as the imaging signal, unlike conventional CT, relying only on absorption of X-rays (11). When X-rays penetrate matter, the index of refraction n of the material causes the electromagnetic wave to be absorbed and phase shifted, compared to an electromagnetic wave propagating in free space as seen in Figure 3.9. The index of refraction *n* of a material is shown in the following equation (90):

$$n = 1 - \delta + i\beta \qquad [3.7]$$

The refractive index is a complex number, with δ describing the real phase shift of the wave, and *i*β describing the imaginary change in amplitude as the wave is attenuated. δ and β are described in the following equations, respectively (90):

$$\delta = (\lambda/2/\pi)\rho_A\sigma_p \qquad [3.8]$$

$$\beta = (\lambda/4/\pi)\rho_A\sigma_a \qquad [3.9]$$

Where λ is the wavelength of the light, ρ_a is the atomic density of the sample, σ_p is the phase cross-section, and σ_a is the absorption cross-section. As stated previously, σ_p is three orders of magnitude greater than σ_a for low Z materials. The real part of the refractive index δ describes the change in the wave inside the material with *n* refractive index, in respect to a wave propagating outside the material in free space. The phase shift of the wave results in a change in the propagation direction as well. The phase shift, direction change, and amplitude attenuation of a wave propagating through a material is shown below in Figure 3.9.

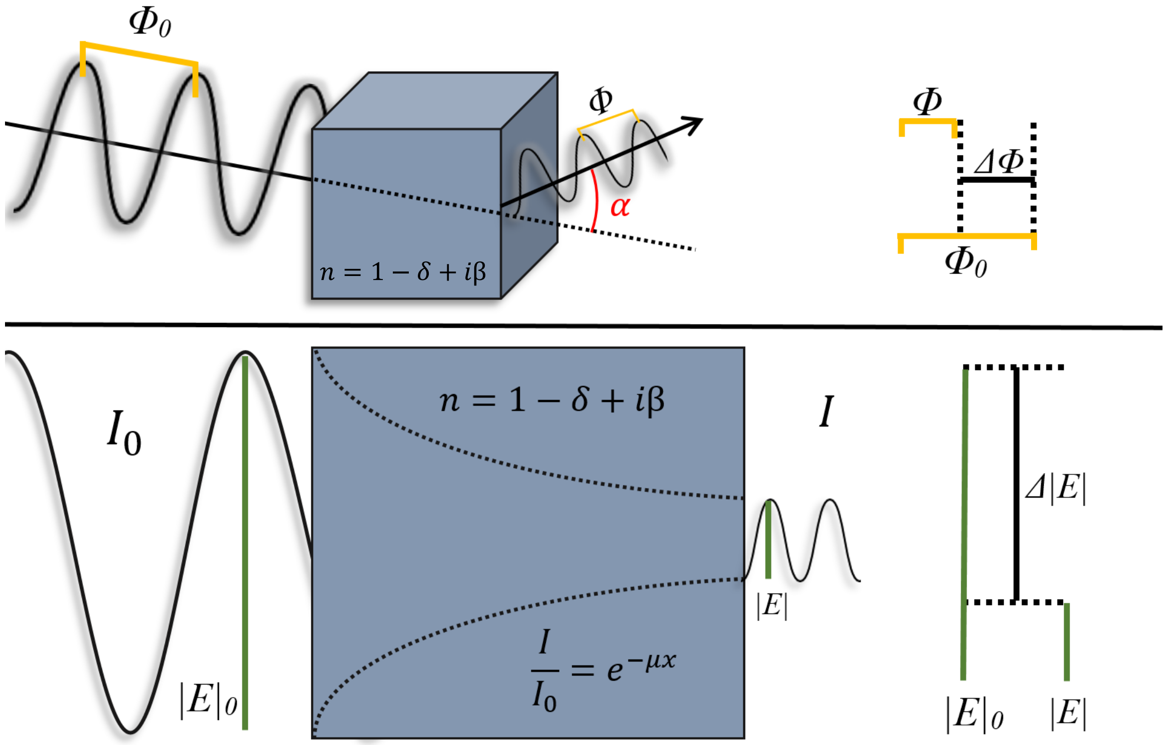

Figure 3.9: The phase shift and attenuation of a wave travelling through a material of *n* refractive index are shown. Top: The shift in phase (*ΔΦ)* is shown in orange and the change in propagation direction (*α)* is shown in red. Bottom: the attenuation of the amplitude (*Δ*|*E*|) between *I* to I_0, shown in green. Based from (2).

There are several PCI methods currently in use, including analyzer based imaging, propagation based imaging (PBI), crystal interferometry, and grating based imaging. Each of these methods can also be applied to CT, with their own strengths and weaknesses. PBI phase contrast computed tomography (PC-CT) was used to collect the data for this thesis (90).

Propagation based imaging PC-CT consists of a spatially coherent X-ray source, a sample some distance away, and a detector some distance away from the sample. Therefore, a small size X-ray source or a source far from the subject is needed to achieve the special coherency required for PBI. Synchrotron X-rays have been used numerous times for PBI imaging (9), (14), (82), (11), (91). The name of PBI derives from the experimental setup, as the detector is placed not immediately behind the sample like in conventional CT, but at some distance, allowing the refracted X-ray beam to propagate in free space before being detected as shown in Figure 3.10. The simple setup and minimal stability requirements are an advantage over other phase imaging modalities that require additional precise optical equipment.

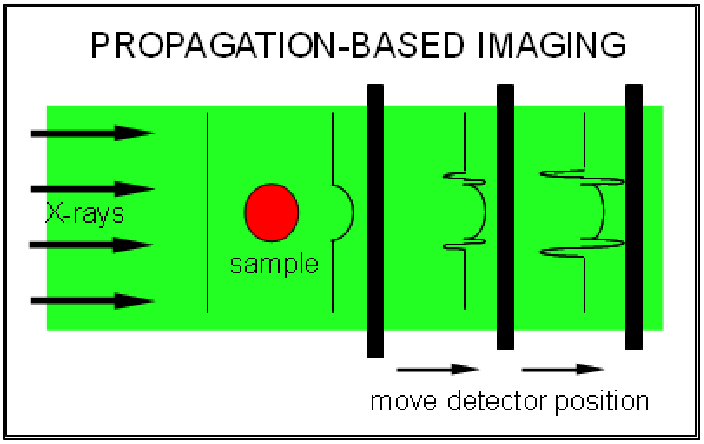

Figure 3.10: The scanning setup for PBI PC-CT imaging, showing Fresnel fringes forming as the wavefront propagates towards the detector. The further the detector position, the more the fringes form (92).

Fresnel fringes are created by the coherent X-ray beam as it propagates away from the sample towards the detector. The interference fringes created are proportional to the second derivative of the phase wavefront. The fringes are seen as edge enhancement, where the interfaces between two materials of different density are more clearly observed (93). This could improve contrast between objects of different density within the same sample being imaged.

PBI PC-CT was selected as the imaging modality for use in this research due to its relatively easy setup, relaxed constraints on stability, and improved soft tissue contrast for prostate visualization. All data collected on the BMIT-ID were collected using PBI PC-CT, which is often just referred to as PC-CT for simplicity.

Chapter 4: Materials and Methodology

This chapter outlines the design process of the canine positioning device, and the design specifications of the device. There were two re-designs of the canine positioning device, described chronologically in the following sections. Three experiments were conducted on the material used to create the canine positioning device, each with the specific goal of generating the best possible PC-CT reconstruction of *in situ* canine prostates. These include the pre-design experiment on the dog holder (the Pawsitioner), a mathematical predication of beam attenuation on the first design, and a comparison between two potential support structures for the final design. A summary of the X-ray detectors used to collect data on the BMIT-ID beamline concludes this chapter.

4.1 *Positioning Device Design Overview*

This section covers the discussion of the positioning device and the specifications needed for the BMIT-ID beamline, and concludes with a discussion of the pros and cons of the different detectors available at the CLS for imaging on the BMIT-ID beamline.

The specific objective of this research was to design, develop, and implement a canine positioning system for the BMIT-ID beamline, capable of imaging *in situ* dog prostates in both cadaver and live dogs. The canine positioning device was designed to restrain dogs in a vertical dorsal recumbency position to minimize the amount of tissue the beam would have to traverse to effectively image the prostate. The pre-design thought was to have the dog in this near vertical dorsal recumbent position, allowing for the scan’s axis of rotation to be centered on the canine prostate area, while reducing the amount of tissue attenuation length the beam would need to pass through. There are three potential axes of rotation allowed in 3D space, and the dog is required to spin on one of these axes during a PC-CT scan. The transverse plane of the dog in the abdominal and pelvic regions has the smallest tissue cross section area compared to the dorsal plane or the median plane, as seen in Figure 4.1. The transverse plane of the dog is represented with the dimensions X and Y. The median and dorsal planes through the abdominal and pelvic areas present a larger cross section though the dog, thereby maximizing the attenuation length of the x-ray beam through this tissue. Therefore, the dog should be held within the device in such a way as to allow a transverse section of the abdomen and pelvis through the imaging beam to minimize beam attenuation. The scan axis of the dog needed to align with the rotational axis of the imaging stage in the BMIT-ID hutch, on which the device would be fitted and rotated, as seen previously in Figure 3.8. Therefore, the final position of the dog during scanning was decided on, as the cranial-caudal anatomical line needed to align with the rotational axis of the stage, parallel to the walls of the imaging hutch. Through this chapter, the development of the canine positioning system is described.

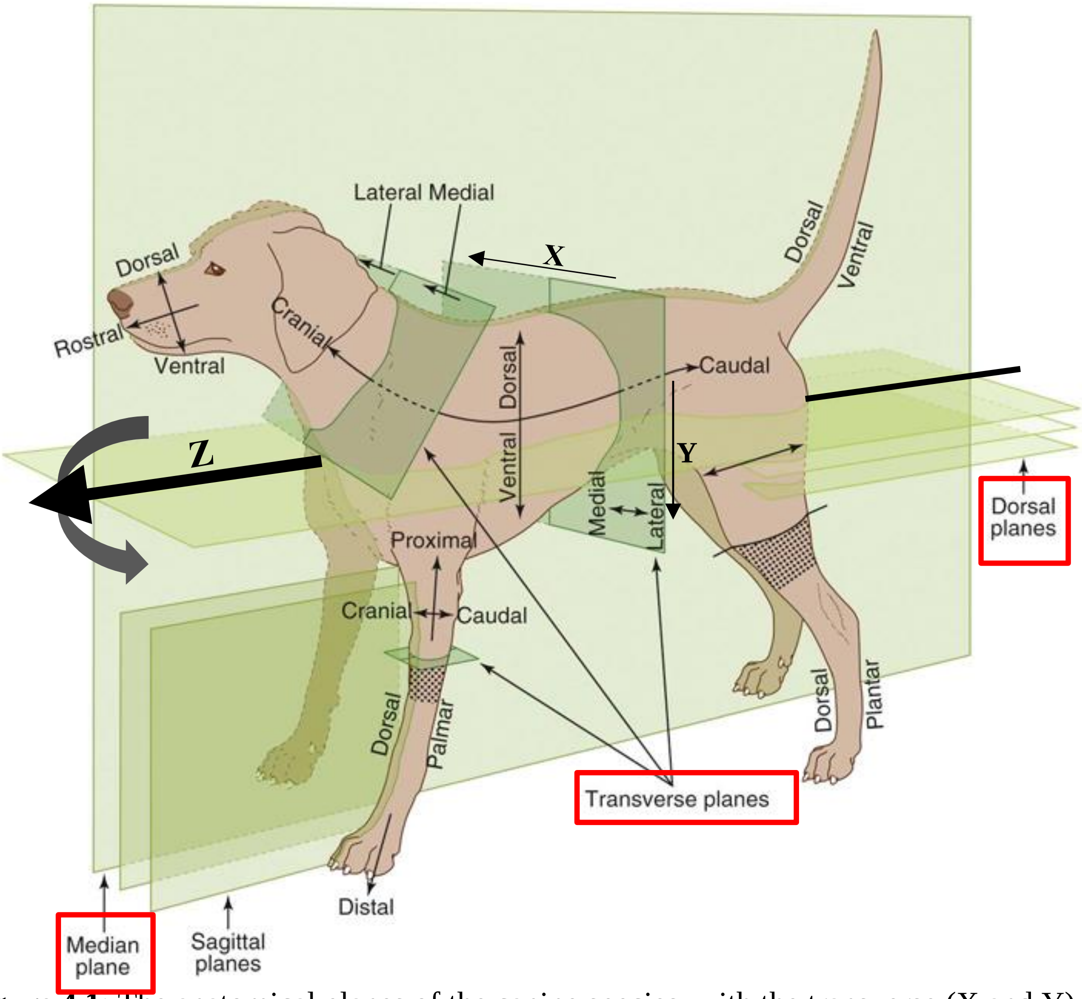

Figure 4.1: The anatomical planes of the canine species, with the transverse (X and Y), median and dorsal planes shown, squared in red. The rotational axis of the dog within the canine positioning device is represented with the black arrow traversing from caudal to cranial. The location that the transverse plane traverses the dog is described as height, and is represented by Z. The transverse plane of the abdomen and pelvis has the smallest cross section, compared to both the median and dorsal planes (94). Reprinted with permission.

4.1.1 *Design Specifications*

The design of the device began with preliminary meetings between researchers from the University of Saskatchewan Prostate Cancer Research Team (USPT), including myself, Beamline Scientists from the CLS BMIT beamline and engineers from RMD Engineering Inc., who constructed the device. The device was specified to do the following:

1) Provide structural stability to the dog while it was rotated during a PC-CT scan.
2) Have minimal material and canine tissue in the path of the beam to reduce attenuation.
3) Have material that was in the path of the beam be of a low atomic number with a low mass attenuation (μ/ρ) value.

4) Not exceed the maximum weight capability of the Canadian Light Source micro-beam radiation therapy (MRT) lift (130 kg: includes weight of device plus dog).
5) Be compatible with and be able to support housing of the anesthetic equipment needed for live dog imaging.

4.1.2 *Pawsitioner*

The Pawsitioner is a commercially available product from AVAIL Concepts, IIC, Sedona, AZ (95). The Pawsitioner was designed for positioning anesthetized dogs for a number of applications, including ultrasonography, CT, MRI, dentistry, surgery, and myelography. The Pawsitioner is made of polyethylene, making it radio-transparent. The Pawsitioner is available in three sizes (24, 37 and 58 inches long) and is designed primarily to hold dogs of various sizes (small <15 kg, medium 15-30 kg and large dogs > 30 kg) during CT scans. A front and side view of a Pawsitioner can be seen in Figure 4.2.

Figure 4.2: Front and side view of the Pawsitioner (95).

A preliminary experiment was conducted on the BMIT-BM beamline to determine if the Pawsitioner would negatively affect reconstruction quality by being in the field of view during PC-CT scanning. It was hypothesized that the low mass attenuation and small cross section area of the Pawsitioner would not affect PC-CT reconstruction quality. If the Pawsitioner created reconstruction artifacts compared to previous tests conducted on the BMIT-BM beamline with excised prostates, then another canine holder would need to be found or designed before moving forward with designs for a complete positioning device. If the image reconstruction quality was not affected, the designing of the positioning device could proceed using the Pawsitioner as the primary canine holding device.

A sample of an excised formalin-fixed canine prostate was set in a polyethylene container, with a diameter of 4.5cm, and filled with clear gelatin (Knox, Oak Brook, IL). The gelatin was allowed to solidify overnight in a fridge. The container with the prostate/gelatin was then wrapped with store-bought beef steak to simulate the surrounding soft tissue around the prostate in a live dog for imaging purposes. The steak and container diameter was 8 cm. The steak/gelatin/prostate sample was then placed in the BMIT-BM hutch on the CT stage. The Pawsitioner was attached to the imaging stage and partially surrounded the prostate sample. A picture of the setup can be seen in Figure 4.3. The experiment would be considered successful if the reconstruction quality of the scan of the excised prostate was not affected compared to previous results generated on the BMIT-BM beamline that did not include the Pawsitioner device.

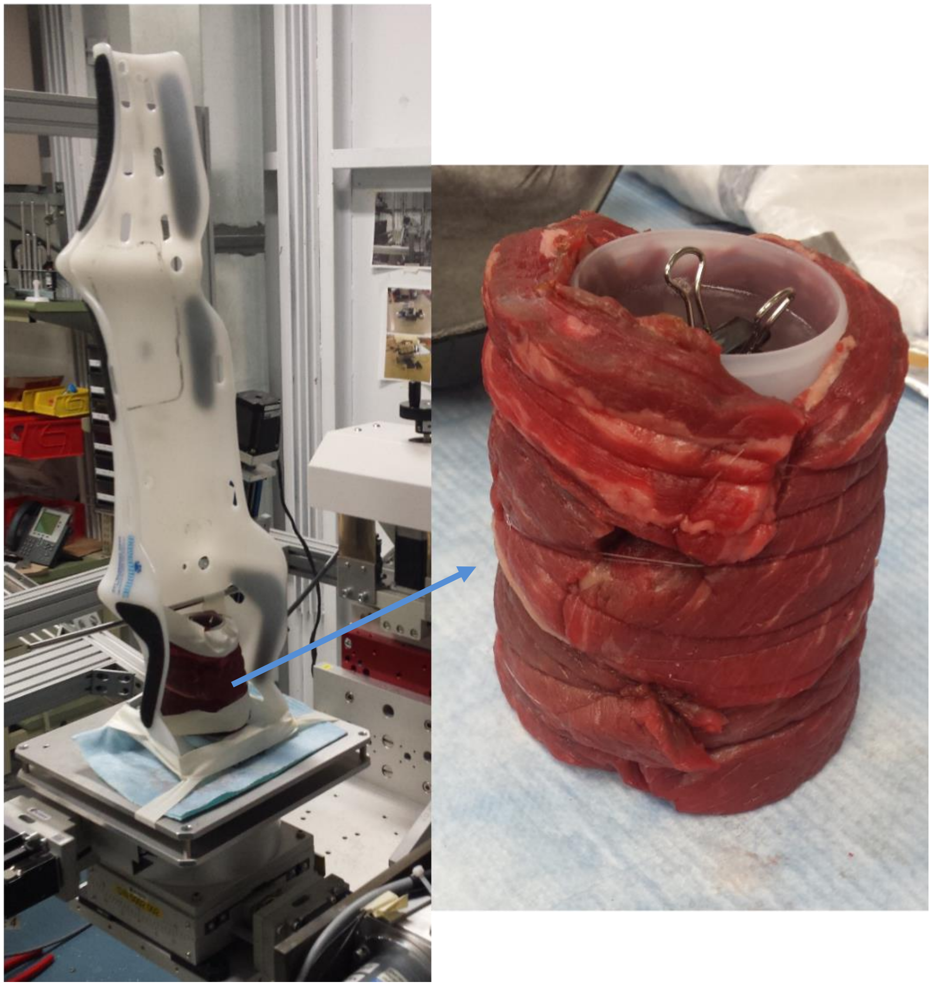

Figure 4.3: The experimental setup for the Pawsitioner test. Left is the overall setup on the CT stage. The blue dashed arrow indicates a close up of the excised canine prostate, set in gelatin and surrounded by steak, right.

The sample was PC-CT scanned at 40 keV, with a 225 ms exposure time for each tomographic projection, and 3751 tomographic projections captured over 180° CT rotation. The resolution at the detector was 14 microns/pixel, with a total capture area of 3894 pixels x 235 pixels. The source to sample distance on the BMIT-BM beamline is 20.15 m, and the sample to detector distance was 5.84 m. The reconstruction results are shown in Figure 4.4. The data collected was reconstructed using NRecon, a software program designed by Bruker microCT (96).

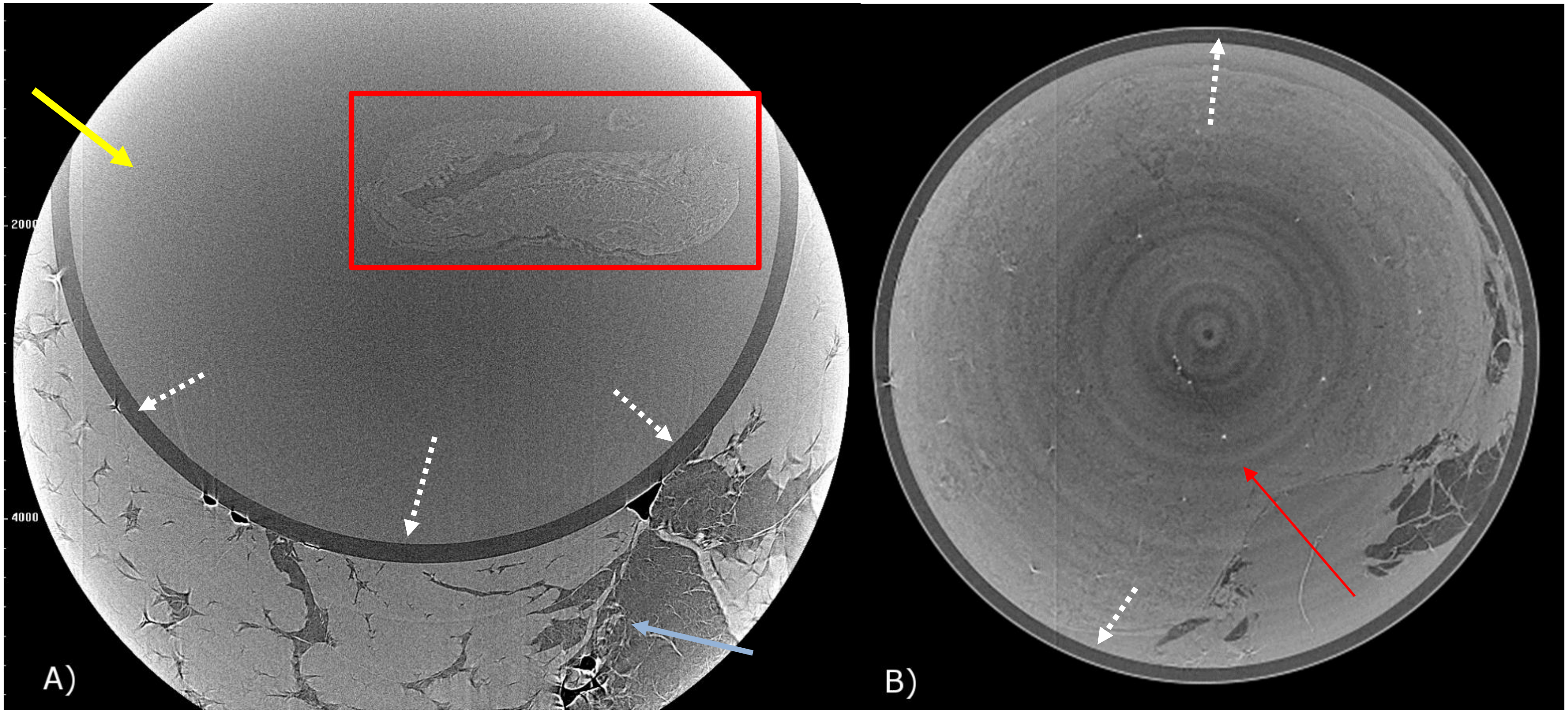

Figure 4.4: A). A slice reconstruction of the PC-CT scan experiment test done with the Pawsitioner, excised canine prostate and steak. The reconstruction was performed in NRecon (96). A red box surrounds the thin slice of prostate tissue, and a blue arrow indicates steak. The polyethylene container is indicated with a dashed white arrow, and the Knox gelatin is indicated with a yellow arrow. The area within the red box is shown larger in Figure 4.5. B). A sample PC-CT reconstruction from an *ex vivo* canine prostate imaged on the BMIT – BM beamline. The white dashed arrows indicate the container, and the red arrow indicates the prostate.

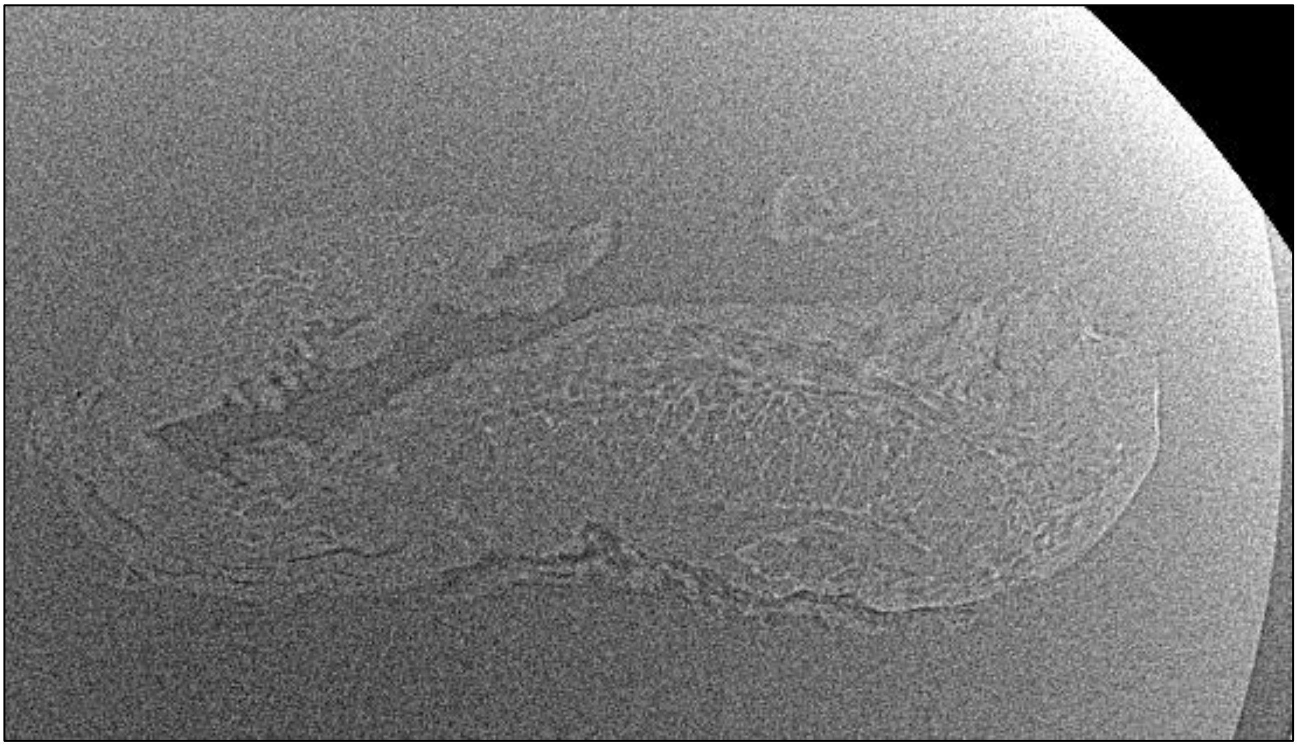

Figure 4.5: A zoomed slice reconstruction of the PC-CT scan experiment test done with the Pawsitioner, excised canine prostate and steak. The prostatic tissue can be seen here, surrounded by Knox gelatin. Distinct tissue arrangements are apparent. This is the area within the red box seen in Figure 4.4.

Previous experiments done on the BMIT-BM beamline with excised prostates set in gelatin produced similar results as to the test done with the Pawsitioner in the field of view, as seen in Figure 4.4. The reconstruction quality was not affected when compared to images from similar previous experiments conducted on the BMIT-BM beamline, supporting the original hypothesis that the low mass attenuation and small cross section area of the Pawsitioner would not affect PC-CT reconstruction quality. The Pawsitioner was therefore determined to be acceptable for restraining/supporting the dog in combination with the positioning device while imaging on the BMIT-ID beamline. Further requirements for the canine positioning device to be designed included:

1) Provide structural stability to the dog while it was rotated during a PC-CT scan.
2) Have minimal material and canine tissue in the path of the beam to reduce attenuation.
3) Have material that was in the path of the beam be of a low atomic number with a low mass attenuation (μ/ρ) value.
4) Not exceed the maximum weight capability of the micro-beam radiation therapy (MRT) lift (130 kg: includes weight of device plus dog).
5) Be compatible with and be able to support housing of the anesthetic equipment needed for live dog imaging.

4.2 *Preliminary Positioning Device Design*

An initial design was drafted, as shown in Figure 4.6. The design had a three-tiered base for gross adjustment of translational movement in the x-y direction with the base attaching to the top of the BMIT ID Beamline MRT lift. The base of the support structure has specially designed spaces for anesthetic equipment, including the oxygen tank, anesthetic gas vaporizer and scavenger, and isoflurane holder. The top of the Pawsitioner needs to be able to be attached to the support beam; this was accomplished using four screws. The base of the Pawsitioner was not attached to the base of the support in the initial design. With this design X-rays would enter parallel to the floor, and pass through the Pawsitioner and polycarbonate support and support as shown in the Figure 4.6. The polycarbonate support is shown in more detail in Figure 4.7 and Figure 4.8.

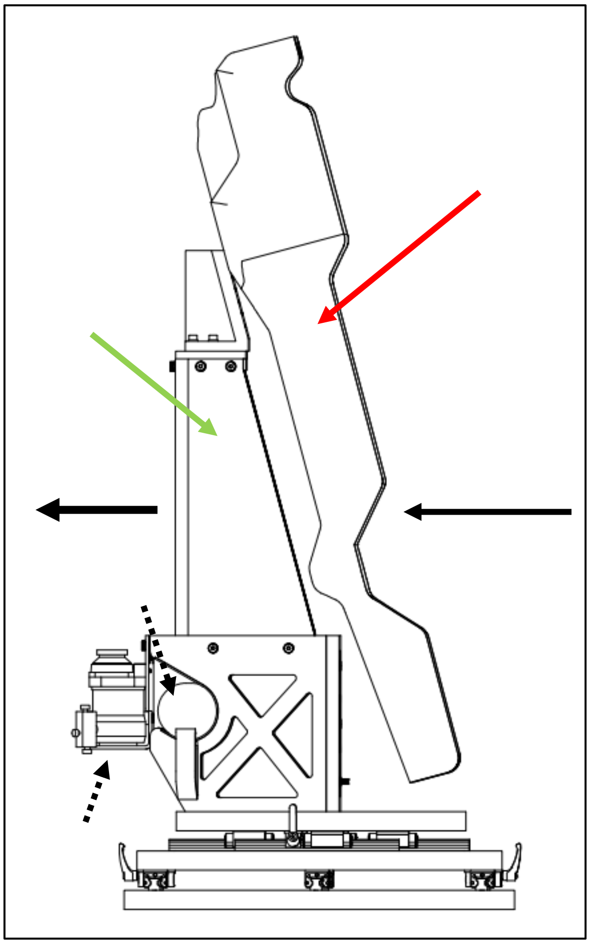

Figure 4.6: A side view of the preliminary design of the canine positioning device, with the Pawsitioner indicated with a red arrow. The green arrow indicates the polycarbonate support structure. The anesthetic equipment attachments are indicated with black dashed arrows. The X-ray beam path is indicated with black arrows.

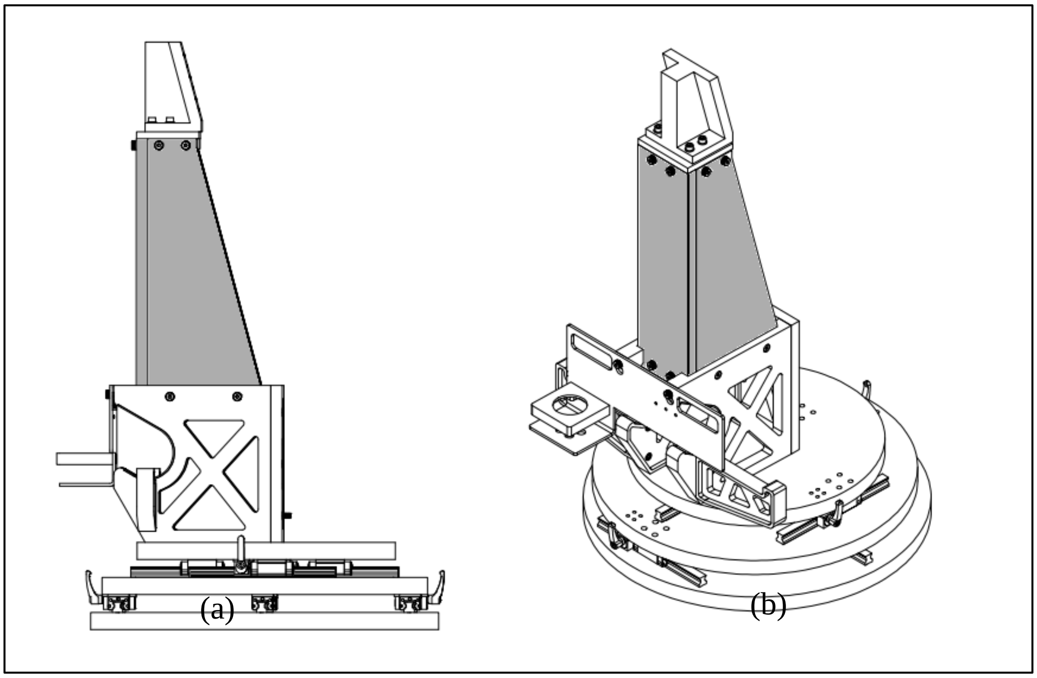

Figure 4.7: (a) A side view of the polycarbonate preliminary canine positioning system support structure shaded in grey and (b) A 3D view. The Pawsitioner is not seen in above figures.

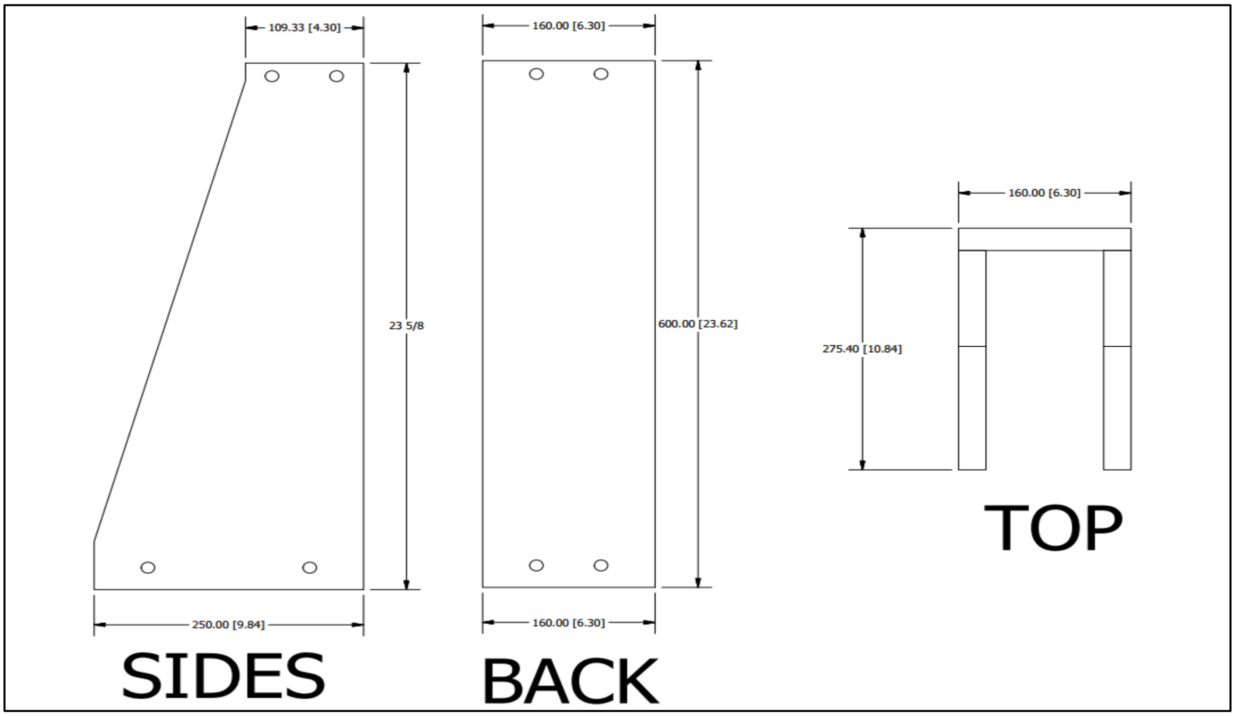

Figure 4.8: The back, sides, and top blueprint for the polycarbonate preliminary support structure are shown. Initial units are in mm, inches shown in brackets.

It was hypothesized that the reconstruction quality of the canine prostates held in the device may be negatively affected by the large beam attenuation length of the support structure. To test this hypothesis, this preliminary polycarbonate support structure was analyzed for beam attenuation, with results of the calculations shown in Table 4.1. As outlined in section 3.1.1, the attenuation (I/I_0) of an object can be calculated using the mass attenuation coefficient (μ/ρ) and the density (ρ) of the sample, along with the attenuation length (x) of the beam.

$$\frac{I}{I_0} = e^{-\left({}^{\mu}/_{\rho}\right)\,\rho\,x} \qquad [3.1]$$

Three paths through the polycarbonate supports were analyzed for beam attenuation, the minimum path travelled, the maximum path travelled, and realistic path travelled by the beam. The realistic path indicated where the prostate was likely to be located in the cadaver. The three beam paths are shown in Figure 4.9, (A) indicates the shortest, (B) the expected, and (C) the maximum attenuation length of the polycarbonate support. Three beam energies of 50 keV, 60 keV, and 80 keV were selected for the attenuation analysis for each beam path. The energies selected were based on the specifications for the energy spectrum produced by the BMIT-ID wiggler, and the lower absorption of X-rays at higher photon energy. The three beam paths are parallel to the floor and perpendicular to the back plate. Polycarbonate has a μ/ρ of 0.024/cm, 0.2244/cm, and 0.2052/cm at 50 keV, 60 keV, and 80 keV, respectively (97), and a density of 1.2 g/cm^2.

Beam path through support	Beam length though support (cm)	Attenuation at 50 keV (I/I_o)	Attenuation at 60 keV (I/I_o)	Attenuation at 80 keV (I/I_o)
A	2.54	0.471	0.566	0.594
B	17.5	5.83×10^{-3}	1.97×10^{-2}	2.76×10^{-2}
C	27.5	3.08×10^{-4}	2.09×10^{-3}	3.54×10^{-3}

Table 4.1: Attenuation data for the beam paths of different lengths shown in Figure 4.9. Attenuation is calculated for 50, 60, and 80 keV beam energies. The smaller attenuation values indicate the greater attenuation of the beam.

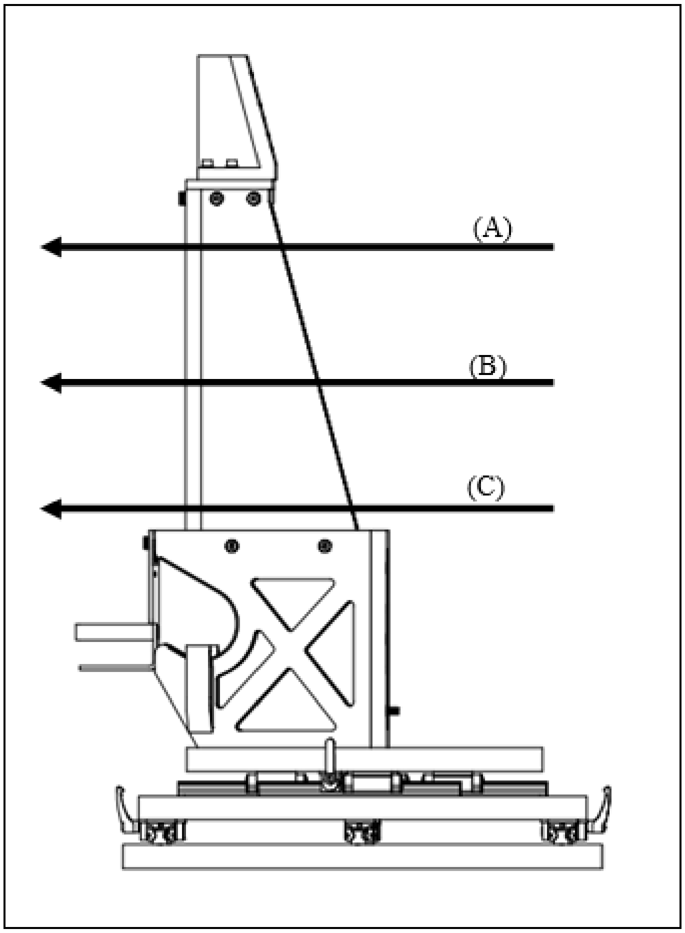

Figure 4.9: Three potential beam paths are shown bisecting the polycarbonate support. The beam attenuation lengths of A, B, and C are 2.54 cm, 17.5 cm, and 27.5 cm, respectively.

It was determined that the polycarbonate support structure should not attenuate the beam by more than 10% of its original value, or reconstruction quality would decrease significantly (98). Therefore, the I/I_o value must be greater than 0.90 for the beam path to produce reasonable reconstructions, i.e anything less than 0.90 I/I_0 is undesirable. The smallest beam path through the polycarbonate support (Path A, 2.54 cm) reduced the beam intensity by 40.6% at the highest beam energy. The beam length traversing the support (Path B, 17.5 cm) at the expected prostate height attenuated the beam by 97.3% at 80 keV. At a length of 27.5 cm, the longest potential beam path through the polycarbonate support, the beam was attenuated by 99.6%. The preliminary polycarbonate support design was therefore predicted to cause severe X-ray beam attenuation at certain angles in the beam, proving the hypothesis even at a minimum distance and high photon energy, and rejected.

It was decided that the polycarbonate support structure should be redesigned to eliminate the material from the path of the beam while still providing stability for the dog to be imaged.

4.3 *Secondary Positioning Device Design*

A second design of the canine positioning device was completed in February 2015. The design is shown in Figure 4.10, with the vertical support structure from the previous design completely removed. The Pawsitioner is now attached to the support at its base. The three-tiered base remained unchanged.

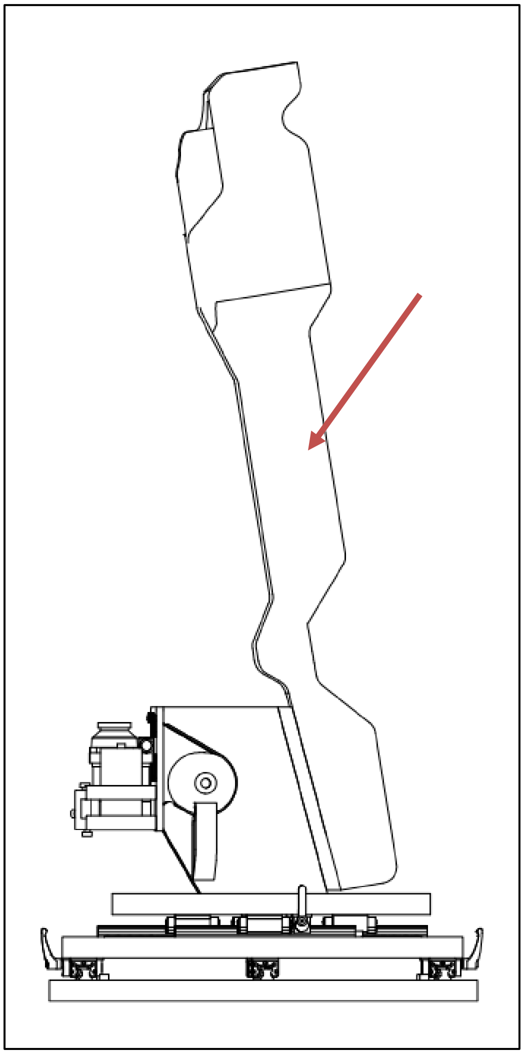

Figure 4.10: A side view of the secondary design of the canine positioning device, with the Pawsitioner indicated with a red arrow.

Upon further discussion, the design in Figure 4.10 was rejected as the lack of support structure at the top of the Pawsitioner could allow for lateral movement and vibration during the imaging, which would be detrimental to the reconstruction quality (98). With only one attachment point at the base, it was a concern that the device would not allow for the stability needed to successfully perform PC-CT with a dog

4.4 *Positioning Device Support Testing*

A compromise between structural stability and minimal attenuation length was needed for the canine positioning device. A second test was conducted on the BMIT-BM beamline to determine the optimal shape for a support structure to immobilize the top end of the Pawsitioner. Two potential shapes for the support structure were selected: a hollow polycarbonate tube with outer diameter 10 cm and a wall thickness of 0.7 cm; and a solid polycarbonate cylinder of 3.81 cm diameter, as seen in Figure 4.11. The hypothesis for this testing was that since the hollow tube had the smallest beam attenuation length it would have fewer negative effects on PC-CT image reconstruction than the solid polycarbonate cylinder. The two shapes were chosen based on the uniformity of a circular support structure, and a high support to attenuation ratio, i.e. the tube and the cylinder can support a large amount of weight with a small attenuation length of the beam.

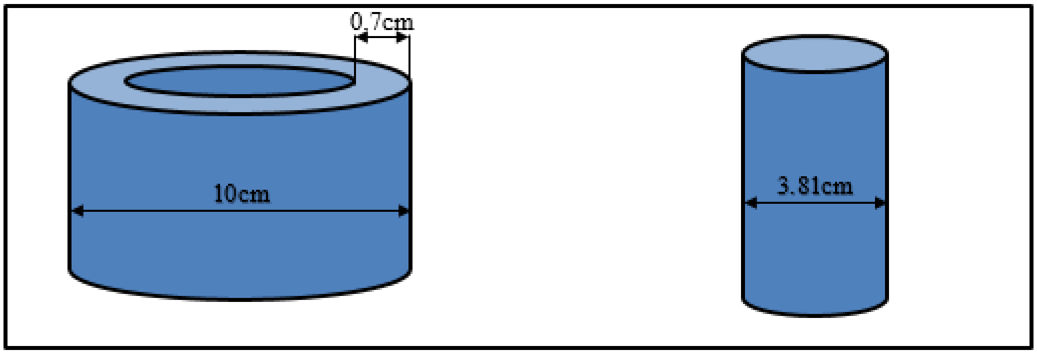

Figure 4.11: Left: The polycarbonate tube with an outer diameter of 10cm and a wall thickness of 0.7cm, the center is hollow. Right: The polycarbonate cylinder with a thickness of 3.81cm.

Polycarbonate was chosen as the material due to its relatively low mass attenuation coefficient and availability. A sample of formalin-fixed excised canine prostate was prepared and set in gelatin. The gelatin/prostate sample was again wrapped with store bought beef steak to better simulate canine tissue as described previously, with an overall 7 cm total diameter resulting. For concision the prostate/gelatin/steak sample is referred to as just the "pseudo-prostate" sample though the rest of this section. The pseudo-prostate sample was placed within the small Pawsitioner and then attached to the CT stage in the BMIT-BM hutch. For two of the scans a canine pelvic bone was attached to the periphery of the pseudo-prostate sample. The canine pelvic bone was supplied from the Western College of Veterinary Medicine Anatomy department. A preliminary scan was done for a baseline reconstruction without the pelvic bone or either of the polycarbonate support structures. The initial scan was done at 35keV; with a capture time of 255 ms. Five scans were taken in total; the experimental setup summary of each scan is shown in Table 4.2. A total of 3751 projections were taken during a 180° rotation for all scans. The general setup for the tests are shown in Figure 4.12.

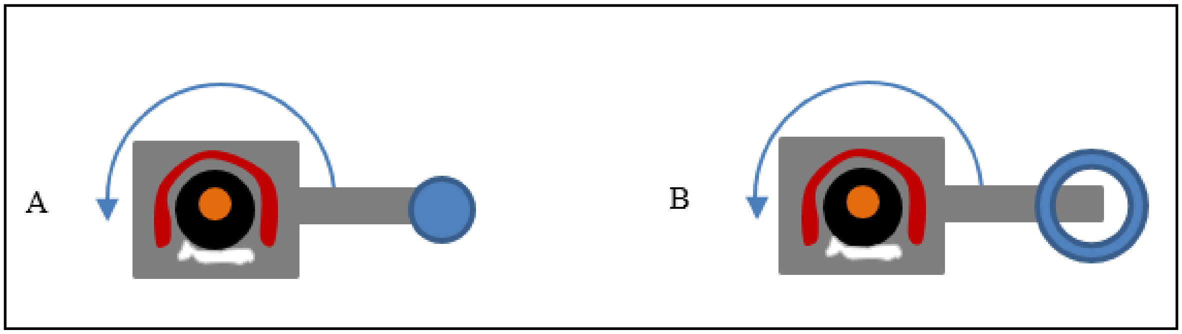

Figure 4.12: A top (birds eye) view of the experimental setup for the polycarbonate support test conducted on the BMIT-BM beamline. A) The blue solid circle indicates the solid polycarbonate tube. The red, black and orange areas represent the Pawsitioner, the steak, and the pseudo-prostate, respectively. The blue arrow indicates the direction of rotation during a single scan. The pelvic bone is the white shape with the orange outline, and was only used in the final two scans. B) The blue hollow circle indicates the hollow polycarbonate cylinder; all other objects remain the same as in A.

Scans	Experimental Setup	Capture Time (ms)	Attenuation Length of Polycarbonate Support (cm)
Scan 1	Prostate Sample	255	n/a
Scan 2	Prostate Sample + Polycarbonate Cylinder	350	3.81
Scan 3	Prostate Sample + Polycarbonate Tube	400	1.40
Scan 4	Prostate Sample + Pelvic Bone	425	n/a
Scan 5	Prostate Sample + Polycarbonate Cylinder + Pelvic Bone	250	3.81

Table 4.2: A summary of the experimental setup for each scan performed on the BMIT-BM beamline. The capture time was adjusted during each scan to overcome the exponential drop in storage ring current at the CLS. Scans 1 and 4 did not have the polycarbonate support structure during the scans and therefore do not have an attenuation length of polycarbonate support.

Scans 1, 2, and 3 were used to determine the optimal shape for the polycarbonate support structure design. Scans 4 and 5 were auxiliary tests to determine if the pelvic bone would be detrimental to the ability to reconstruct the CT data. The polycarbonate supports in each of the scans was placed 18.5cm radially from the center of rotation on the CT stage. A radial distance of 18.5 cm was chosen as this was likely to be the actual distance of the support from the prostate in the final draft of the design. Data from all five scans were reconstructed using NRecon. A total of 173 slice reconstructions were generated from each scan, with a pixel size of 13.9 microns, and a resolution of 3987x3981 pixels.

A board certified veterinary radiologist compared the scan reconstruction qualities against one another. This was done to determine the best candidate for the support structure design. The veterinary radiologist was blinded to the experimental setup for each reconstructed image - three sample reconstructions from each scan were evaluated. A random number generator was used to select the slice height of the images to be evaluated - slices 87, 155, and 68 were called Tests 1, 2, and 3, respectively. The five scan slices of each height were given a score from 1-5, with 1 being the highest quality reconstruction and 5 being the poorest reconstruction quality with the most artifact present. Each scan reconstruction was performed with the same parameters selected for scan 1 in NRecon, to reduce any biases in the reconstruction process. The results of the three reconstruction quality assessments done by the veterinary radiologist are shown in Table 4.3. Figure 4.13 shows reconstructions from scan 3 and scan 1 from test 2; (a) and (b), respectively.

Reconstruction Quality (1 = High, 5 = Poor)	Test 1 (Slice Height 87)	Test 2 (Slice Height 155)	Test 3 (Slice Height 68)
1	Scan 3	Scan 3	Scan 3
2	Scan 2	Scan 1	Scan 2
3	Scan 4	Scan 4	Scan 1
4	Scan 5	Scan 2	Scan 5
5	Scan 1	Scan 5	Scan 4

Table 4.3: A summary of the results from the reconstruction quality assessment performed by the veterinary radiologist. The row denoted with 1 represents the reconstructions with the highest quality, 5 with the poorest reconstruction quality.

It was determined that scan 3 had the best reconstruction quality of all three quality assessment tests. As shown in Table 4.3, scan 3 contained the prostate sample and polycarbonate hollow tube and was determined to have the highest reconstruction quality in all three tests. Therefore, from these results, it was decided that there should be a support for the upper end of the Pawsitioner constructed out of hollow polycarbonate tubing, in agreement with the hypothesis that since the hollow tube had the smallest beam attenuation length it would have fewer negative effects on PC-CT image reconstruction than the solid polycarbonate cylinder

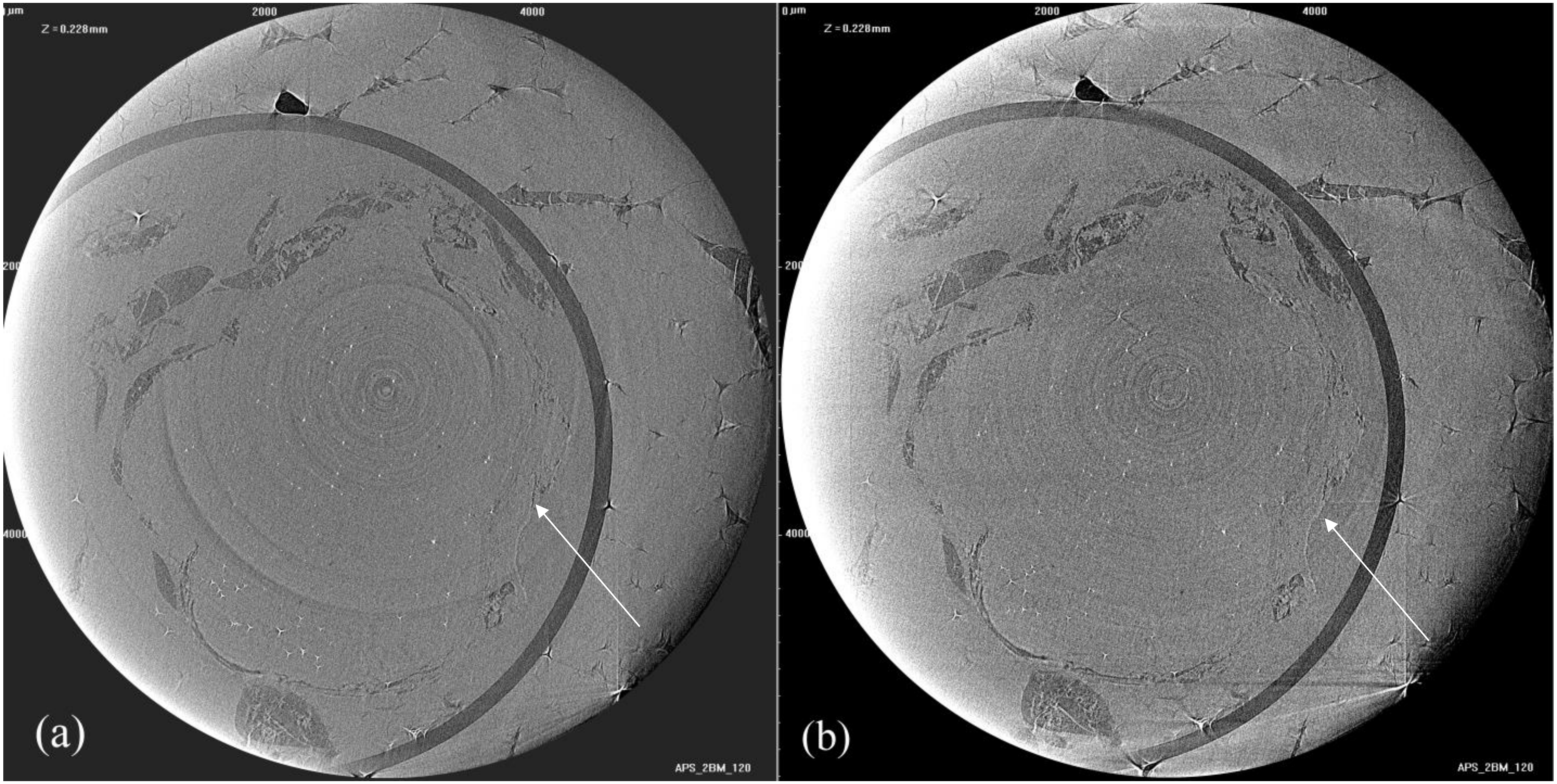

Figure 4.13: Examples of reconstructions assessed by the veterinary radiologist. These two slices are from the slice height of 155, test 2. (a) shows the reconstruction from scan 3, (b) shows the reconstruction from scan 1. Prostate tissue is indicated with white arrows in both (a) and (b).

4.5 *Final Canine Positioning Device Design*

The final product after manufacturing and assembly can be seen in Figure 4.14 (a). The final design is shown in Figure 4.14 (b). The final design met the requirements described in section 4.1.1:

1) Provide the required structural stability to the dog while it was rotated during a PC-CT scan.
2) Have minimal material and canine tissue in the path of the beam to reduce attenuation.
3) Have material that was in the path of the beam be of a low atomic number with a low mass attenuation (μ/ρ) value.
4) Not exceed the maximum weight capability of the micro-beam radiation therapy (MRT) lift (130 kg: includes weight of device plus dog).
5) Be compatible with and support anesthetic equipment needed for live dog imaging.

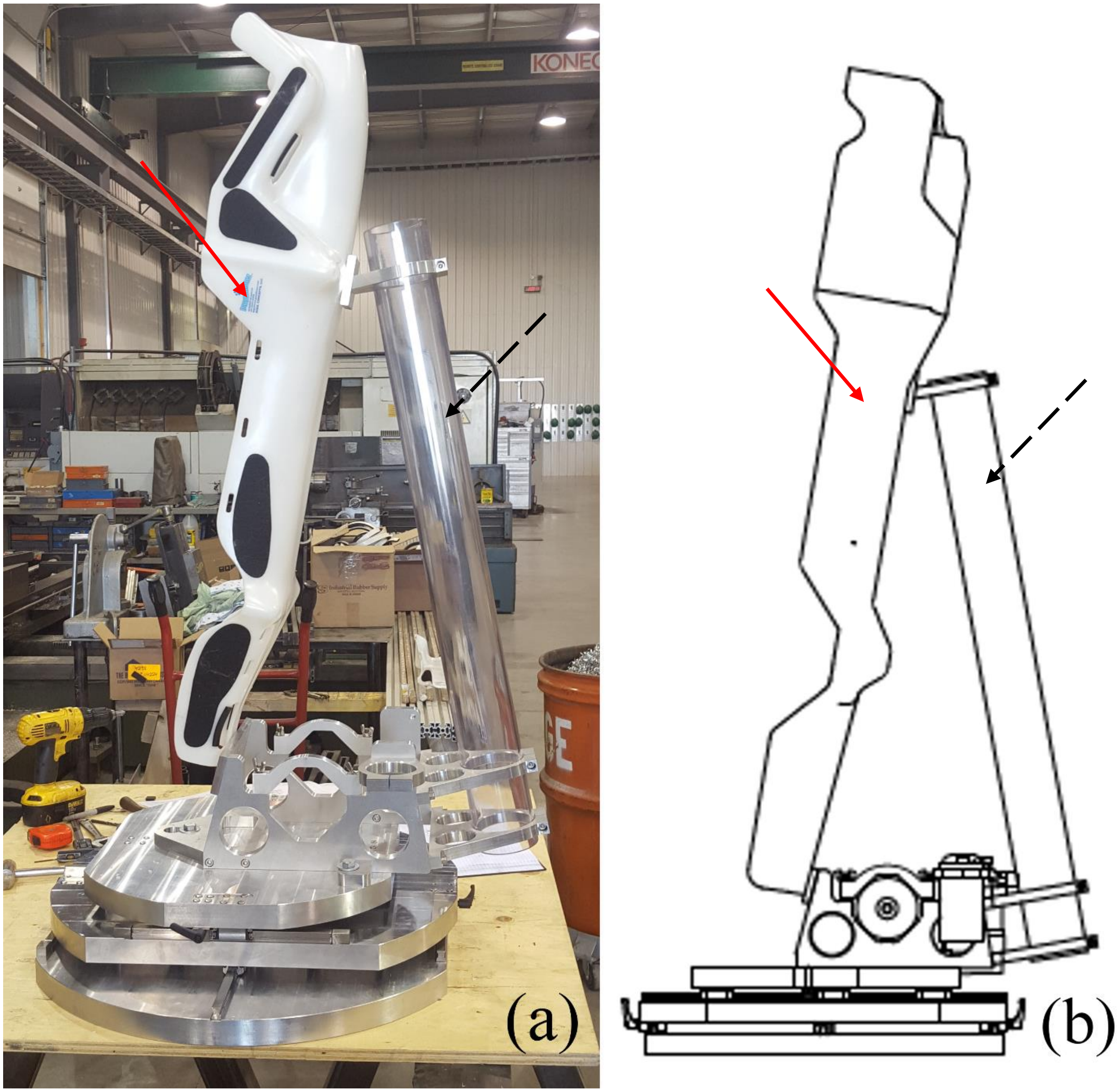

Figure 4.14: (a) A side view of the final design of the canine positioning device, with the Pawsitioner indicated with a red arrow. The polycarbonate support tube is indicated with a dashed black arrow. (b) A side view of the final draft design approved by the USPT, with the arrows indicating the same structures as in (a).

4.6 *X-ray Detectors*

The concluding section of Chapter 4 covers the X-ray imaging detectors used on the BMIT-ID beamline at the CLS. For this thesis three X-ray imaging detectors were used to collect data. The majority of the canine cadavers were imaged with a Photonic Science Fiber Optic Camera (XDI-VHR 90) (99). With funding from the Saskatchewan Health Research Foundation Phase Two grant, the USPR was able to purchase another X-ray detector, the Photonic Science Fiber Optic Camera (X-ray SCMOS) (100). A third detector, a Hamamatsu Flat Panel Sensor Detector (C9252DK-14) was used to collect data on the final canine cadaver images, as well as several of the live dogs imaged (100). The specifications of each of the detectors are shown below in Table 4.4.

Detector	Field of View (mm)	Effective Pixel Size (microns)	Energy Range (keV)	Frame Rate (FPS)
Photonic Science Fiber Optic Camera (XDI-VHR 90)	74 x 49	18.7	5 - 100	0.5-2
Photonic Science Fiber Optic Camera (X-ray SCMOS)	105 x 52	25.3	5 - 100	18-25
Hamamatsu Flat Panel Sensor Detector (C9252DK-14)	243 x 10	100	20 - 90	146

Table 4.4: Specifications for each of the three X-ray detectors used to collect data on the BMIT-ID beamline (100).

The important distinction between the cameras is their frame rate, where FPS stands for frames-per-second. The higher the frame rate, the more images can be captured in a shorter amount of time, which reduces the scan time. A short scan time is desirable due to motion artifact, which is discussed under 5.2. Any movement of the object being scanned negatively affects the quality of the reconstruction, creating motion artifacts as seen in Figure 4.15, and therefore quicker scan times allow for less movement to occur.

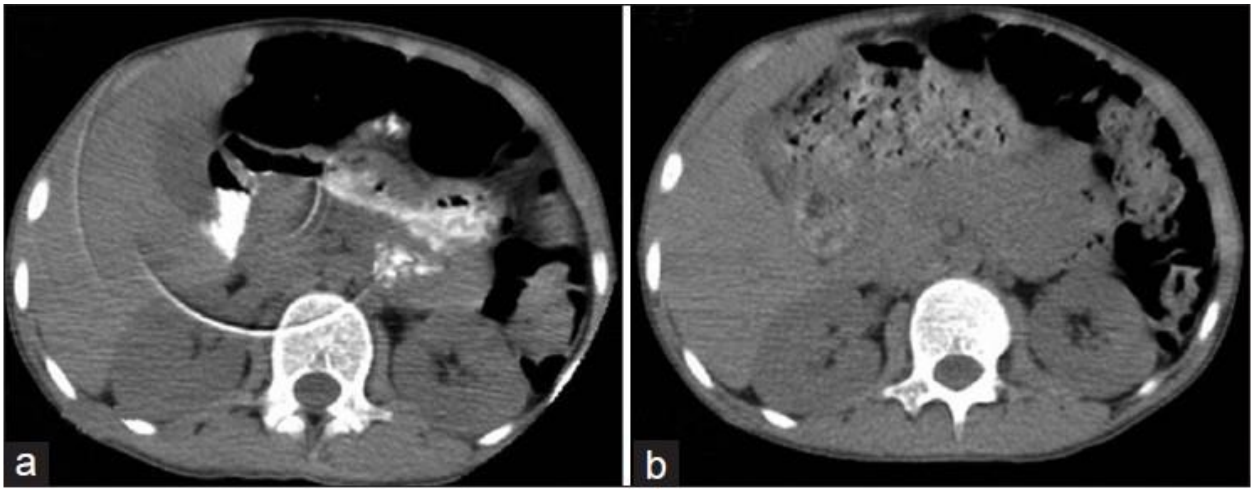

Figure 4.15: (a): Motion artifact of a transverse CT reconstruction of a human abdomen. (b) A transverse CT reconstruction of a human abdomen without motion artifact (101).

A typical PC-CT scan takes approximately 4000 tomographic projections over 180°. The number of projections captured by the detector during a PC-CT scan should be approximately the same as the number of columns in the detectors field of view. The total scan time for one view can be determined by dividing the total number of projections to be taken over the frame rate of the detector. Therefore, the Hamamatsu detector can capture one view of 4000 tomographic projections in approximately 27 seconds, making it the fastest detector available at the CLS BMIT compared to the XDI-VHR 90 and the X-ray SCMOS, which would take 2000 seconds (33.33 minutes) and 160 seconds (2.66 minutes) each to capture 4000 tomographic projections, respectively. The longer the scan time, the more the potential for the object being imaged to move, consequently the Hamamatsu Flat Panel would be the most desirable of the available detectors to prevent motion artifacts. However, the pixel size of the Hamamatsu detector is the largest of all three, giving it the poorest resolution. The pixel size of the detector directly effects the resolution in the reconstructions. As a general rule for CT, no object smaller than the pixel size can be discerned in the reconstructions (93). With this rule, the smallest object detectable by the Hamamatsu Flat Panel detector is 100 microns, while the XDI-VHR 90 and X-ray SCMOS can detect object of 19 and 25 microns, respectively. Therefore, the Hamamatsu Flat Panel may have the highest tolerance to movement, but is less desirable due to the large pixel size. For comparison, high resolution conventional CT has a maximum pixel resolution of 200 microns, and nuclear magnetic resonance imaging has a resolution of around 1000 microns (102), (103).

The differences of the field of view (FOV) is also important between the detectors. The Hamamatsu Flat Panel detector has the smallest FOV, with an area of 2430 mm^2, the XDI-VHR 90 Photonic Science detector has an intermediate FOV of 3626 mm^2, and the X-ray SCMOS Photonic Science has the largest FOV at 5460 mm^2. The width of the detector corresponds to the area of the reconstruction due to the algorithms used to reconstruct the CT data. The height of the detector corresponds to how many reconstructions can be generated from a data set. For example, the Photonic Science Fiber Optic Camera (XDI-VHR 90) at full field would generate approximately 2575 reconstructions. Remember that reconstructions can also be referred to as slices. The number of reconstructions generated can be estimated by dividing the height of the detector in microns by the pixel size, also in microns. In reality, the XDI-VHR 90 will not produce that many reconstructions because of the limited height of the synchrotron X-ray beam. As discussed previously in section 3.2, the size of the beam at the sample location in the BMIT-ID imaging hutch is approximately 11mm high x 220mm wide. Therefore, to get a realistic estimate of the number of reconstructions generated by each of the detectors, the beam height needs to be divided by the pixel size instead. This method gives a more accurate representation of the reconstructions generated for each view. The smaller the pixel size, the more reconstructions are generated. The XDI-VHR 90, X-ray SCMOS, and Hamamatsu Flat Panel generate 580, 440, and 110 reconstructions, respectively. The use of the detectors is discussed further in section 5.2.

The Hamamatsu Flat Panel's pixel size make it ineffective for PC-CT imaging. The 100-micron pixel size is too large to detect the phase change signal from the interfaces between tissues in the dog. Both of the Photonic Science detector's pixels' sizes are sufficient to detect the edge enhancement effect generated from PC-CT imaging (14), (9).

Chapter 5: Implementation of Canine Positioning Device

5.1 *Overview*

The specific objective of this thesis was to design, develop and implement a canine positioning system for the BMIT-ID beamline that would allow safe and effective imaging of live dogs. This section covers the implementation of the device. This chapter covers two main issues discovered and addressed during the implementation of the device: Positioning / Motion Artifact, and Locating the Prostate. Preventing motion artifact of the dog within the canine positioning device was a challenging issue. Several attempts at different methods of immobilization were tested to try to secure the dog for imaging. Section 5.2 goes over the different immobilization methods tested during the cadaver imaging. Locating the prostate for imaging was the second issue that was identified and addressed during the course of this research, which is discussed in section 5.3.

The canine positioning device was designed to allow for imaging of an *in-situ* canine prostate on the BMIT-ID beamline at the CLS. To this effect, a total of 15 dog cadavers and six live dogs were imaged using the canine positioning device between June 2015 and May 2016. The cadaver dogs were sourced for the Saskatoon Society for the Prevention of Cruelty to Animals, and were all a variety of breeds and sizes. The cadaver dogs were frozen post-mortem and kept in a freezer until two days before the experimental beam time at the CLS, when they were allowed to thaw at room temperature. The freezing and thawing of the cadavers altered the tissue structure, but this was unavoidable as no recently deceased cadavers could be sourced for the experiments. The live dog imaging occurred last, with all six dogs being imaged in May 2016. Each cadaver dog and live dog was imaged using PC-CT, the imaging modality previously discussed in section 3.3. The live dogs used for this research were scheduled for euthanizing for reasons not related to this thesis. For each of the cadaver and live dogs imaged a similar protocol was followed, where the dogs were immobilized in the canine positioning device, put up onto the stage in the BMIT-ID hutch and imaged using PC-CT. Due to the exploratory nature of this research, the imaging protocol used for each dog was modified and adjusted, based on lessons learned from imaging of previous dogs, and always with the specific goal of improving the PC-CT image reconstruction quality. Therefore, the imaging protocol for the first cadaver dog imaged is dramatically different from the last. The protocols for imaging live dogs were built off of the cadaver imaging protocol, but with several adjustments required to account for anesthesia and monitoring required. Table 5.1 describes the imaging parameters for the cadaver dogs 1-15, and Table 5.2 describes the parameters used for live dog imaging.

Table 5.1 – Overview of Cadaver Dog PC-CT

Dog Cadaver	Date Imaged (DD/MM/YY)	Filters in Beam	View Height (mm)	Magnetic Field Strength (T)	Views	Energy of Scan (keV)	Capture Time (ms)	Number of Projections	Detector
1	11/06/15	1 mm Al, 0.5 mm Cu	8.4	2.5	1-1	45	40	3600	XDI-VHR 90
					1-2	45	25	3600	
					1-3	45	32	3600	
					1-4	45	25	3600	
2	12/06/15	1 mm Al, 0.5 mm Cu	7.0	2.5	2-1	45	27	1800	XDI-VHR 90
					2-2	45	25	1000	
					2-3	45	30	1800	
					2-4	60	70	1000	
					2-5	70	22	3600	
3	24/06/15	1 mm Al, 0.5 mm Cu	7.3	2.5	3-1	50	170	3600	XDI-VHR 90
					3-2	70	200	3600	
					3-3	80	200	3600	
					3-4	60	250	3600	
					3-5	70	170	3600	
					3-6	90	60	3600	
4	25/06/15	1 mm Al, 0.5 mm Cu	7.5	2.5	4-1	90	50	3600	XDI-VHR 90
					4-2	90	450	3600	
5	30/07/15	1 mm Al, 0.5 mm Cu	7.7	2.5	5-1	60	900	3600	XDI-VHR 90
					5-2	60	900	3600	
					5-3	60	500	3600	
6	11/09/15	1 mm Al, 0.5 mm Cu	5.5	2.5	6-1	60	180	3600	XDI-VHR 90
					6-2	60	60	3600	
7	12/09/15	1 mm Al, 0.1 mm Cu	5.5	2.5	7-1	80	140	3600	XDI-VHR 90
					7-2	80	140	3600	
					7-3	80	700	3600	
8	12/12/15	1 mm Al, 180 mm Lucite	7.2	2.5	8-1	70	250	3600	XDI-VHR 90
					8-2	70	300	3600	

9	27/01/16	1 mm Al, 160 mm Lucite	8.7	2.5	9-1	70	600	1200	XDI-VHR 90
					9-2	70	150	1200	
10*	22/04/16	1 mm Al, 220 mm Lucite	9.3	2.5	n/a	n/a	n/a	n/a	XDI-VHR 90
11	06/05/16	1 mm Al, 140 mm Lucite	8.7	3.0	11-1	60	1500	1501	XDI-VHR 90
					11-2	60	1000	3751	
					11-3	60	950	1250	
12	17/05/16	1 mm Al, 160 mm Lucite	8.7	3.0	12-1	60	1500	3751	XDI-VHR 90
					12-2	60	100	4000	X-ray SCMOS
					12-3	60	100	4000	
					12-4	60	100	2000	
					12-5	60	100	4000	
13	21/05/16	1 mm Al, 160 mm Lucite	8.2	3.0	13-1	60	95	4000	X-ray SCMOS
					13-2	60	95	4000	
					13-3	60	95	4000	
					13-4	60	95	4000	
					13-5	60	95	4000	
					13-6	60	95	4000	
					13-7	60	45	8000	
					13-8	60	95	4000	
14	21/05/16	1 mm Al, 160 mm Lucite	8.2	3.0	14-1	60	195	8000	X-ray SCMOS
15	22/05/16	1 mm Al, 160 mm Lucite	8.0	3.0	15-1	60	95	4000	X-ray SCMOS
					15-2	60	95	4000	
					15-3	60	10	2000	Flat Panel
					15-4	60	10	2000	
					15-5	80	10	2000	
					15-6	80	10	2000	
					15-7	90	10	2000	
					15-8	90	10	2000	

Table 5.1: An overview of the canine cadaver imaging done at the CLS between June 2015 and May 2016. * Dog 10 was not imaged using PC-CT, and was only used to monitor for motion, but is included in this list because the device was still used. The three different detectors used are the Photonic Science Fiber Optic Camera XDI-VHR 90 (XDI-VHR 90), Photonic Science Fiber

Optic Camera X-ray SCMOS (X-ray SCMOS) and the Hamamatsu Flat Panel Detector (Flat Panel).

Table 5.2 – Overview of Live Dog PC-CT

Live Dog Imaged	Date Imaged (DD/MM/YY)	Filters in Beam	View Height (mm)	Magnetic Field Strength (T)	Energy of Scan (keV)	Views	Capture Time (ms)	Number of Projections	Detector
1	29/05/16	1 mm Al, 160 mm Lucite	8	3	60	1	95	4000	X-ray SCMOS
						2			
						3			
						4			
2	22/05/16	1 mm Al, 160 mm Lucite	8.2	3	60	1	95	4000	X-ray SCMOS
						2			
						3			
3	28/05/16	1 mm Al, 160 mm Lucite	8	3	90	1	27.2	1900	Flat Panel
						2	27.2	1900	
						3	27.2	1900	
						4	27.2	1900	
						5	27.2	760	
						6	61.2	1900	
						7	61.2	1900	
						8	61.2	760	
4	28/05/16	1 mm Al, 160 mm Lucite	8	3	90	1	27.2	1900	Flat Panel
						2	27.2	1900	
						3	27.2	1900	
						4	27.2	1900	
						5	27.2	760	
						6	61.2	1900	
						7	61.2	1900	
						8	61.2	760	
						9	61.2	1900	
						10	61.2	1900	
						11	61.2	1900	
5	29/05/16	1 mm Al, 160 mm Lucite	8	3	60	1	95	4000	X-ray SCMOS
						2	195	2000	

6	25/05/2016	1 mm Al, 160 mm Lucite	8	3	60	1 2 3 4 5 6 7 8 9	10	2000	Flat Panel

Table 5.2: An overview of the live dogs imaged at the CLS BMIT-ID beamline using the canine positioning device during May 2016. The two different detectors used are the Photonic Science Fiber Optic Camera X-ray SCMOS (X-ray SCMOS) and the Hamamatsu Flat Panel Detector (Flat Panel).

5.1.1 *Positioning*

The Pawsitioner® comes with several hook-and-loop straps (i.e. "Velcro") used to hold the dog stable during use. The device was originally designed to hold dogs in a supine horizontal position for conventional CT imaging (95). As described previously, the canine positioning device holds the dog in a near vertical position in order to minimize the amount of the subject the beam will have to traverse, and to minimize the radiation exposure of the dog. At the start of this project it was not known if the hoop-and-loop straps would be sufficient to support the dog during imaging. Therefore, for the first dog imaged, only the hook-and-loop straps were used to hold the dog within the positioning device during scanning, as shown in Figure 5.1. Using only these straps to secure the cadaver in the device did not prove to be sufficient for immobilizing the dog during scanning. The dog was visibly seen sliding down in the Pawsitioner during the duration of the scan, and therefore a different method of securing the dogs were investigated.

Figure 5.1: Cadaver 1imaged using the canine positioning device. The dog’s front and rear legs are secured with the hook-and-loop straps, indicated with the black arrows. The orange straps across the abdomen is vet wrap, used to secure the black padding (towels) seen bilaterally between the cadaver and the Pawsitioner.

For Cadavers 2-8 a Ruffwear® Load Up™ Harness (Bend, OR), a canine travel harness designed to restrain dogs during transport was used to help immobilize the dogs, and for cadavers 9-15 a Walkabout™ Front harness, (Santa Cruz, CA) a sling device to provide extra support and help a dog stand and walk with orthopedic or neurologic gait problems was utilized. The hook-and-loop straps were also used along with their respective harnesses to secure the cadaver for imaging. The Load Up™ and Walkabout™ harnesses, used in their intended form, can be seen in Figure 5.2. Figures 5.3 and 5.4 show dog cadavers secured in the canine positioning device with the Load Up™ and Walkabout™ harnesses, respectively.

Figure 5.2: (a): The Walkabout™ Front Harness (Santa Cruz). (b): The Ruffwear® Load Up™ harness (Bend, OR) (104), (105).

Figure 5.3: Cadaver two secured using the Ruffwear® Load Up™ harness (red arrow), and the hook-and-loop straps (white arrows) within the positioning device for imaging.

Figure 5.4: An example of a dog cadaver secured into the canine positioning device by the Walkabout™ front harness. The harness is indicated by a red arrow, and the hook-and-loop straps indicated black arrows.

5.2 *Motion Artifact*

Motion artifact refers to the movement of the dog within the canine positioning device caused by gravity. For the first several month of data collection it was not known that motion artifact was a major issue. This was due to a variety of other confounding issues, such as technical problems with BMIT and the CLS, positioning of the cadaver within the device, beam energy selection, tomographic projection capture number, technical problems with the X-ray detector, and difficulty in locating the prostate for imaging. It was only by examination of previously collected data from the first eight cadavers and multiple consultation with researchers from the

CLS that motion was identified as a major obstacle. In retrospect, both the Load Up™ and Walkabout™ harnesses did not sufficiently immobilize the cadaver dogs for imaging. There was a large amount of motion artifact in the scans obtained using these devices in conjunction with the Pawsitioner, making reconstruction quality extremely poor. The Walkabout™ harness was used for all of the live dog imaging as well, along with a modification to the device, described in section 5.1.3. The first time the motion artifact was calculated was after the imaging of the ninth dog cadaver, and each subsequent imaging shift was use to try to reduce the motion of the dog during scanning. This section describes how each of the cadavers were secured into the canine positioning device, and the steps taken to reduce motion.

Due to the mathematical nature of the algorithms used to do the CT reconstructions, the object being scanned needs to remain near stationary while scanned (82). For small samples, such as excised canine prostates in a jar of gelatin, this is not an issue, but for larger samples, such as a cadaver, this issue proves very challenging. In clinical CT, where the patient is supine, the immobilization issue is minimal, and usually revolves around the involuntary movements of the body, such as breathing and heart movements (98). The scan time of clinical CT is also several orders of magnitude shorter than synchrotron PC-CT, around 10 seconds per scan, therefore greatly reducing the risk of motion artifacts during clinical CT scanning compared to PC-CT. Due to the near-vertical nature of which the cadaver for PC-CT imaging in the canine positioning device, extra care was taken to secure the cadaver to help limit slumping due to the force of gravity.

The maximum amount of movement allowed during a scan is dependent on the imaging detector's pixel size and scan time (82). This is because the algorithms used for CT reconstruction assumes no movement of the object during the entire scan. Only a slight amount of movement can be tolerated for the reconstructions to be accurate (98). The tolerated movement size is equal to the pixel size of the detector. Therefore, the Hamamatsu Flat Panel has the highest tolerance to movement per scan, the X-ray SCMOS in intermediate, and the XDI-VHR 90 has the least. The other important factor to consider when dealing with the motion issue is the total scan time required for each view. The shorter the scan time, the less time there is for the cadaver to slump. As described previously in section 4.6, the Hamamatsu Flat Panel detector has the shortest scan time, compared to the other two detectors, of approximately 27 seconds for a 180° scan of 4000 tomographic projections. With this information, a maximum movement tolerance for the detector can be estimated by dividing the pixel size by the scan time, giving a tolerance of 3.7 μm/s for the Hamamatsu Flat Panel detector.

$$Motion\ Tolerance\ (\mu m/s) = \frac{Detector\ Pixel\ Size\ (\mu m)}{Scan\ Time\ (s)} \tag{5.1}$$

The movement tolerance describes the maximum "speed" or distance in a given time the cadaver can be moving before the reconstruction quality is affected resulting in motion artifacts. To increase the motion tolerance, either the scan time can be reduced or the pixel size can be increased. However, the pixel size is a physical property of the detector, and therefore the only practical approach to increase the movement tolerance is to reduce the scan time. Two steps can be taken to decrease the scan time: decrease the amount of tomographic projections captured over 180°, and increasing the frame rate of the detector. For example, if the number of tomographic projections is halved, the motion tolerance will double.

$$Scan\ Time\ (s) = \frac{\#\ of\ Tomographic\ Projections\ Taken}{Frame\ Rate\ (s^{-1})} \tag{5.2}$$

The motion tolerance of any detector is not perfect. That is to say, the formula assumes near uniform linear motion of the cadaver being imaged, which is highly unlikely. The motion tolerance of the Hamamatsu Flat Panel detector only holds true if the cadaver moves in one dimension at a constant speed of less than 3.7 µm/s. In reality, the cadaver being imaged can move in multiple dimensions, at multiple rates, and experiences variable accelerations for the duration of the scan. This means that parts within the cadaver may be moving at different rates in different directions while held in the positioning device during scanning which is contrary to the requirement of a near stationary sample being imaged. The motion tolerance equation does not describe the effect that motion during scanning will have on reconstruction quality, rather the equation is only a tool to help explain that even microscopic movements of the cadaver can effect reconstruction quality. The equation does not describe a movement threshold which after crossing will immediately result in poor reconstructions.

One way to assess motion post-scanning is to take the first tomographic projection and compare it to the last horizontally inverted tomographic projection of the scan. This is called a motion artifact test. The first projection is taken at 0° and the last at 180°, and therefore they should be mirror images of each other. By horizontally inverting the final tomographic projection, a direct comparison can be made between the initial and final projection images. If the sample has been completely stationary during scanning, the inverted final projection should exactly overlay the initial projection. An example of a perfect scan (i.e. one without any cadaver motion) can be seen in Figure 5.5, though it is artificially made and only for example purposes.

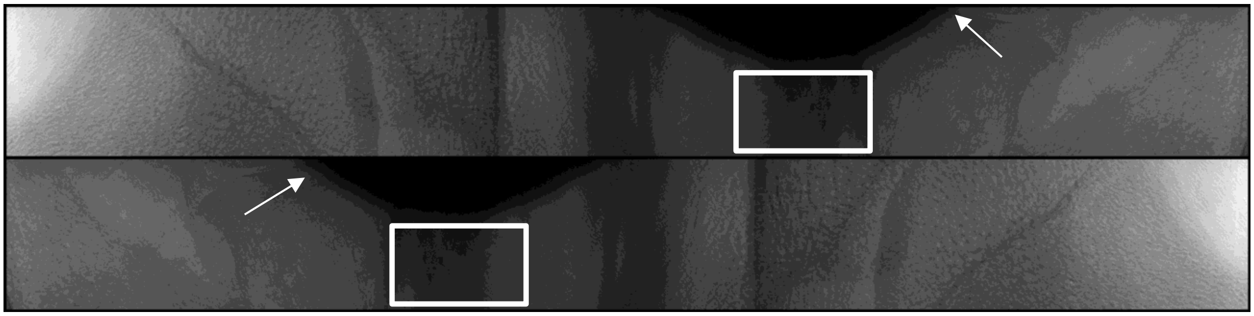

Figure 5.5: An example of a scan without any sample motion, the top image is the initial tomographic projection at 0° and the bottom image is the final at 180°. Notice that they are mirror images of one another. This figure was generated by taking the initial projection and making a copy imaged inverted horizontally. This image is from the fifth view of cadaver 2. Iodine contrast agent was injected into the bladder of the cadaver through a urethral catheter. The bladder can be seen in both the top and bottom image as the dark semi-circle, indicated with the white arrow in each. The prostate area is indicated with a white box.

The real initial and final tomographic projection of the fifth view of the second dog are shown below in Figure 5.6. The movement of the bladder is extremely apparent when comparing the images together. The bladder moved 321 pixels horizontally and 258 pixels vertically, translating into a movement of 5.4 mm horizontally and 4.3 mm vertically. Interestingly, the bone in the same scan moves less vertically but more horizontally compared to the bladder. The bone appears to move 6.4mm horizontally and only 0.2mm vertically from the first to last projection.

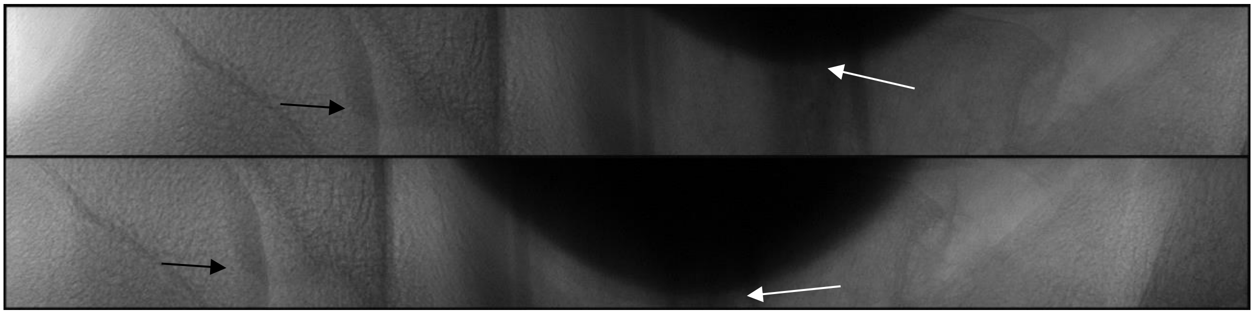

Figure 5.6: The initial (top) and final (bottom) tomographic projections of the fifth view from cadaver 2 scanned using the canine positioning device. The bottom image has been flipped horizontally. The movement of the bladder is extremely apparent when comparing the top and bottom image, shown with a white arrow. Bone movement is harder to see, but is still apparent, shown with black arrows.

ImageJ, a software used for medical imaging, was used to measure the distances from Figure 5.5 and 5.6. The view shown above in Figure 5.6 has a low movement tolerance of 4.72×10^{-3} µm/s due to its large scan time of 60 minutes. The 60-minute scan time is due to the low frame rate of the detector used to capture this view, the Photonic Science Fiber Optic Camera XDI-VHR 90. The apparent movement of the bladder was 6.9 mm over the entire scan, assuming a linear relationship between the movement of 5.4 mm horizontal and 4.3 mm vertical. A movement of 6.9 mm translates to a bladder motion of 2.7 μm/s, several order of magnitudes greater than the movement tolerance of the scan. The bone in the same view has a slightly lower motion of 2.5 μm/s. Figure 5.7 shows a montage of the view shown above, with several tomographic projections between the beginning and end of the scan. This figure shows how the bladder slumps significantly more than the rest of the objects within the view.

Due to the movement of the cadaver during scanning, the quality of the reconstructions was low, as seen in Figure 5.8. No soft tissue contrast is apparent, but a rough figure of bone can be seen on the left of the reconstructed image. The large white oval shape is the bladder filled with contrast agent, but the shape is undefined. Iodine based contrast agent is used to better locate the prostate, discussed further later. The speckles in the top right of the image is thought to be fecal matter, indicated with a yellow arrow. The prostate cannot be seen in Figure 5.8, nor in any of the reconstructions from this second cadaver.

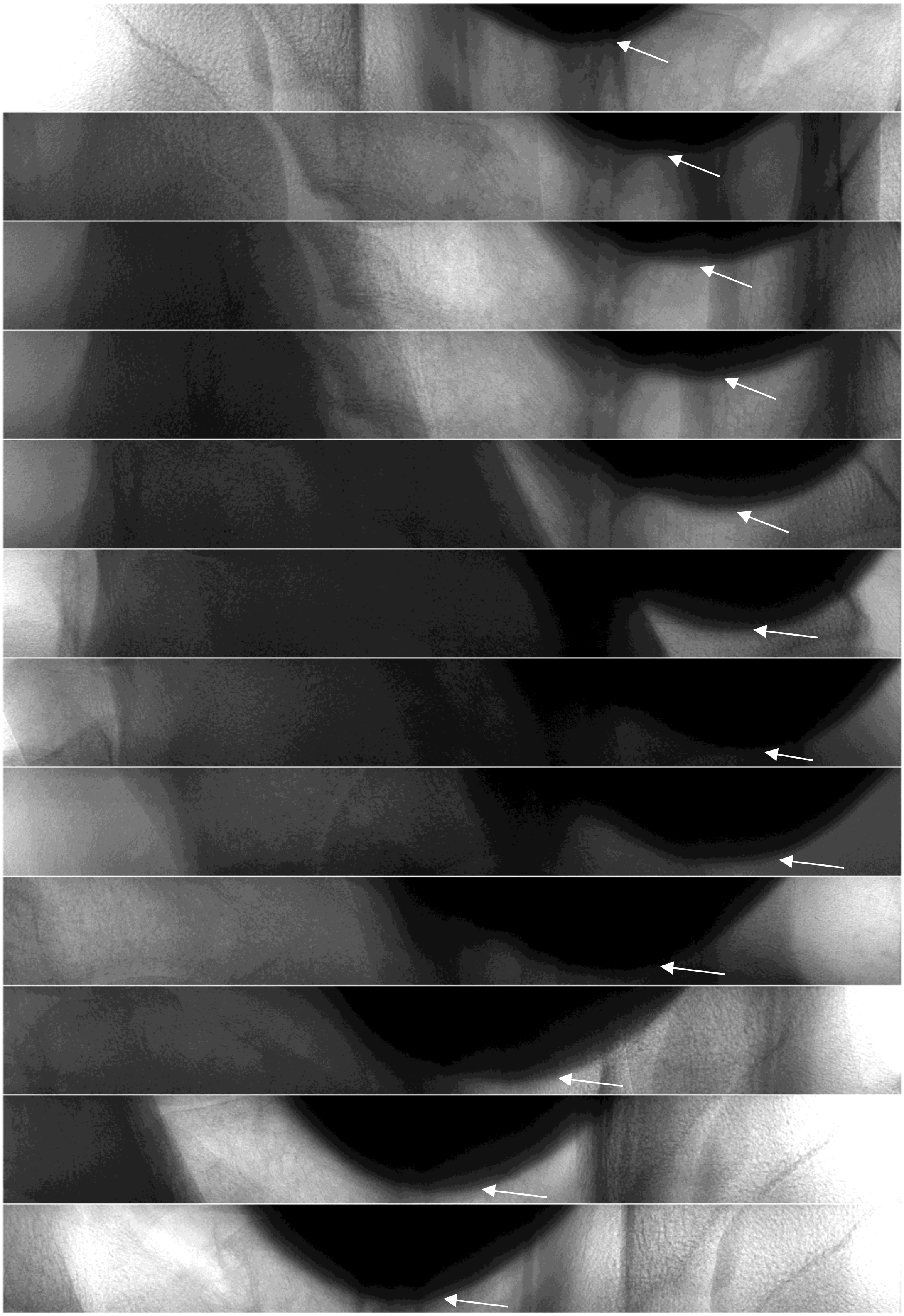

Figure 5.7: A montage of the fifth view from cadaver 2. The top and bottom images represent the initial and final tomographic projections of the scan, respectively. The ten images between

show the vertical displacement of the bladder during the scan. The bladder is indicated with a white arrow in each of the twelve images.

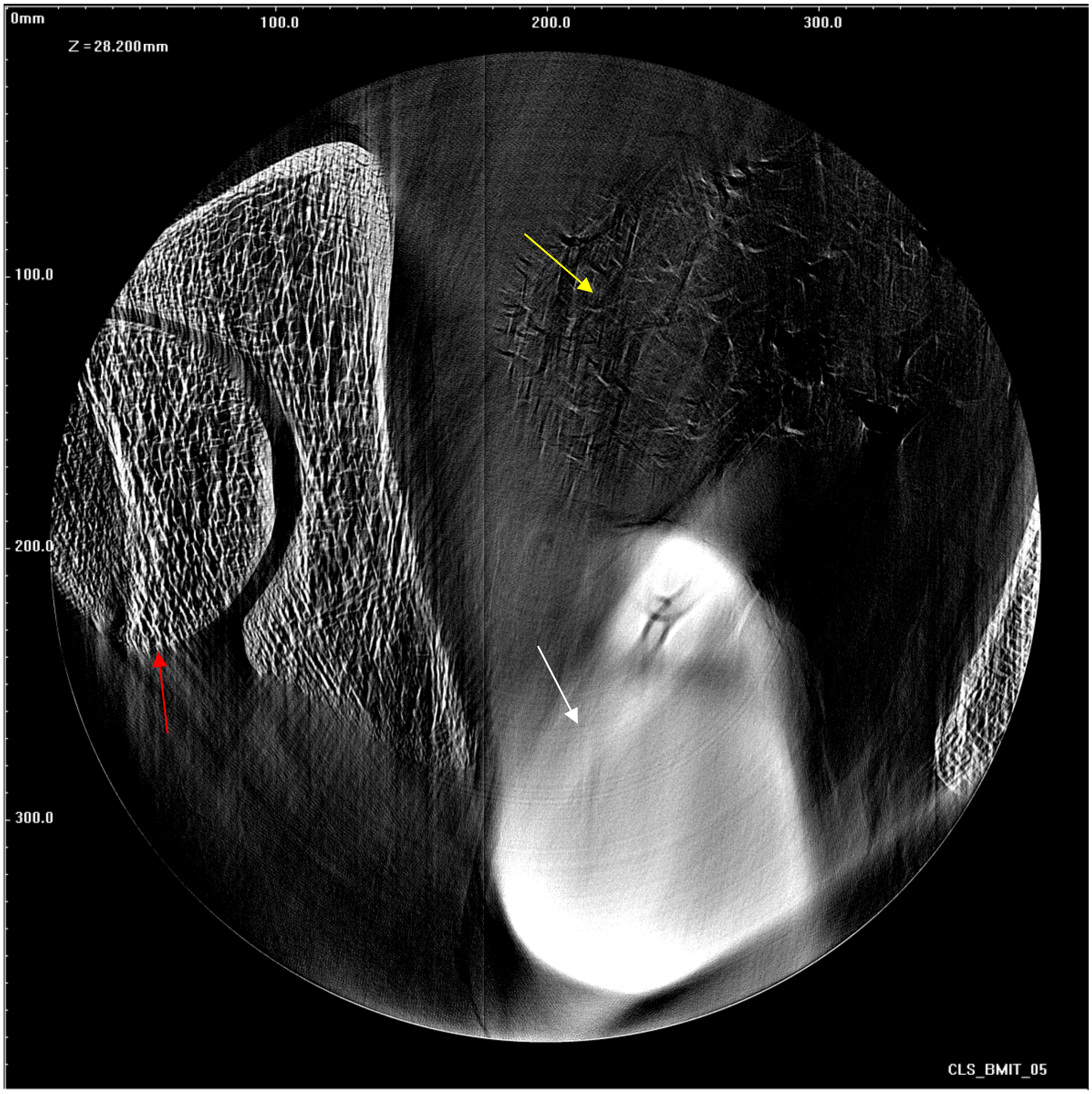

Figure 5.8: A reconstruction from the fifth view of cadaver 2 with the canine positioning device. The head of the femur, bladder, and fecal matter are indicated with a red, white, and yellow arrow, respectively.

The highest quality reconstructions from the 15 cadavers imaged came from the third dog, a small, long-haired dachshund, perhaps because of the small size of the dog. The scans of this cadaver took approximately 60 minutes, and were captured with the Photonic Science Fiber Optic Camera XDI-VHR 90. The scans had a calculated movement tolerance of 4.7 x 10^{-3} µm/s. The higher quality of the reconstructed images is related to the movement speed of the third dog, approximately 0.011 µm/s. The movement speed of this cadaver is two orders of magnitude smaller than for cadaver 2, and therefore much closer to the movement tolerance required for successful scanning, 4.7 x 10^{-3} µm/s. An example reconstruction from dog three can be seen in Figure 5.9. The pelvic bone, penile tissue, and urethral catheters are evident in 5.9 and the rough area of the prostate can be seen. The movement tolerance for dogs 1 – 15 are shown in Table 5.3. To address the motion issue, the canine positioning device was modified, as described below in 5.1.3. Motion artifact tests were not conducted on the live dogs due to wanting to keep the radiation dose delivered as low as reasonably achievable, and these tests expose the dogs to a large amount of extra dose.

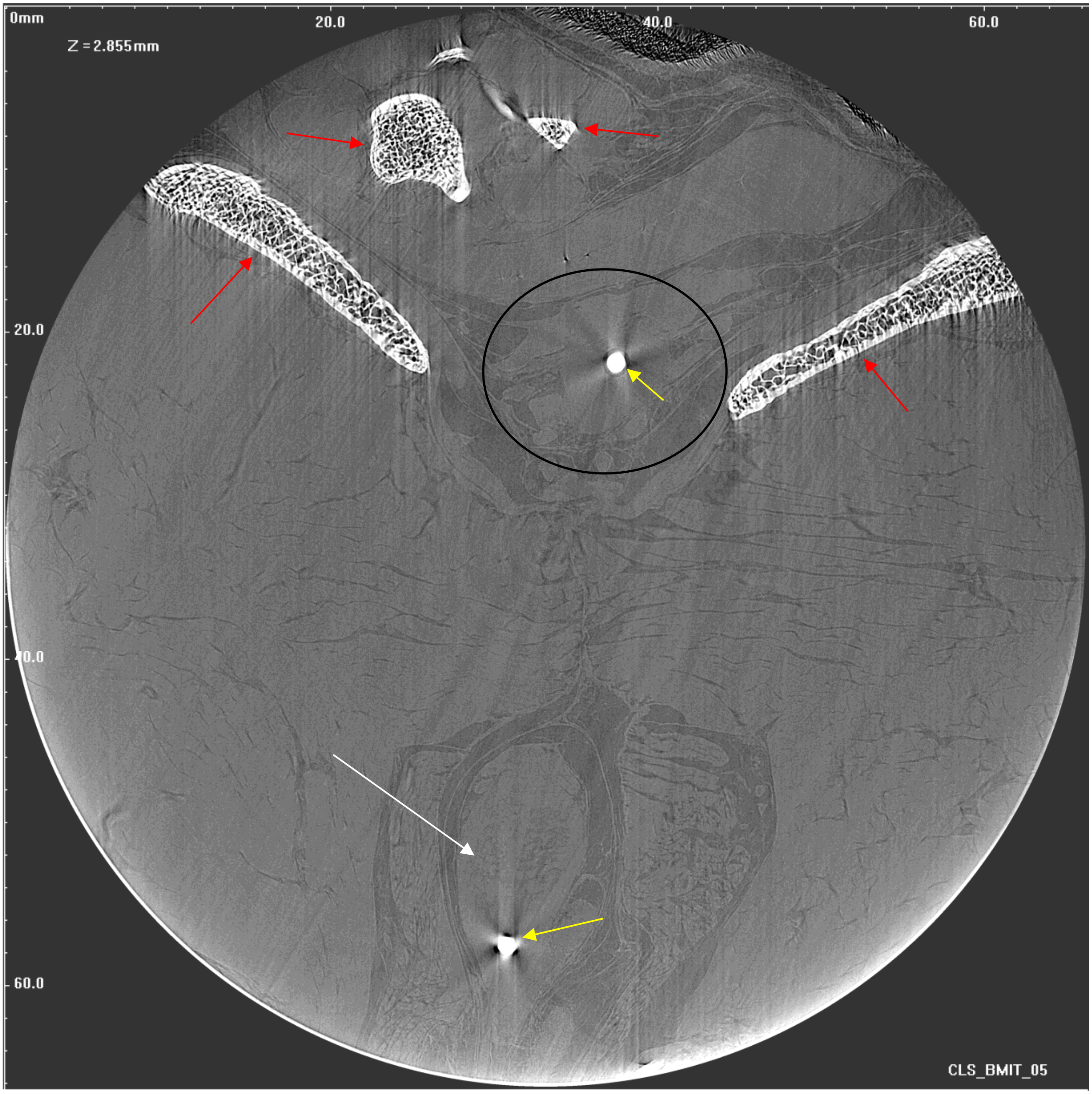

Figure 5.9: A reconstruction from the second view from cadaver 3 with the canine positioning device. The pelvic bone, penile tissue, and urethral catheters are indicated with a red, white, and yellow arrow, respectively. The same catheters can be seen twice due to the catheter passing through the penis and the prostate. The rough area of the prostate is marked with the black circle.

Table 5.3 – Movement Tolerance of PC-CT Scans Using Canine Cadavers

Dog	View	# of Tomographic Projections	Capture Rate (FPS)	Pixel Size (µm)	Scan Time (S)	Movement Tolerance (µm/s)	Apparent movement (µm/s)	Detector
1	1	3600	1	17	3600	0.00472	1.99	XDI-VHR 90
	2	3600	1	17	3600	0.00472	1.98	
	3	3600	1	17	3600	0.00472	1.85	
	4	3600	1	17	3600	0.00472	1.88	
2	1	1800	1	17	1800	0.00944	4.17	XDI-VHR 90
	2	1000	1	17	1000	0.017	6.63	
	3	1800	1	17	1800	0.00944	3.86	
	4	1000	1	17	1000	0.017	6.58	
	5	3600	1	17	3600	0.00472	6.90	
3	1	3600	1	17	3600	0.00472	0.27	XDI-VHR 90
	2	3600	1	17	3600	0.00472	0.15	
	3	3600	1	17	3600	0.00472	0.0283	
	4	3600	1	17	3600	0.00472	0.10	
	5	3600	1	17	3600	0.00472	0.0633	
	6	3600	1	17	3600	0.00472	0.12	
4	1	3600	1	17	3600	0.00472	0.30	XDI-VHR 90
	2	3600	1	17	3600	0.00472	0.18	
5	1	3600	1	17	3600	0.00472	2.70	XDI-VHR 90
	2	3600	1	17	3600	0.00472	2.53	
	3	3600	1	17	3600	0.00472	3.00	
6	1	3600	1	17	3600	0.00472	0.47	XDI-VHR 90
	2	3600	1	17	3600	0.00472	0.48	
7	1	3600	1	17	3600	0.00472	0.35	XDI-VHR 90
	2	3600	1	17	3600	0.00472	0.42	
	3	3600	1	17	3600	0.00472	0.44	
8	1	3600	1	17	3600	0.00472	0.77	XDI-VHR 90
	2	3600	1	17	3600	0.00472	0.87	
9	1	1200	1	17	1200	0.0142	1.23	XDI-VHR 90
	2	1200	1	17	1200	0.0142	1.13	
10	1	n/a	n/a	n/a	n/a	n/a	0.0189	XDI-VHR 90
11	1	1501	1	17	1501	0.0113	0.78	XDI-VHR 90
	2	3751	25	25	150.04	0.167	0.64	
	3	1250	25	25	50	0.5	0.25	

12	1	3751	25	25	150.04	0.167	0.0750	XDI-VHR 90
	2	4000	25	25	160	0.156	0.0750	X-ray SCMOS
	3	4000	25	25	160	0.156		
	4	2000	25	25	80	0.313		
	5	4000	25	25	160	0.156		
13	1	4000	25	25	160	0.156	1.06	X-ray SCMOS
	2	4000	25	25	160	0.156		
	3	4000	25	25	160	0.156		
	4	4000	25	25	160	0.156		
	5	4000	25	25	160	0.156		
	6	4000	25	25	160	0.156		
	7	4000	25	25	160	0.156		
	8	4000	25	25	160	0.156		
14	1	4000	25	25	160	0.156	0.94	X-ray SCMOS
15	1	8000	25	25	320	0.0781	1.01	X-ray SCMOS
	2	4000	25	25	160	0.156		
	3	8000	146	100	54.79	1.83	1.01	Flat Panel
	4	4000	146	100	27.40	3.65		
	5	4000	146	100	27.40	3.65		
	6	2000	146	100	13.70	7.3		
	7	2000	146	100	13.70	7.3		
	8	2000	146	100	13.70	7.3		

Table 5.3: The number of projections, scan time and movement tolerance of each view as well as pixel size and capture time of the detector are described. Notice that with the Hamamatsu Flat Panel detector the movement tolerance is several orders of magnitude greater than the Photonic Science Fiber Optic Camera XDI-VHR 90 or the Photonic Science Fiber Optic Camera X-ray SCMOS. All apparent motions are well above tolerable levels.

5.2.1 *Seat Modification*

A modification was made to the canine positioning device after the ninth cadaver was imaged. The slumping issue was not well understood until after the ninth dog cadaver was imaged. To address the issue, a seat was added near the bottom of the Pawsitioner, which supported the dog from below. The seat took some of the weight off of the upper harness, and provided a firm base for the lower half of the dog. The modification consisted of a pump-jack attached to a bicycle seat, with which the height of the seat could be adjusted. A before and after picture of the canine positioning device can be seen in Figure 5.10. The modified canine positioning device was used to image the last four canine cadavers, dogs 11-15. Dog ten was used to initially test the seat device, but did not undergo PC-CT. The modified seat was also used during the imaging of the six live dogs. The modified seat can also be seen in Section 5.4, Figure 5.13.

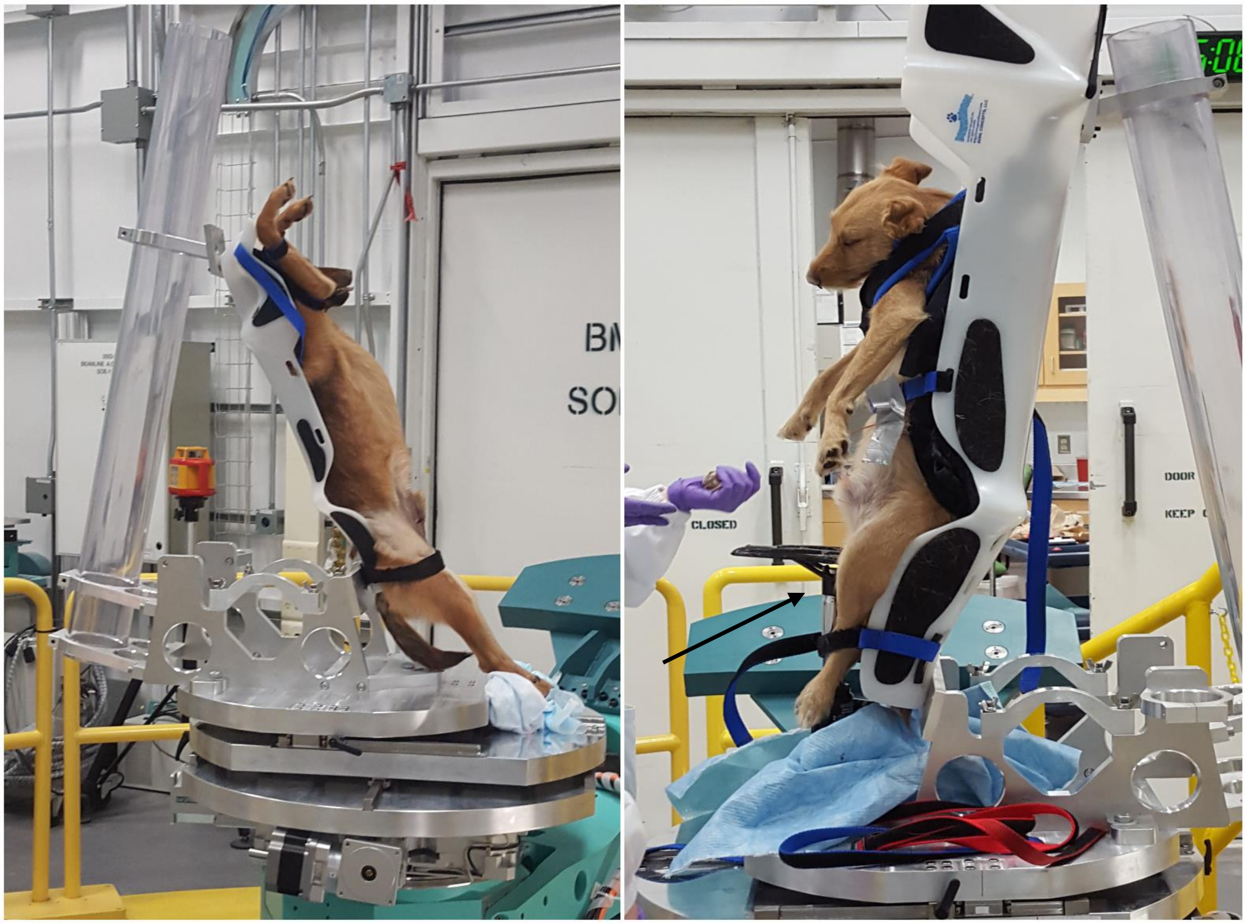

Figure 5.10: Left: The unmodified canine positioning device. Right: the modified device with the seat attached near the base of the Pawsitioner, indicated with a black arrow. The height of the seat is adjustable to match the size of the dog being imaged.

5.3 *Locating the Prostate*

The canine prostate is typically located equally in the abdomen and pelvic cavity, though this would not be the case for neutered dogs, whose prostates would be found exclusively in the pelvic canal (39). When the dog is positioned in a near vertical orientation in the canine positioning device, the prostate appears to shift downwards into the pelvic cavity. The prostate needed to be located before each scan due to the small area that the beam can image, only 10 mm x 1 mm. Accurately locating the prostate for imaging presented a significant challenge at the CLS that was eventually overcome through experimentation with different locating methods. With experimentation with these methods the prostate can now accurately be centered in the beam before scanning is initiated. This is an improvement over the first cadaver imaged, where the imaging area was only assumed to contain the prostate. This section covers the external and internal methods of locating the prostate for PC-CT in the canine positioning device. Locating the prostate occurs in two sequential steps, the external then internal methods. The external methods can be thought of as rough positioning of the prostate within the imaging field of view, and the internal methods as fine-tuning of the position.

There are two positioning lasers located within the imaging hutch on the BMIT-ID beamline. These two lasers are positioned on walls perpendicularly to one another, and project a straight line that divides the hutch into halves. The intersection of the two lasers occurs at the center of the stage rotation. Therefore, these lasers can be used to position a sample accurately in the center of rotation for the stage. When the canine positioning device is mounted onto the stage in the hutch, the lasers can be used to align the center of the dog roughly in the center of rotation for the stage. This rough centering is accomplished using the x-y stages located at the bottom of the positioning device, which can be adjust to ±10mm in both the X and Y dimensions. To simplify the locating procedure, the dog can be thought of as a near perfect cylinder, with the prostate being located near the center. Therefore, if both the lasers travers the dog down the center line, the prostate should be roughly centered in the beam. Although this external method aligns the transverse abdominal plane of the dog in the center of rotation (referred to as the X and Y dimension), it does not address the height at which this plane traverses the prostate within the dog (referred to as the Z dimension). The X and Y dimensions are the width and length of the prostate cross section, respectively, while the Z dimension describes the length of the prostate in the dorsal section as seen previously in Figure 3.8 and 4.1. The location of the prostate can be estimated visually when the dog is held within the canine positioning device prior to imaging. The imaging hutch has a third laser which projects a plane line parallel to the floor and ceiling at the height the beam traverses the stage's center of rotation. Using these three lasers, the X, Y, and Z dimensions of the approximate prostate location can be centered in the beam.

Prior to imaging, internal localization methods can be employed to increase the likelihood that the prostate will be located within the imaging field of view. A key anatomical feature to help locate the prostate for imaging is the urethra. The urethra traverses the prostate in its entirety, both in canine and human prostates, and opens into the bladder at the cranial end of the prostate. A Foley catheter can be inserted into the urethra through the penis of the dog. When the balloon of this Foley catheter is inflated it will secure the catheter at the neck of the bladder just cranial to the prostate; locating this catheter balloon can be used to internally locate the prostate with the help of the X-ray beam. Foley catheters have two separate channels running down their length, one for draining urine from the bladder with openings at both ends, and one with only one valve opening used to inflate a balloon near the tip of the catheter. In clinical setting the Foley catheter's balloon can be inflated once placed to prevent the catheter from accidentally being removed from the bladder. The inflated balloon is too large to pass from the bladder down the urethra, and therefore the catheter remains in the neck of the bladder, just cranial to the prostate. The inflated Foley's catheter balloon was used for the internal method of localizing the prostate for PC-CT imaging. Iodine contrast agent, in the form of diatrizoic acid, was injected into the balloon of the Foley catheter which allowed the neck of the bladder and urethra to be visualized using X-rays. The diatrizoic acid was purchased from AK Scientific, Inc. California, under the brand name H919, with a concentration of 98% (106). Two milliliters were injected into the Foley catheter balloon. The contrast is very visible due to the higher X-ray absorption of iodine compared to soft tissues at the same photon energy. The mass attenuation coefficient of iodine at 50 keV is 12.32 cm^2/g, while soft tissue's is only 0.22 cm^2/g (78).Therefore, the iodine contained within the catheter is very visible when images are captured. Additionally, the catheter prevents the iodine contrast from diffusing through the tissues including into the prostatic ducts. When using a Foley catheter to administer contrast agent, the balloon filled with contrast agent can be visualized at the neck of the bladder, and therefore the prostate should be located caudally to its position. This method can be seen in Figure 5.11, where the white arrow indicates the Foley catheter balloon, and a white box indicates the location of the prostate. The final step in locating the prostate is to rotate the dog 90-180°, while insuring that the Foley balloon catheter remains within the field of view; this is used to confirm that the prostate itself will remain in the field of view throughout imaging. If the balloon moves too far away from the center of the image the stages must be adjusted accordingly to re-center it.

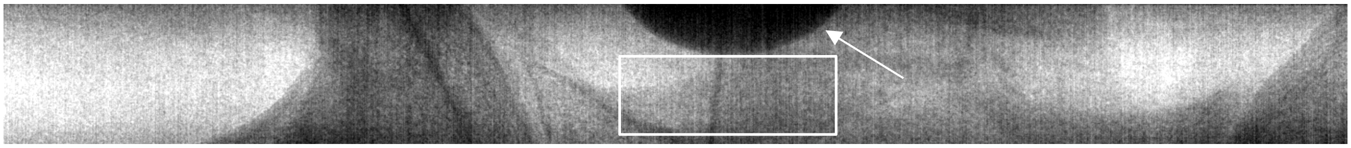

Figure 5.11: A tomographic projection from the first of the six live dogs imaged. The dark semi-circle indicated with a white arrow is the balloon of the Foley catheter filled with iodine contrast agent, stuck within the neck of the bladder. The prostate is located just below, in the white box, but cannot be seen directly in this image due to the poor soft tissue contrast.

Due to the small vertical view size of the images captured on the BMIT-ID beamline, several projections taken at different view heights can be stitched together to create a larger radiographic image. These images are referred to as a scout montage, an example is shown in Figure 5.12, taken from the sixth canine cadaver imaged. The montage is of 12 tomographic projections, taken at the same angle but different heights within the dog's pelvic region, stacked one on top of each other. The view height is 5.5 mm, and captured with the Photonic Science Fiber Optic Camera XDI-VHR 90. The pelvic bone and vertebrae can be seen in the montage, outlined and indicated with white arrows. Unfortunately, the Foley catheter was not used to locate the prostate until the ninth dog imaged so is not available as a localizing landmark for the prostate in this image.

Figure 5.12: A scout montage from the fifth view of the sixth dog imaged using the canine positioning device. The wings of the pelvis are outlined in white, and the vertebrae are indicated with white arrows. The bone appears darker than the surrounding soft tissue because of the higher X-ray absorption.

5.4 *Live Dog Imaging*

5.4.1 *Overview*

The conclusion of this thesis focuses on the final stage and implementation of the canine positioning device, live dog imaging. All of the previous work shown with cadavers was done to prepare for the imaging of live dogs. Live imaging was done on six dogs during May 2016. The University of Saskatchewan Animal Research Ethics Board, operating in accordance with the guidelines set out by the Canadian Council on Animal Care, reviewed and approved the use of live animal subjects and animal tissues for the purposes of this thesis. The dogs were held in the canine positioning device in a similar way to the cadavers, with the Walkabout™ front harness used to secure their upper body into the Pawsitioner. The live dog imaging used the modified seat to secure the lower end of the dog, and to help reduce the motion of the dog during scanning. The setup of live dog imaging was more complex compared to cadaver imaging due to the necessary equipment needed to keep the live dog anesthetized during imaging. Care was taken to ensure that each dog did not receive a lethal dose of radiation during imaging, as these live dog experiments were meant to be non-lethal. After imaging, each of the dogs were recovered from anesthesia and monitored for any signs of acute radiation syndrome. Symptoms of acute radiation syndrome monitored for include: red skin, hair loss, bloody and loose stool, nausea, anorexia, vomiting, and weight loss (107). None of the dogs became symptomatic post-imaging. An image of the live dog in the canine positioning device can be seen in Figure 5.13. An oxygen tank, intubation tube, anesthetic gas filter, anesthetic, anesthetic ventilator, ventilation bag, intravenous (IV) line, saline IV, pressure IV bag, vital monitoring equipment, oxygen flow regulator, and various tubing were used during live dog imaging, along with the Foley catheter, Walkabout™ front harness, hook-and-loop straps, and the modified seat.

The oxygen tank used for imaging was a size M^3, with 700 L of oxygen sourced from Praxair, Saskatoon, SK. The tank is indicated in Figure 5.13 with a yellow arrow. An Easy Dial Reg™ oxygen regulator (Precision Medical Inc, Northampton, PA) was used to control the flow rate of O_2. Size 9.5, 10 and 11mm cuffed endotracheal tubes were used for intubation, sourced from the Western College of Veterinary Medicine (WCVM), Saskatoon, SK. The Fortec 3™ anesthetic vaporizer (Cyprane Limited, Yorkshire, U.K.) used is specified for isoflurane 100% (Piramal Critical Care, Bethlehem, PA), was used for all dogs. The anesthetic gas filter is a Breath Fresh™ charcoal filter sourced manufactured by Jorgensen Labs Inc, Loveland, CO. The re-breather bag used for ventilation was sourced from the WCVM, anesthesia department, Saskatoon, SK. A three or five-liter bag was used during imaging, depending on the size of the dog. Normosol-r™ (Hospira, St. Laurent, QC), 1000 ml, was used as the IV solution for each of the dogs imaged, and the IV line used was a Macro-Drip fluid administration set (DeRoyal, Powell, TE). The IV bag was pressurized with a Infu-Surg® pressure infusion bag, used to increase IV flow rates (Anetic Aid, West Yorkshire, U.K). A B3MVet Next© device (Bionet America Inc, Tustin, CA) was used to monitor the dog’s vitals during imaging. This permitted us to tract trends in the heart rate and rhythm, O_2 saturation (fraction of oxygen saturated hemoglobin relative to total hemoglobin), non-invasive blood pressure monitoring, respiration rate, temperature, and capnography (end tidal CO_2). The B3MVet Next© device was modified to broadcast reading outside of the BMIT imaging hutch to the control room.

Imaging of all live dogs was under direct supervision of a veterinarian (Dr. Elisabeth Snead, DVM, University of Saskatchewan). Hydromorphone (0.05 mg/kg, 10 mg/mL) and Acepromazine (0.02 mg/kg, 10 mg/mL) were used as intramuscular pre-anesthetic medication. The dog was induced with a bolus of intravenous propofol (4 mg/kg, 10mg/mL) before being intubated and maintained on inhalant gas anesthesia (isoflurane 1-2%). Following this the dog was secured into the Pawsitoner using the Walkabout™ front harness and the hook-and-loop straps. The Walkabout™ front harness was modified based off of the poor results with the cadavers. The size of the harness was increased to cover a larger surface area over the dog, and several more straps were sown onto it to provide extra support. The dog was kept anesthetized throughout, and secured into the positioning device on the stage within the BMIT-ID imaging hutch. The modified seat was used to secure the lower limbs and pelvic region of the dog. The oxygen tank, vaporizer, IV drip, and anesthetic gas scavenger were all attached to the base of the positioning device, meeting the design requirement of the device. The monitoring equipment was attached to the dog at the appropriate locations, and the monitor was secured to the imaging platform, indicated in Figure 5.13 with a black arrow.

Figure 5.13: An image of a live dog set up for imaging at the CLS BMIT. The oxygen tank, vaporizer, IV drip and gas filter are indicated with a yellow, blue, green, and red arrow, respectively. The monitoring equipment is indicated with a black arrow. The modified seat can also be seen in this image, indicated with a white arrow.

5.4.2 *Radiation Dose*

The radiation dose delivered was a large consideration during the live dog imaging. X-rays are ionizing radiation, and can cause damage to living tissues. The damage from X-ray exposure has been well documented in both human and veterinary medicine (108), (109). An ion chamber was used on the BMIT-ID beamline to estimate the surface dose rate the dog received during imaging. The surface dose rate delivered to the dog ($\dot{D}_S$) can be estimated by multiplying the ion chamber dose rate ($\dot{D}_\iota$) by a magnification ratio between the source - ion chamber distance ($X_{s\rightarrow I}$ = 51m) and the source - sample distance ($X_{s\rightarrow S}$ = 55m), and then dividing the results by π (110), (111).

$$\dot{D}_S = (\dot{D}_\iota)\left(\frac{X_{S\rightarrow I}}{X_{S\rightarrow S}}\right)^2 (\pi^{-1}) \qquad [5.3]$$

Previous research lead to the adoption of a two gray (Gy) dose limit for each of the dogs during imaging as no symptoms of acute radiation syndrome appear at surface doses below this dose (107). The ion chamber dose rate and surface dose rates at the dog are shown in Table 5.4, along with the calculated total amount of time the dog could be imaged while not exceeding the total dose allowance. The dose received by the dog is contained to the area irradiated by the beam, (i.e. the specific area of each view). Each dog was imaged multiple times at multiple areas, with no overlap between the irradiated areas to prevent the dose limit from being reached.

Dog	($\dot{D}_\iota$) Ion Chamber Dose Rate, (mGy/s)	($\dot{D}_S$) Calculated Surface Dose Rate (mGy/s)	Calculated Maximum Scan Time Allowed per View (s)	Experimental Scan Time per View (s)	Calculated Experimental Surface Dose Delivered per View (mGy)
1	10.0	2.74	729	400	1096
2	9.30	2.55	784	400	1020
3	1.14	0.31	6451	186	58
4	1.18	0.32	6250	186	60
5	10.0	2.74	729	400	1096
6	0.6	0.16	12500	20	3.2

Table 5.4: The experimental surface dose delivered to each of the live dogs imaged at BMIT.

The surface dose of dogs 1, 2 and 5 was the highest of the six dogs imaged due to the use of the Photonic Science Fiber Optic Camera X-ray SCMOS to capture the projections. The tomographic projections from dogs 3, 4 and 6 were captured with the Hamamatsu Flat Panel Detector, and therefore had a lower dose delivered due to the shorter scan time. All of the six dogs received less than the two Gy maximum surface dose allowance, and were successfully recovered from anesthesia, and are currently healthy and free of acute radiation syndrome symptoms. Unfortunately, none of the reconstructions from any of the views collected from the live dogs show the *in situ* prostate. Figure 5.14 shows an example reconstruction from dog 5. The reconstruction has no soft tissue contrast, while bone is slightly more apparent. All the reconstructions from all six live dogs are comparable to Figure 5.14, and show less detail than the cadaver dog's reconstructions.

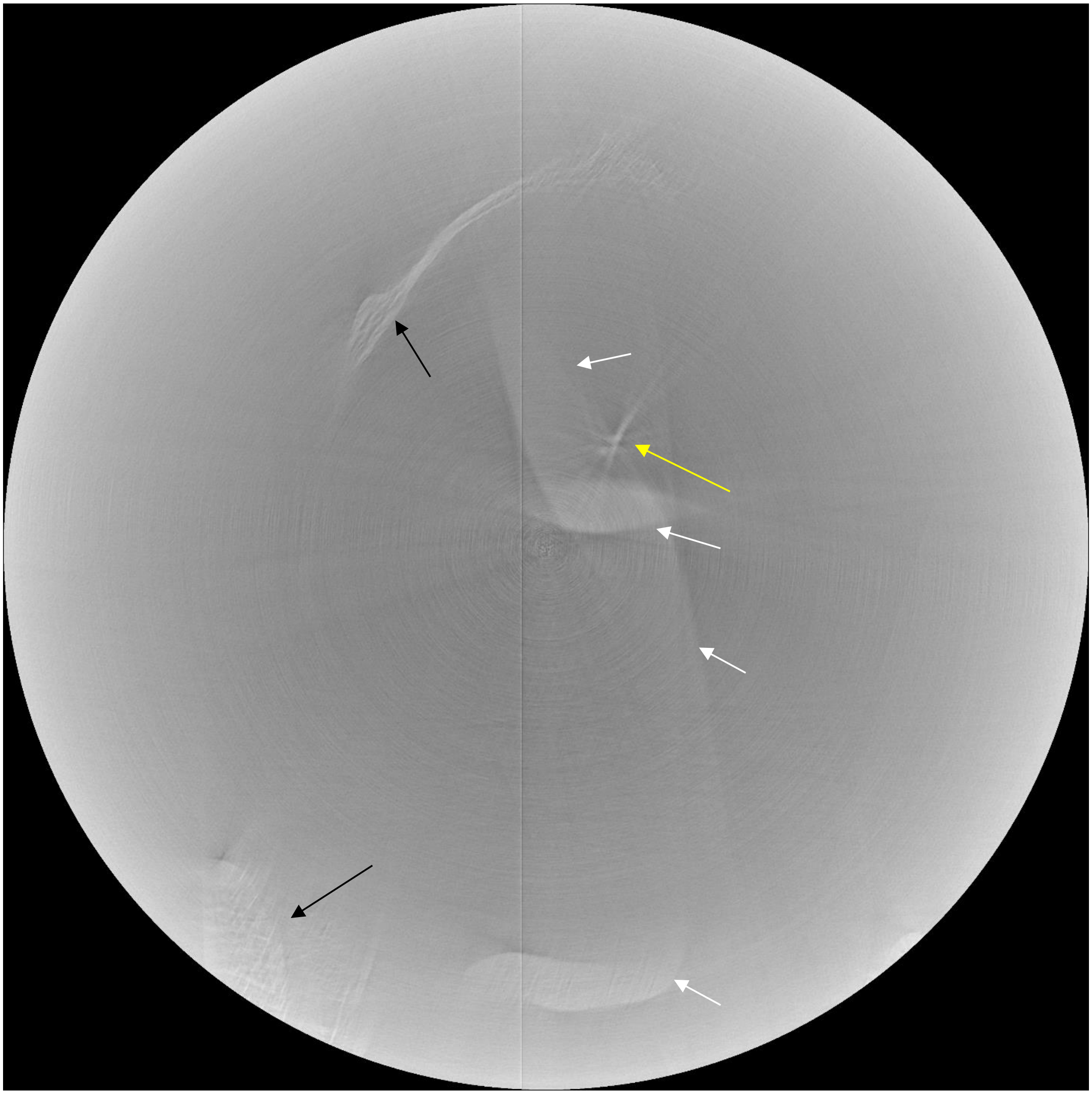

Figure 5.14: A reconstructed slice from dog 5. There is a large amount of motion blur and streaking artifacts (indicated with white arrows), and a no visible prostate area. Bone is observable in the bottom left of the image and near the center of the upper left quadrant, indicated with black arrows. The urethral catheter is indicated with a yellow arrow.

There are several proposed reasons why the reconstruction quality from the live dog imaging was poor, including: the general motion artifact issue, unconscious motion (i.e. cardiopulmonary (CP) and gastrointestinal (GI) motion), and low signal transmission. Both motion artifact and low signal transmission contribute greatly to poor reconstruction quality, while unconscious motion has a lesser effect. The motion issue has previously been discussed in section 5.2, and was known to be an issue before the live dogs were imaged. Breathing, heartbeats, and smooth muscle contraction of the GI tract during scanning could result in motion artifact formation in the reconstructions. Some of this unconscious motion can be overcome with CP gaiting, a type of monitoring that synchronizes the image capture time with a specific phase of the CP cycle. In this way the tomographic projections can be captured when the dog is in the same breathing position, thereby minimizing the CP motion effect seen in the tomographs and reconstructions (112). Cardiac and respiratory gating would greatly increase scan time, as each tomographic projection needs to be captured at the same position of the heart and breathing cycle. This was not attempted in this study. There is no effective way to control GI motion, though a rectal balloon has been proposed as a potential device. The balloon would be inserted into the rectum of the dog and inflated, potentially reducing any motion of the prostate caused by motion of the rectum. These rectal balloon have been employed in humans undergoing radiotherapy for the treatment of rectal and prostate cancer (113), but no previous research was found describing their use with dogs. Low signal transmission is the final proposed issue of live dog imaging. Recall from section 3.1.1 that the X-ray transmission through a sample is equal to:

$$\frac{I}{I_0} = e^{-\mu x} \qquad [3.1]$$

The thickness (*x*) is an important factor for live dog imaging, and is one of the reason for the poor signal transmission. The transmission of X-rays through the live dogs is shown in Table 5.5. These transmission values were calculated using the mass attenuation coefficient of soft tissue at 90 keV, and the diameter of the dog in the pelvic region. Notice that the transmission values are all less than the 10% minimum transmission required for high quality CT reconstructions (98). For simplicity sakes the dog is assumed to be a cylinder of uniform mass attenuation coefficient. Although the assumption that each dog is a perfect cylinder of homogenous mass attenuation coefficient is clearly inaccurate, it does provide an over-estimation of the amount of X-ray transmission through the dog.

Dog	Diameter (cm)	Transmission (I/I_0)
1	18.6	3.13
2	21.83	1.71
3	20.83	2.31
4	18.60	3.13
5	17.78	3.63
6	15.36	5.71

Table 5.5: The transmission (I/I_0) of each of the live dogs imaged on BMIT. For simplicity sake the dog is assumed to be a cylinder of uniform diameter as indicated.

From Table 5.5, it is apparent that the thickness of the dog is too large for sufficient signal transmittance (above 10%). This is called the transmission issue. In clinical CT the transmission issue can be overcome by increasing the current of the X-ray tube, thereby increasing the flux generated, and the amount of photons hitting the detector (114). Unfortunately, the synchrotron storage ring current cannot be modulated to increase the flux generated. There is currently no way to increase the flux during PC-CT in real time like in clinical CT. The transmission issue is also more complicated due to the non-homogenous nature of the mass attenuation coefficient within the dog. While the dog is being imaged there is potential for areas to have less attenuation or less thickness than other areas within the beam, leading to certain regions of very high transmission. There may also be areas of greater thickness or increased mass attenuation coefficients, giving rise to regions of very low transmission. These high and low transmission areas can occur in the same tomographic projection. This complicates the transmission issue because certain areas of the detector may get over-exposed to X-rays, while in the same projection there can be areas of under-exposure. As the dog is rotating through the scan, the detector can repeatedly be over-exposed and under-exposed to X-rays, reducing the quality of the captured tomographic projections and therefore, the quality of the reconstructions as well. Solutions for the transmission and slumping issues have not been found to date resulting in poor reconstruction quality in the images achieved in cadavers and live dogs.

Chapter 6: Conclusion

6.1 *Overview*

In the past twenty years, synchrotron X-ray imaging has emerged as a novel way for high resolution imaging of biological tissues and samples. The specific objective of this thesis was to design, develop, and implement a canine positioning system for the Biomedical Imaging and Therapy – Insertion Device beamline, capable of imaging *in situ* dog prostates in both cadaver and live dogs. Chapter one introduced the idea of using PC-CT to image *in situ* canine prostates as a way to determine cellular morphologies, with the hope of eventually using PC-CT as a diagnostic tool for human PCa. Chapter two examined the current understanding of human and canine prostate anatomy and pathology, as well provided justification for the use of dogs as a model for human PCa. In chapter three, the general information of radiology and synchrotron imaging was discussed, and background was provided on the use of PC-CT for *in situ* imaging.

Chapter four presented the design process for the canine positioning device, along with the background information of the detectors used for PC-CT. The canine positioning device was successfully designed and manufactured, and meet the specifications required of the design. In chapter five the implementation of the device was discussed, including cadaver and live dog imaging. The device failed to properly immobilize the dogs during imaging, resulting in severe motion of the dog. The motion artifact issue, along with the transmission issue, generated CT reconstructions of poor quality, and prevented the *in situ* prostate from being visualized at this time.

6.2 *Future Directions*

The motion and transmission issue must be addressed before any future research can be conducted with the canine positioning device. The modified seat will be revamped and improved to better immobilize the dog within the device. Once the motion artifact issue is addressed, work can be done to correct the transmission issue. It is anticipated that ultimately this device will also be able to be used to image areas of the dog other than the prostate.

The canine positioning device can be used to compare *in situ* canine prostates PC-CT to clinical diagnostic tools, such as magnetic resonance imaging, CT, ultrasound, and positron emission tomography-CT. Studies can be conducted on experimental induction of BPH and PCa in dogs, with the device used to collected PC-CT reconstructions of control and treatment groups. Accomplishing *in situ* imaging of canine prostates is the first step towards *in situ* imaging of human prostates.

6.3 *Conclusion*

This thesis has laid the ground work for canine imaging on the Biomedical Imaging and Therapy – Insertion Device beamline at the Canadian Light Source. The design and implementation of the device are described, along with the issues discovered and addressed. Unfortunately, no *in situ* canine prostates were seen post-imaging in reconstructions. This is a significant setback in the potential use of PC-CT as a diagnostic tool for human PCa, but is nonetheless an important step forwards in both prostate cancer and medical imaging research.

Works Cited

1. *Beamlines of the Biomedical Imaging and Therapy Facility at the Canadian Light Source-Part 1.* Wysokinski, T., Chapman, D., Adams, G., Renier, M., Suortti, P., Thomlinson, W. 1, Saskatoon : Nuclear Instrumentation and Methods in Physics Research A, 2015, Vol. 582. doi:10.1016/j.nima.2007.08.087.

2. Jensen, T.H. *PhD thesis, refraction and scattering based x-ray imaging.* Copenhagen : University of Copenhagen, 2010.

3. Canadian Cancer Society's Advisory Committee on Cancer Statistics. *Candian Cancer Statistics 2015.* Toronto : Canadian Cancer Society, 2015. Available from http://www.cancer.ca/~/media/cancer.ca/CW/cancer%20information/cancer%20101/Canadian%20cancer%20statistics/Canadian-Cancer-Statistics-2015-EN.pdf?la=en . Accessed Januray 29 2017.

4. *How reliable is 12-core prostate biopsy procedure in the detection of prostate cancer?* Akincioglu, E., Altinova, S., Asil, E., Balbay, M.D., Serefoglu, E.C., Ugras, N.S. 5-6, s.l. : Canadian Urological Association Journal, 2013, Vol. 7. doi: 10.5489/cuaj.11224.

5. *Serial biopsy reults in prostate cancer sreening study.* Roehl, K.A., Anternor, J.V., Catalona, W.J. St. Louis : The Journal of Urology, 2002, Vol. 167, pp. 2435-2439. 0022-5347/02/1676-2435/0.

6. *Saturation Techinque Does Not Decrease cancer Detection During Followup After Initial Prostate Biopsy.* Lane, B.R., Zippe, C.D., Aboiassal, R., Schoenfield, L., Magi-Galluzzi, C., Jones, J.S. Clevland : The Journal of Urology, 2008, Vol. 179, pp. 1746-1750. DOI:10.1016/j.juro.2008.01.049.

7. *Prospective Study of Diagnostic Accuracy Compaing Prostate Cancer Detection by Transrectal Ultrasound-Guided Biopsy Versus Magnetic Resonance (MR) Imaging with Subsequent MR-guided Biopsy in Men Without Previous Prostate Biopsies.* Barentsz, J.O., Duncan, E.,Parkinson, R., Pokorny, M.R., Rooij, M.D., Schroder, F.H., Thompson, L.C. 1, s.l. : European Urology, 2014, Vol. 66.

8. Institute, National Cancer. *Understanding prostate changes – A health guide for men.* Bethesda : National Cancer Institute, 2015. Available from https://www.cancer.gov/types/prostate/understanding-prostate-changes/prostate-booklet.pdf .Accessed January 29 2017.

9. *Toward Clinical X-ray phase-contrast CT: demonstration of enhanced soft-tissue contrast in human specimen.* Bunk, O., David, C., Donath, T., Grunzweig, C., Hempel, E., Pfeiffer, F., Popescu, S., Vock, P. 7, s.l. : Investigations In Radiology, 2012, Vol. 45. doi: 10.1097/RLI.0b013e3181e21866.

10. *Curret studies and duture perspectives of sycnhrtron radiation imaging trial in human patients.* Longo, R. s.l. : Nuclear Instruments and Methods in Physics Research Section A: Accelerators, Spectrometers, Dectectors and Associated Equipment, 2016, Vol. 809, pp. 13-22. doi:10.1016/j.nima.2015.10.110.

11. *Diffraction enhanced x-ray imaging.* Chapman, D., Thomlinson, W., Johnston, R.E., Washburn, D., Pisano, E., Gmur, N., Zhong, Z., Menk, R., Arfelli, F., Sayers, D. 11, Chicago : Phys Med Biol, 1997, Vol. 42. PMID: 9394394.
12. *Developments in The Theory of Synchrotron Radiation and Its Reabsorption.* Ginzburg, V.L., Syrovatskii, S.I. Moscow : Annual Review of Astronomy and Astrophysics, 1969, Vol. 7. DOI: 10.1146/annurev.aa.07.090169.002111.
13. *X-ray Phase contrast tomography with a bending magnet source.* Carlo, F.D., Dhal, B.B., McMahon, P.J., Nugent, K.A., Peele, A.G. 8, s.l. : Review of Scientific Instruments, 2005, Vol. 76. doi: http://dx.doi.org/10.1063/1.2005447.
14. *A compressed sensing based reconstruction algorithm for synchrotron source propagation-based X-ray phase contrast computed tomography.* Ali Melli, S., Babyn, P., El-Gayed, A., Montgomery, J., Pettitt, M., Snead, E., Wahid, K.A., Wesolowski, M., Wolkowski, B. Saskatoon : Nuclear Instruments and Methods in Physics Research Section A: Accelerators, Spectrometers, Detectors and Associated Equipment, 2016, Vol. 806. doi:10.1016/j.nima.2015.10.013.
15. *Spontaneously occurring tumors of companion animals as models for human cancer.* MacEwen, E.G., Vail, D.M. 8, s.l. : Cancer Investigations, 2000, Vol. 18. PMID: 11107448.
16. Oh, W.K., Hurwitz, M., D'amico, A.V., Richie, J.P., Kantoff, P.W. *Holland-Frei Cancer Medicine. 6th edition.* Hamilton : BC Decker, 2003. ISBN-10: 1-55009-213-8.
17. *Normal histology of the prostate.* Mcneal, J.E. 8, s.l. : American Journal of Surgical Pathology, 1988, Vol. 12. PMID: 2456702.
18. *Inflammation in prostate carcinogenesis.* De Marzo, A.M., Drake, C.G., Gronberg, H., Isaacs, W.B., Nakai, Y., Nelson, W.G., Platz, E.A., Sutcliffe, S., Xu, J. 4, s.l. : Nature Review of Cancer, 2007, Vol. 7. doi:10.1038/nrc2090.
19. Berman, D.M., Veltri, R.W. Development, molecular biology, and physiology of the prostate. [book auth.] A.J., Kavoussi, L.R., Partin, A.W., Peters, C.A. Wein. Philidelphia : W.B Saunders, 2011.
20. *Benign Prostatic Hyperplasia.* Paolone, D.R. 2, s.l. : Clinics in Geriatric Medicine, 2010, Vol. 26. DOI: http://dx.doi.org/10.1016/j.cger.2010.02.010.
21. *Benign mimickers and potential precursors of prostatic adenocarcinoma.* Srigley, J.R., Zhou, M. 19, s.l. : Dignostic Histopathology, 2011, Vol. 17. DOI: http://dx.doi.org/10.1016/j.mpdhp.2011.06.011.
22. *[Prostatic Stromal Tumors of Uncertain Malignant Potential (STUMP): definition, pathology, prognosis and management]*. Bouchot, O.,Branchereau, J., Braud, G., Moreau, A., Michaud, S., Renaudin, K., Rigaud, J. 12, s.l. : Progres en Urologie, 2012, Vol. 22. doi: 10.1016/j.purol.2012.06.004.
23. Simon, H., Zieve, D. *Benign Prostatic Hyperplasia.* Maryland : University of Maryland Medical Center, 2012.
24. *Benign prostatic hyperplasia in primary care: what you need to know.* Burnett, A.L., Wein, A.J. 175, s.l. : The Journal of Urology, 2006, pp. S19-24.

25. *Prostatic Intraepithelial Neoplasia: An Overview.* Brawer, M. Suppl 3, s.l. : Reviews In Urology, 2005, Vol. 7. PMC1477603.
26. *Preneoplasia in the prostate gland with emphasis on high grade prostatic intraepithelial neoplasia.* Merrimen, J.L.O., Evans, A,J., Srigley, J.R. 3, s.l. : American Journal of Pathology, 2013, Vol. 45. DOI: 10.1097/PAT.0b013e32835f6134.
27. *Clinical Significance of Proliferative Inflammatory Atrophy in Prostate Biopsy.* Arbos, M.A., Celma, A., de Torres, I., Morote, J., Placer, J., Planas, J., Quilex, M.T., Servian, P. 2, s.l. : Actas Urologicas Espanolas, 2013, Vol. 38.
28. *Interobserver Reproducibility in the Diagnosis of Prostatic Intraepithelial Neoplasia.* Epstein, J.I., Grignon, D.J., Humphery, P.A., McNeal, J.E., Sesterhenn, I.A., Troncoso, P. 8, Baltimore : American Journal of Surgical Pathology, 1995, Vol. 19. DOI: 10.1097/00000478-199508000-00002.
29. *Clinical significance of proliferative inflammatory atrophy in prostate biopsy.* Celma, A., Servain, P., Planas, J., Placer, J., Quilex, M.T., Arbos, M.A., Torres, I.D., Morote, J. 2, s.l. : Actas Urologicas Espanolas (English Edition), 2014, Vol. 38, pp. 122-126. doi:10.1016/j.acuroe.2013.10.011.
30. *Morphological transition of proliferative inflammatory atrophy to high-grade intraepithelial neoplasia and cancer in human prostate.* Bergh, A., Damber, J.E., Wang, W. 13, s.l. : The Prostate, 2009, Vol. 69. DOI: 10.1002/pros.20992.
31. *Defining the ideal cutpoint for determining PSA recurrence after radical prostatectomy.* Freedland, S., Sutter, M.E., Dorey, F., Aronson, W.J. 2, s.l. : Urology, 2003, Vol. 61, pp. 365-369.
32. *Screening for prostate cancer, Controversy? What controversy?* Albin, R.J., Haythorn, M.R. 3, s.l. : Current in Oncology, 2009, Vol. 16, pp. 1-2.
33. *Recommendations on screeing for prostate cancer with the prostate-specific antigen test.* Bell, N., Dickinson, J., Dunfield, L., Gorber, S.C., Joffres, M., Shane, A., Shaw, E., Singh, H., Tonelli, M. 16, s.l. : CMAJ, 2014, Vol. 186. doi: 10.1503/cmaj.140703.
34. *Lifetime and recent prostate specific antigen (PSA) screeening of men for prostate cancer in Canada.* Beaulac, J.A., Fry, R.N., Onysko, J. 3, s.l. : Canadian Journal of Public Health, 2006, Vol. 97, pp. 171-176.
35. *Correlation between prostate size estimated by digital rectal examination and measured by transrectal ultrasound.* Roehrborn, C.G., Girman, C.J., Rhodes, T., Hanson, K.A., Collins, G.N., Sech, S.M., Jacobsen, S.J., Garraway, W.M., Bieber, M.M. 4, s.l. : American Journal of Urology, 1997, Vol. 49, pp. 548-557. http://www.ncbi.nlm.nih.gov/pubmed/9111624.
36. Shevchuk, M.M., Robinson, B.D. the Pathology of Prostatic Carcinoma. [book auth.] A., Costello, A.J., Mahesh, D., Eastham, J.A., Fitzpatrick, J.M., Gleave, M., Neal, D., Sampaio, F.J.B., Sooriakumaran, P., Vaughan, E.V. Tewari. *Prostate Cancer: A Comprehensive Perspective.* London : Springer-Verlag, 2013.
37. *The 2014 International Society of Urological Pathology (ISUP) Consensus Conference on Gleason Grading of Prostatic Carcinoma: Definition of Grading Patterns and Proposal for a*

New Grading System. Epstein, J., Egevad, L., Amin, M.B., Delahunt, B., Srigley, J.R., Humphrey, P.A., Grading Committee. 2, s.l. : American Journal of Surgical pathology, 2016, Vol. 40. PMID: 26492179.
38. *A Contemporary Prostate Cancer Grading System: A Validated Alternative to the Gleason Score.* Epstein, J.I., Zelefsky, M.J., Sjoberg, D.D., Nelson, J.B., Egevad, L., Magi-Galluzzi, C., Vivkers, A.J., Parwani, A.V., Reuter, V.E., Fine, S.W., Eastharn, J.A., Wiklund, P., Han, M., Reddy, C.A., Ciezki, J.P., Nyberg, T., Klein, E.A. 3, s.l. : European Urology, 2016, Vol. 69, pp. 428-435.
39. *Canine Prostatic Disease.* Barsanti, J.A., Finco, D.R. 3, s.l. : Vet Clin North Am Small Anim Pract, 1986, Vol. 16. PMID: 3487161.
40. Urogenital System of the Dog. *Healthy Animals, Healthy People, Healthy Planet.* [Online] Washington State University College of Veterinary Medicine. [Cited: May 22, 2016.] https://www.vetmed.wsu.edu/outreach/Pet-Health-Topics/categories/cat-and-dog-anatomy/urogenital-system-of-the-dog.
41. Evans, H.E, Christensen, G.C. The urogential system. *Miller's anatomy of the dog.* s.l. : WB Saunders, 1993.
42. *Canine Prostatic disease: A review of anatomy, pathology, diagnosis, and treatment.* Smith, J. 3, s.l. : Theriogenology, 2008, Vol. 70. PMID: 18514299.
43. *Noninfectious prostatic diseases in dogs.* Gobello, C., Corranda, Y. s.l. : Compendium of Continuing Education Vet, 2002, Vol. 24, pp. 99-107.
44. *"The creeping tumor" An unusual presentation of upper urinary tract malignancy.* Selvaraj, V., Govindarajan, P., Deepak, M., Sivaraj, M. 1, s.l. : Indian Journal of Urology, 2014, Vol. 30, pp. 454-455.
45. *Immunohistochemical differentiation of high-grade prostate carcinoma from urothelial carcinoma.* Chuang, A.Y., DeMarzo, A.M., Veltri, R.W., Sharma, R.B., Bieberich, C.J., Epstein, J.I. 8, s.l. : American Journal of Surgical Pathology, 2007, Vol. 31, pp. 1246-1255.
46. *A population study of neutering status as a risk factor for canine prostate cancer.* Bryan, J.N., Keeler, M.R., Henry, C.J., Bryan, M.E., Hahn, A.W., Caldwell, C.W. 1, s.l. : Prostate, 2007, Vol. 67. PMID: 17516571.
47. *Noninfectious prostatic diseases in dogs.* Gobello, C., Corrada, Y. 1, s.l. : Compend contin Educ Vet, 2002, Vol. 24.
48. *Prostatic intraepithelial neoplasia in dogs with spontaneous prostate cancer.* Waters, D.J., Hayden, D.W., Bell, F.W., Klausner, J.S., Wian, J., Bostwick, D.G. 1, s.l. : Prostate, 1997, Vol. 30, pp. 92-97.
49. *Comparing the age a prostate cancer diagnosis in humans and dogs.* Waters, D.J., Patronek, G.J., Bostwick, D.G., Glickman, L.T. 1, s.l. : Journal of National Cancer Institutue, 1996, Vol. 88, pp. 1686-1687.
50. *Prostatic intraepithelial neoplasia: Animal models.* Bostwick, D.G., Ramnani, D., Qian, J. s.l. : Prostate, 2000, Vol. 43, pp. 286-294.

51. *Workgroup 4: spontaneous prostate carcinoma in dogs and nonhuman primates.* Waters, D.J., Sakr, W.A., Hayden, D.W., Lang, C.M., McKinney, L.,Murphy, G.P., Radinsky, R., Ramoner, R., Richardson, R.C., Tindall, D.J. 1, s.l. : Prostate, 1998, Vol. 36, pp. 64-67.
52. *High grade prostatic intraepithelial neoplasia in military working dogs with and without prostate cancer.* Aquilina, J.W., McKinney, L., Pacelli, A. Richman, L.K., Waters, D.J., Thompson, I., Burghardt, W.F.Jr., Bostwick, D.G. 36, s.l. : Prostate, 1998, Vol. 3, pp. 189-193.
53. *Effects of aging on prostate growth in beagles.* Berry, S.J., Coffey, D.S., Ewing, L.L. 250, s.l. : American Journal of Physiology, 1986, pp. R1039-1046.
54. *Binign prostate hyperplasia: Evaluation of treatment respone with DCE MRI.* Hevergagen, J.T., Tengg-Bobligk, H. von., Baudendistel, K.T., Jia, G., Polzer, H., Henry, H., Levine, A.L., Rosol, T.J., Knopp, M.V. 17, Columbus : MAGMA, 2004, pp. 5-11. DOI 10.1007/s10334-004-0040-1.
55. *The requirement of the testis in establishing the sensitivity of the canine prostate to develop benign prostatic hyperplasia.* Juniewicz, P.E., Berry, S.J., Coffey, D.S., Strandberg, J.D., Ewing, L.L. 152, 1994 : Journal of Urology, pp. 996-1001.
56. *Sevelopment of canine benign prostatic hyperplasia with age.* Berry, S.J., Strandberg, J.D., Saunders, W.J., Coffey, D.S. 9, s.l. : Prostate, 1986, pp. 363-373.
57. *Prostatic intraepithelial neoplasia occurs spontaneously in the canine prostate.* Waters, D.J., Bostwick, D.G. 2, Rochester : The Journal of Urology, 1996, Vol. 157. http://dx.doi.org/10.1016/S0022-5347(01)65256-X.
58. *prostatic intraepithelial neoplasia in dogs with spontaneous prostate cancer.* Waters, D.J., Hayden, D.W., Bell, F.W., Klausner, J.S., Qian, J., Bostwick, D.G. 2, s.l. : Prostate, 1996, Vol. 30.
59. *Canine Prostatic Intraepithelial Neoplasia: is the comparative model relevant?* Madewell, B.R., Gandour-Edwards, R., DeVere White, R.W. s.l. : The Prostate, Vol. 58, pp. 314-317.
60. *Immunohistochemical characterization of canine prostatic intraepithelial neoplasia.* Matsuzaki, P., Cogliati, B., Sanches, D.S., Chabible, L.M., Kimura, K.C., Silva, T.C., Real-Lima, M.A., Hernandez-Blazquez, F.J., Laufer-Amorim, R., Dagli, M.L.Z. 1, s.l. : Journal of Camparative Pathology, 2010, Vol. 142, pp. 84-88. http://dx.doi.org/10.1016/j.jcpa.2009.06.005.
61. *A restrospective analysis of 111 canine prostatic samples: Histopathological findings and classification.* Palmieri, C., Lean, F.Z., Akter, S.H., Romussi, S., Grieco, V. 97, s.l. : Research in Veterinary Science, 2014, Vol. 3, pp. 568-573. doi:10.1016/j.rvsc.2014.11.006.
62. *Evaluation of serum and seminal plasma markers in the diagnosis of canine prostatic disorders.* Bell, F.W., Klausner, J.S., Hayden, D.W., Lund, E.M., Liebenstein, B.B., Feeney, D.A., Johnston, S.D., Shivers, J.L., Ewing, C.E., Isaacs, W.B. 3, s.l. : Journal of Veterinary Internal Medicine, 1995, Vol. 9, pp. 149-153. 0891 -6640/95/0903-0004$3.00/0.
63. *Diagnostic possibilities in the management of canine prostatic disorders.* Paclikova, K., Kohout, P., Vlasin, M. 1, s.l. : Veterinarni Medicina, 2006, Vol. 51, pp. 1-13.

64. Dorfman, M., Barsanti, J.A. CVT Update: Treatment of canine bacterial prostatitis. [book auth.] J.D. Bonagura. *Kirk's Current Veterinary Therapy XII: Small Animal Practice.* s.l. : Current Veterinary Therapy XII, 1995.
65. *Determination of canine prostatic volume using trans-abdominal ultrasonography.* Kamoplatana, K., Johnston, G.R., Johnston, S.D. s.l. : Veterinary radiology and ultrasound, 1999, Vol. 36, pp. 226-230.
66. *Diagnostic imaging of the male canine reproductive organs. Methods and limitations.* Johnston, G.R., Feeney, D.A., Rivers, B., Walter, P.A. s.l. : Veterinary Clinics of North America Small Animal Practice, 1991, Vol. 21, pp. 553-589.
67. *Ultrasound guided biopsy.* Smith, S. 1, s.l. : Veterinary Clinics of North America, 1985, Vol. 15, pp. 1249-1262.
68. Zinkl, J. Cytology of the male reproductive tract. [book auth.] R.I., Tyler, R.D., Meinkoth, J.M Cowell. *Diagnostic cytology and hematology of the dog and cat.* St. Louis : CV Mosby, 1999.
69. *Diagnosis of canine prostatic carcinoma.* Nickel, R.F., Teske, E. s.l. : Tijdschrift voor Diergeneeskunde, 1992, Vol. 117, pp. 32-36.
70. Leav, I., Schelling, S.H., Merk, F.B. Age-related and sex hormone-induced changes in the canine prostate. [book auth.] U, Carlton, W.W., Dungworth, D.L., Benjamin, S.A., Capen, C.C., Han, F.F. Mohr. *Pathobiology of the aging dog.* Ames : Iowa State University Press, 2001.
71. *Role of canine basal cells in postnatal prostatic development, induction of hyperplasia, and sex hormone-stimulated growth; and the ductal origin of carcinoma.* Leave, I., Schelling, K.H., Adams, J.Y., Merk, F.B., Alroy, J. s.l. : The Prostate, 2001, Vol. 48, pp. 210-224.
72. *Prostate cancer in dogs: Comparative and clinical aspects.* LeRoy, B.E., Northrup, N. 2, s.l. : The Veterinary Journal, 2009, Vol. 180, pp. 149-162.
73. *Polysomy 13 in a canine prostate carcinoma underlining its significance in the development of prostate cancer.* Winkler, S., Reimann-Berg, N., Murua, E.H., Loeschke, S., Eberle, N., Hoinhaus, R., Notle, I., Bullerdiek, J. s.l. : Cancer genetics and cytogenetics, 2006, Vol. 169, pp. 154-158.
74. *Refining the orthotopic dog prostate cancer (DPC)-1 model to better bridge the gap between rodents and men.* Anidjar, M., Chevalier, S., Cury, F.L., Hamel, L., Luz, M., Rocha, J., Scarlata, E. 7, s.l. : Prostate, 2012, Vol. 72. doi: 10.1002/pros.21479.
75. *Proposal of Gleason-like grading system of canine prostate carcinoma in veterinary pathology practice.* Grieco, V., Palmieri, C. s.l. : Research in Vertrinary science, 2015, Vol. 103. doi:10.1016/j.rvsc.2015.09.004.
76. *A retrospective analysis of 111 canine prostatic samples:.* Akter, S.H., Grieco, V., Lean, F.Z., Plamieri, C., Romussi, S. Gatton : Research in Veterinart Science, 2014, Vol. 97. http://dx.doi.org/10.1016/j.rvsc.2014.11.006.
77. Neutze, J.A., Singh, H. *Radiology Fundamentals: Introduction to Imaging & Technology.* New York : Springer Science+Business Media, 2012. DOI 10.1007/978-1-4614-0944-1_3.
78. *Tables of X-Ray Mass Attenuation Coefficients.* Hubbell, J.H., Seltzer, S.M. s.l. : NIST, 1996.

79. Dance, D.R., Christofides, S., Maidment, A.D.A., McLean, I.D., Ng, K.H. *Diagnostic Radiology Physics: A Handbook For Teachers And Students.* Vienna : International Atomic Energy Agency, 2014. ISBN 978–92–131010–1.
80. Hounsfield, G.N. *Computed Medical Imaging.* London : The Medical Systems Department of Central Research Laboratories EMI, 1979. http://www.nobelprize.org/nobel_prizes/medicine/laureates/1979/hounsfield-lecture.pdf.
81. ChumpusRex. Ct-internals.jpg. 2007. https://commons.wikimedia.org/wiki/File:Ct-internals.jpg.
82. Abbot, A.L., Kriz, R.D., Rao, R., Ribbens, C.J. *Parallel Implementation of the Filtered Back Projection Algorithm for Tomographic Imaging.* [Web] Virginia : Virgina Tech, Virginia Tech College of Engineering, 1995. http://www.sv.vt.edu/xray_ct/parallel/Parallel_CT.html.
83. Smith, S.W. *The Scientist and Engineer's Guide to Digital Signal Processing.* San Diego : California Techical Publishing, 1997. ISBN-10: 0966017633.
84. *Radiation from Electrons in a Synchrotron.* Elder, F.R., Gurewitsch, M., Langmuir, V., Pollock, H.C. New York : Phys Rev, 1947, Vol. 71. DOI:http://dx.doi.org/10.1103/PhysRev.71.829.5.
85. Machine Design. *Light Source.* [Online] Canadian Light Source. [Cited: February 4, 2016.] http://www.lightsource.ca/operations/machinedesign.php.
86. *Beamlines of the biomedical imaging and therapy facility at the Canadian light source – part 3.* Wysokinski, T., Chapman, D., Adams, G., Renier, M., Suortti, P., Thomlinson, W. 1, Saskatoon : Nuclear Instruments and Methods in Physics Research Section A: Accelerators, Spectrometers, Detectors and Associated Equipment, 2015, Vol. 775. doi:10.1016/j.nima.2014.11.088.
87. *The Relfection of X-rays by Crystals.* Bragg, W.H., Bragg, W.L. 605, s.l. : Proceedings of the Royal Society A, 1913, Vol. 88. DOI: 10.1098/rspa.1913.0040.
88. *Holotomography: quantitative phase tomography with micrometer resolution using hard synchrotron radiation x rays.* Cloetens, P., Ludwig, W., Baruchel, J., Van Dyke, D., Van Landuyt, J., Guigay, J.P., Schlenker, M. Arnhem : Appl Phys Lett, 1999, Vol. 75. DOI:http://dx.doi.org/10.1063/1.125225.
89. *Introduction to Experimental Partice Physics.* Cambridge : Cambride University Press, 1986. ISBN 0 521 37940.
90. Jian, Fu. Phase Contrast Computed Tomography. [book auth.] Luca Saba. *Computed Tomography - Clinical Applications.* Shanghai : InTech China, 2012.
91. *Low-dose phase contrast x-ray medical imaging.* Arfelli, F., Assante, M., Bonvicini, V., Bravin, A., Cantatore, G., Castelli, E., Dalla Palma, L., Di Michiel, M., Longon, R., Olivio, A., Pani, S., Pontoni, D., Poropat, P., Prest, M., Rashevsky, A., Tromba, G., Vacchi, A., Vallazza, E., Zanconati, F. 10, s.l. : Phys Med Biol, 1998, Vol. 43. PMID: 9814522.
92. Mcm222. File: Propagation-based imaging.PNG. [Online] May 7, 2012. [Cited: April 25, 2017.] https://commons.wikimedia.org/wiki/File:Propagation-based_imaging.PNG.

93. *Theory of quantitative phase-contrast computed tomography.* Bronnikov, A.V. 3, s.l. : Journal of the Potical Society of America A, 2002, Vol. 19. ISSN 1084-7529.
94. Dyce, K.M., Sack, W.O., We sing, C.J.G. *Textbook of Veterinary Anatomy, 4th Edition.* s.l. : Saunders, 2010.
95. Avail Concepts, LLC. Pawsitioner. *Pawsitioner.* [Online] Avail Concepts, LLC, 2014. [Cited: 2 4, 2016.] http://www.pawsitioner.com/.
96. Bruker MicroCT. NRecon. Kontich, Belgum : s.n.
97. Fressler, J. *Mass Attenuation Coefficient Lexan (Polycarbonate: C16H14O3).* Ann Arbor : University of Michigan.
98. *CT artifacts: Causes and reduction techniques.* Boas, F.E., Fleischmann, D. 2, Stanford : Imaging Med, 2012, Vol. 4. http://www.edboas.com/science/CT/0012.pdf.
99. Zhu, N. Detector Specifications: XHI-VHR 90. *Canadian Light Source.* [Online] Biomedical Imaging and Therapy, September 15, 2014. [Cited: June 16, 2016.] http://exshare.lightsource.ca/bmit/Lists/Spec2/DispForm.aspx?ID=21.
100. Zhu, N., Webb, A. Detectors. *BioMedical Imagina and Therapy Facility.* [Online] [Cited: June 16, 2016.] http://bmit.lightsource.ca/tech-info/detectors/.
101. *Identification of a unique cause of ring artifact seen in computed tomography trans-axial images.* Agrawal, A., Jha, A.K., Purandare, N.C., Puranik, A.D., Rangarajan, V., Shan, S. 4, Maharashtra : Indian Journal of Nuclear Medicine, 2013, Vol. 28, pp. 232-233.
102. *High-Resolution CT of the Lungs.* Kazerooni, E.A. 3, Michigan : American Journal of Roentgenology, 2001, Vol. 177.
103. Runge, V.M. Image Resolution: Pixel and Voxel Size. *Clinical MRI.* Temple : W.B Saunders Company.
104. Load Up (tm) Harness. *vehicle restraint harness.* Bend : Ruffwear, 2016.
105. Walkabout Front Harness. *Dogs in Motion Canine Rehabilitation.* 2016.
106. AK Scientific, Inc. *Diatrizoic acid.* California : Online, 2014. http://aksci.com/sds/H919_SDS.pdf.
107. *Acute radiation enteritis caused by dose-dependent radiation exsposure in dogs: Experimental research.* Xu, W., Chen, J., Xu, L., Li, H., Guo, X. Shenyang : Experimental Biology and Medicine, 2014, Vol. 239, pp. 1543-1556.
108. *Systemic mechanisms and the effects of ionizing radiation: A new "old" paradigm of how the bystanders and distant can become the players.* Nitkitaki, Z., Mavragani, I.V., Laskaratou, D.A., Gika, V., Moskvin, V.P., Theofilatos, K., Vougas, K., Stewart, R.D., Georgakilas, A.G. s.l. : Seminars in Cancer Biology, 2016, Vols. 37-38, pp. 77-95.
109. *Autologous bone marrow stromal cell transplantation as a treatment for acute radiation enteritis induced by a moderate dose of radiation in dogs.* Xu, W., Chen, J., Liu, X., Li, H., Qi, X., Guo, X. Shenyang : The journal of Laboratory and Clinical Medicine, 2016, Vol. 171, pp. 38-51.
110. *Estimation of contrast of refraction contrast imaging compared with absorption imaging-basic approach.* Hirano, M., Yamasaki, K. 1-2, Yagumo : Nuclear Instruments and Methods in

Physic Section A: Accelerators, Spectrometers, Detectors and Associated Equiptment, 2005, Vol. 548. http://dx.doi.org/10.1016/j.nima.2005.03.088.

111. *Dose fractionation in synchrotron radiation x-ray phase micro-tomography.* Frachon, T., Webe, L., Hesse, B., Rit, S., Dong, O., Olivier, C., Peyrin, F., Langer, M. 19, s.l. : Physics in Medicine and Biology, 2015, Vol. 60.

112. *ECG-Gated Cardiac CT.* Desjardins, B., Kazerooni, E.A. 4, s.l. : American Journal of Roentgenology, 2004, Vol. 182, pp. 993-1010.

113. *The use of rectal balloon during the delivery of intensity modulated radiotherapy (IMRT) for prostate cancer: more than just a prostate gland immobilization device?* Teh, B.S., McGary, J.E., Dong, L., Mai, W.Y., Carpenter, L.S., Lu, H.H., Chiu, J.K., Woo, S.Y., Grant, W.H., Butler, E.B. 6, s.l. : Cancer Journal, 2002, Vol. 8, pp. 476-483.

114. *Techniques and applications of automatic tube curent modulation for CT.* Kalra, M.K., Maher, M.M., Toth., T.L., Schmidt, B., Westerman, B.L., Morgan, H.T., Saini, S. s.l. : Radiology, 2004, Vol. 233, pp. 649-657.

115. Urogential System of the Dog. *Healthy Animals, Healthy People, Healthy Planet.* [Online] Washington State University College of Veterinary Medicine. [Cited: May 22, 2016.] https://www.vetmed.wsu.edu/outreach/Pet-Health-Topics/categories/cat-and-dog-anatomy/urogenital-system-of-the-dog.

116. Education, Pet Pig. Further Learning. *Pet Pig Education.* [Online] 2016. [Cited: August 13, 2016.] http://www.petpigeducation.com/further-learning--terminology.html.

117. Pettitt, M. PhD. *Gross Anatomy of the Canine Prostate.* The University of Saskatchewan, Saskatoon : 2017.